Surface Treatment of A Low-cost Beta Titanium Alloy to Combat Wear

University of Birmingham

A thesis submitted for the degree of

Master of Research (MRes)

by

Eleanor Redmore

School of Engineering
Metallurgy and Materials
University of Birmingham

UNIVERSITY OF
BIRMINGHAM

University of Birmingham Research Archive

e-theses repository

This unpublished thesis/dissertation is copyright of the author and/or third parties. The intellectual property rights of the author or third parties in respect of this work are as defined by The Copyright Designs and Patents Act 1988 or as modified by any successor legislation.

Any use made of information contained in this thesis/dissertation must be in accordance with that legislation and must be properly acknowledged. Further distribution or reproduction in any format is prohibited without the permission of the copyright holder.

Surface treatment of a low-cost beta titanium alloy to combat wear

Student: Eleanor Redmore

Supervisors: Professor H Dong and Dr X Li

Abstract

The development of an effective ceramic conversion treatment of TIMETAL LCB (Ti-6.8Mo-4.5Fe-1.5Al) has been investigated. Various characterisation methods were used to analyse samples in order to identify the best process conditions including SEM, EDX, XRD, GDS, micro-indentation and scratch testing. A solution treatment temperature of 850°C was used as this is the appropriate temperature for the mechanism of solution treatment according to the β-transus temperature of this alloy. The results show that a solution treatment of 0.5 hours produces an acceptable thickness of oxygen hardened case, an almost equal hardness to that of a longer treatment and a far better oxide layer, than a longer treatment time did, in terms of adherence to the substrate. An aging temperature of 500°C was found to be the best as a lower temperature than this produced too thin an oxide layer and a higher temperature meant the oxide layer became exceedingly brittle. An aging time of 8 hours was found to be best as this gave good hardness, good performance in both static and dynamic loading and good wear resistance. The wear testing results show that the tribological properties of the TIMETAL LCB alloy have been significantly enhanced by the new ceramic conversion treatment specifically developed for beta alloys. The improved friction and wear properties can be attributed to the low-friction TiO_2 outer oxide surface layer supported by a Ti_3O_5 inner oxide layer and an oxygen diffusion hardened case up to a depth of ~70μm.

ACKNOWLEDGEMENTS

I would like to sincerely thank my supervisors for this Masters research study, Prof. H. Dong and Dr. X. Li, for their invaluable help, guidance and discussions throughout the project.

Thanks are due to all members of the Surface Engineering Group and technical staff from the Department of Metallurgy and Materials who have aided me in my research work and provided helpful discussions.

Thanks are also due to Professor Paul Bowen, Head of the Department of Metallurgy and Materials, for the provision of research facilities.

I greatly thank the Titanium Metals Corporation for the free provision of a TIMETAL LCB sample rod.

I would also like to thank EPSRC, UK for providing an MRes scholarship to enable me to carry out this study in the Department of Metallurgy and Materials at the University of Birmingham.

CONTENTS

CHAPTER I **1**
INTRODUCTION **1**

CHAPTER II **3**
LITERATURE REVIEW **3**

2.1 Titanium and titanium alloys **3**
2.1.1 The properties and applications of titanium 3
2.1.2 Phases and structural of titanium 3
2.1.3 Alloying of titanium 4
2.1.4 Alpha titanium alloys 4
2.1.5 Beta titanium alloys 5
2.1.6 Alpha-Beta titanium alloys 6
2.1.7 Low-cost beta alloy and applications 7
2.1.7.1 TIMETAL LCB (Low-Cost Beta) 7
2.1.7.2 Applications of LCB 8

2.2 Solution treatment and aging (STA) of titanium alloys **9**

2.3 Tribological characteristics of titanium **10**

2.4 Surface Engineering of Titanium Alloys **11**
2.4.1 Surface Coatings 12
2.4.2 Surface Modification 12
2.4.2.1 Nitriding 12
2.4.2.2 Ion Implantation 13
2.4.2.3 Plasma electrochemical oxidation (PEO) 14
2.4.3 Thermal oxidation (TO) treatments 15
2.4.3.1 Thermal oxidation 15
2.4.3.2 The oxidation mechanism of titanium 16
2.4.4 Oxygen diffusion hardening 16
2.4.5 Duplex treatment 17

2.5 Surface property evaluation **18**
2.5.1 Scratch testing 18
2.5.2 Wear testing 18

2.6 Summary **19**

CHAPTER III **20**
EXPERIMENTAL METHOD **20**

3.1 Materials **20**

3.2 Sample preparation **20**
3.2.1 Cutting and grinding of samples 20

3.2.2 Design of Surface treatments 20
3.2.3 Preparing cross-sections 21
3.2.4 Etching of mounted samples 21

3.3 Characterisation 22
3.3.1 Microstructure 22
3.3.1.1 Scanning electron microscope (SEM) observation 22
3.3.1.2 X-ray diffraction (XRD) analysis 22
3.3.1.3 Transmission electron spectroscopy (TEM) 23
3.3.2 Chemical composition 24
3.3.2.1 Energy dispersive X-ray spectroscopy (EDX) 24
3.3.2.2 Glow discharge spectroscopy (GDS) 24
3.3.3 Mechanical properties 24
3.3.3.1 Surface and cross-section micro-hardness 24
3.3.3.2 Load bearing capacity tests 25
3.3.3.3 Scratch testing 25
3.3 4 Surface roughness measurement 25

3.4 Tribological properties 26
3.4.1 Ball-on-disc wear testing 26
3.4.2 Wear loss evaluation 26

CHAPTER IV 27
EXPERIMENTAL RESULTS 27

4.1 As-received material 27
4.1.1 Microstructure 27
4.1.2 Phase constituent 27
4.1.3 Compositions 27
4.1.4 Mechanical testing 28

4.2 Solution treated samples 28
4.2.1 Microstructure 28
4.2.2 Chemical composition 29
4.2.3 Surface Hardness 29
4.2.4 Selection of optimal solution treatment conditions 30

4.3 Solution treated and aged samples 30
4.3.1 Aging temperature effect on surface layer structure and properties 30
4.3.1.1 Microstructure 30
4.3.1.2 Chemical composition 32
4.3.1.3 Mechanical testing 33
4.3.2 Aging time effect on surface layer structure and properties 34
4.3.2.1 Oxide layer thickness 35
4.3.2.2 Hardness and load bearing capacity 35
4.3.2.3 Adhesion of surface oxide layers 36
4.3.2.4 Microstructures of the oxide layer 37
4.3.2.5 Surface roughness 38

4.4 Tribological assessment **38**
4.4.1 Tungsten carbide ball as counterpart 38
4.4.1.1 Under dry conditions 38
4.4.1.2 Under oil lubricated conditions 42
4.4.2 Hardened steel balls as counterpart 42
4.4.2.1 Under dry conditions 42
4.4.2.2 Under oil lubricant conditions 45
4.4.3 Comparison of wear tests 46

CHAPTER V **47**
INTERPRETATION & DISCUSSION **47**

5.1 Evolution of Treated Surface Cases **47**
5.1.1 Formation of surface oxide layers 47
5.1.2 Microstructure and bonding 49

5.2 The mechanisms of wear **50**
5.2.1 Dry sliding against WC balls 50
5.2.2 Dry sliding against steel balls 51
5.2.3 Effect of lubrication 53

5.3 Optimum treatment parameters **54**

CHAPTER VI **56**
CONCLUSIONS AND RECOMMENDATIONS FOR FUTURE WORK **56**

REFERENCES **60**

CHAPTER I

INTRODUCTION

The non-aerospace use of titanium alloys (such as in the motor sports industry) has become increasingly popular over the last 20 years due to their light weight, high ductility and high strength in conjunction with excellent corrosion resistance and outstanding biocompatibility. Titanium alloys are normally classified by their structure into the groups of alpha, near-alpha, alpha-beta, metastable beta and beta alloys. Advantages of β phase alloys include excellent workability, good hardening properties, high corrosion resistance and excellent fatigue/ crack propagation behaviour (Ivansishin et al., 2007). TIMETAL LCB (Ti-6.8Mo-4.5Fe-1.5Al) is a low-cost metastable beta (LCB) alloy developed specifically for non-aerospace (e.g. automotive) applications. TIMETAL LCB has been found to have a better combination of high strength (UTS>1500 MPa) and good ductility (total elongation >8%) than many other β alloys (Ivansishin et al., 2007).

However, it has been reported that the natural oxide film that forms on titanium and its alloys has been found to easily rub off, thus leaving the substrate in a state of high friction and low wear resistance (Dong & Bell, 2000). Consequently, titanium and its alloys are characterised by inferior tribological properties including a high and unstable coefficient of friction and a strong scuffing tendency (Dong et al., 1999). This is a problem for titanium and its alloys in all tribological applications, and surface engineering is an essential requirement for the tribological applications of titanium components.

To this end, many surface engineering methods have been researched to combat the poor tribological properties of titanium and its alloys. These range from surface coatings such as PVD and plasma electrolytic oxidation to surface modifications such as ion implantation,

plasma nitriding and thermal oxidation (Dong, 2010). However, there is little research on the surface engineering of TIMETAL LCB alloy within the current literature which is an issue needing to be addressed.

Research carried out by Dong and Bell (Dong & Bell, 2000) on the titanium alloy Ti-6Al-4V demonstrated the effectiveness of the thermal oxidation (TO) treatment in enhancing the wear resistance of the alpha/beta alloy. During the treatment, the titanium alloy surface was converted through controlled thermal oxidation processes into a diffusionally bonded ceramic (rutile TiO_2) layer and an oxygen strengthened diffusion zone underneath. Typical TO-treatment for most α+β alloys is normally carried out at about 600 °C in air for a long time (50-100h). However, this process cannot be directly applied to the TIMET LCB alloy since it is a metastable beta alloy. The long-time TO treatment at high-temperature will cause undue growth of the beta grains and excessive precipitation and growth of the alpha phase, thus leading to the degradation of the core mechanical properties of the β-alloy.

Therefore, the aim of this research was to enhance the tribological properties of TIMETAL LCB alloy without evoking a loss of core mechanical properties through developing new surface engineering processes based on integration of bulk heat treatment with surface ceramic conversion.

CHAPTER II

LITERATURE REVIEW

2.1 Titanium and titanium alloys

2.1.1 The properties and applications of titanium

Titanium and its alloys are recognised as maximising strength efficiency and metallurgical stability at high temperatures (Donachie, 2000). With its additional properties of low creep rate and predictable stress-rupture and low-cycle fatigue, titanium is ideal for use in rotating turbine and gas-engine blades, aircraft structural applications and high performance automotive and marine applications. Titanium and its alloys also possess excellent biocompatibility and corrosion resistance because of the formation of dense and adherent surface TiO_2 films and so for artificial joints and medical applications they are again the material of choice.

2.1.2 Phases and structural of titanium

Titanium can exist in two crystal structures, one in a hexagonal close-packed (hcp) formation and the other in a body-centred cubic (bcc). The first of which is known as alpha-titanium phase and the latter, beta-titanium phase. The beta phase is found only at very high temperatures, unless the titanium alloy is alloyed with specific elements. Titanium can exist also in a near-alpha phase (some beta present) and in an alpha-beta phase. The selection of titanium alloy primarily depends on which mixture of phases suits the desired application. Each has different behaviours and characteristics unique to the phase they exhibit. A titanium phase diagram is given in Fig. 2.1-1 (Wilkins group, 2006) illustrating the occurrence of the different titanium crystal structures at different

temperatures and pressures.

2.1.3 Alloying of titanium

Pure titanium has relatively low strength, which cannot be increased by heat treatment. To meet the wide application requirements, a number of titanium alloys with improved strength and heat resistance at elevated temperatures have been developed.

The addition of alloying elements divides the single allotropic transformation temperature for pure titanium into two temperature ranges (i) the alpha transus, below which the alloy is all alpha, and (ii) the beta transus, above which the alloy is all beta. Between them both phases are present. Both the alpha transus and the beta transus are functions of the concentration of the alloying elements. Some elements dissolve preferentially in the alpha phase and expand this field thereby raising the alpha-beta transformation temperature (alpha stabilisers) while others stabilise the beta phase by promoting lower temperatures (beta stabilisers). So alloying elements favour either the alpha or beta phase (or are neutral).

Correspondingly, the binary titanium alloy systems, and hence the phase diagrams, can be categorised into two major divisions-- alpha stabilised and beta stabilised systems, as presented in Figure 2.1-2 (Molchanova, 1965).

2.1.4 Alpha titanium alloys

Alpha alloys are stable at room temperature and contain α-stabilising elements such as Al or O. These α-stabilisers can increase the alpha-to-beta phase transformation temperature (Collings, 1984). The structure of alpha alloys is hexagonal close-packed (hcp) so forms a very high strength metal. Alpha alloys generally have creep resistance that is superior to β alloys, and are preferred for high-temperature applications. The absence of a ductile-to-

brittle transition, a feature of β alloys, makes α alloys suitable for cryogenic applications.

The close-packed structure gives α-Ti a packing density of K_{hcp}=0.74 compared to K_{bcc}=0.68 for β-Ti. This means that the diffusion rate of oxygen in β Ti is much quicker than that involving α-Ti. However, a greater number of interstices in α phase titanium mean it can absorb a higher amount of oxygen in solution and deep case hardening; hence achieving a higher hardness value than α+β or β phase alloys (Ma, 2004). Alpha alloys may not be suitable in some applications due to their tendency for forging defects. Also, unlike β alloys, α alloys cannot be strengthened by heat treatment because they are single-phase. They are used most often in the annealed or recrystallized condition to eliminate the residual stresses caused by working (Destifani, 2002).

2.1.5 Beta titanium alloys

Metastable beta alloys have a body-centred cubic (bcc) structure. They are not naturally thermodynamically stable below 883°C but when a β phase stabilizer element such as vanadium or molybdenum is added in quantities in excess of a critical amount, the structure at room temperature will remain entirely β phase. These stabilising elements work by lowering the temperature of the α to β phase transition, thus promoting the development of the bcc β phase. Some alloys with β-stabilizing elements below this critical amount can be cooled rapidly from above the α+β to β transus temperature to retain a metastable structure of β phase at room temperature. This is the state that nearly all beta alloys are in and so even though they are only ‘near- β’ they are still referred to as simply ‘β alloys’. Since the β alloys have a metastable microstructure, they tend to transform into a balance of the two structures under atmospheric temperature and pressure. Their strength is derived from the intrinsic strength of the beta structure plus the precipitation of alpha

and other phases from the alloy through heat treatment. However, due to the microstructural instability of these alloys, their use is limited to below about 250 °C (Weiss, 2004). Advantages of β phase alloys include excellent workability, good hardening ability, corrosion resistance and excellent fatigue/ crack propagation behaviour (Ivasishin et al, 2007). The small β grain size and the bcc structure also determine their high formability which is their main advantageous property and ideal for applications such as suspension springs in automobiles. Beta alloys have excellent hardening properties, and respond readily to heat treatment. A common heat treatment involves solution treatment followed by aging at temperatures of 450 to 650 °C (850 to 1200 °F). This treatment results in formation of finely dispersed α particles in the retained β phase (Destifani, 2002).

However, a disadvantage of β alloys is that the solubility of oxygen in this phase is limited compared to the other phases due to there being fewer interstices in the cubic lattice (Ma, 2004). As previously mentioned, their lower atom packing density means they have a high rate of oxygen diffusion but low overall oxygen solubility.

2.1.6 Alpha-Beta titanium alloys

The α+β alloys combine both the α and β phase microstructures. These dual-phase Ti alloys form the deepest hardened layer since the α-Ti aids in preparing the oxygen to form solid solution and the β-Ti promotes the inward diffusion of oxygen to the inner layer. α + β alloys generally have good formability and their properties can be controlled through heat treatment by adjusting the morphology and distribution of retained β phase present. Solution treatment followed by ageing at 480 to 650 °C (900 to 1200 °F) precipitates α Ti, resulting in a fine mixture of α and β in a matrix of retained or transformed β phase (Destifani, 2002).

2.1.7 Low-cost beta alloy and applications

2.1.7.1 TIMETAL LCB (Low-Cost Beta)

The chemistry, Ti-4.5Fe-6.8Mo-1.5Al, of the proprietary LCB alloy, was designed to achieve beta phase stability at room temperature with the least amount of expensive alloying elements, thus conferring a cost advantage compared with other beta alloys. A reduced cost of raw material was achieved by stabilising the beta phase using an inexpensive FeMo master alloy widely used in the steel industry. A small amount of aluminium was also added to increase the strength of TIMETAL LCB via solid solution hardening and precipitation hardening of alpha grains during the aging process since aluminium is a strong alpha stabiliser. Using carefully selected amounts of low-cost alloying elements can produce a material with very similar qualities to other beta alloys but with a much lower cost, therefore making it more marketable. Indeed, LCB is even cheaper than Ti-6Al-4V α+β alloy since the expensive vanadium was replaced by iron, allowing less-expensive Fe-Mo master alloys to be used.

In addition to the cost advantages, LCB distinguishes itself from other beta alloys with an unusually high strength potential, which enables strengths of approximately 1350MPa concurrent with a sufficient high ultimate strain. This alloy is cold formable in the β microstructure and can be aged to high strengths by precipitating the α phase. This is done by aging the alloy at temperatures in the range of 30 to 100°C (55 to 180 °F) below the transus temperature which then causes the α phase to precipitate. In this condition, the alloy has a yield strength greater than 900 MPa (130 ksi) and a tensile elongation of about 18% (Weiss, 2004), which compares favourably with high strength steels.

2.1.7.2 Applications of LCB

The beta alloy TIMETAL LCB (Low-Coat Beta) was developed for non-aerospace and automotive spring applications in particular. This has been found to have a better combination of high strength (UTS>1500 MPa) and good ductility (total elongation >8%) than many other β alloys (Ivasishin et al, 2007). This combination of cold formability and high strength makes this alloy a potential replacement for most steel components in the automotive industry such as suspension springs, valve springs and bolts.

For example, Formula 1 racing cars, racing motorcycles and high-performance cars have made the advantages of LCB springs. This is mainly because the mass of an axle coil spring is proportion to the product of density and shear modulus. It is known that the shear modulus and density are much lower for titanium alloys than for steels (Kosaka et al., 2005), and effective weight reduction of 40-50% can only be attained through the replacement of steel springs with titanium ones (Leyens and Peters, 2003). As a beta alloy, the shear modulus of LCB is lower than that of standard α+β alloys, thus further reducing the mass of LCB springs.

Another potential application area lies in biomedical devices because of the outstanding biocompatibility and excellent corrosion resistance of titanium and its alloys. Currently, the workhorse alloy, Ti-6Al-4V, has been used for several body implants. It is expected that the biocompatibility of LCB should be better than Ti-6Al-4V. An advantage of adding iron to titanium is that it increases biocompatibility. Titanium naturally has an inherent inertness in the human body which means it can be safely used for surgical implants and prosthetic devices. Adding Fe, Nb, Zr or Ta enhances this characteristic and so increases the safety factor (Bloyce et al., 2002). In addition, beta alloys have a lower modulus than alpha and

alpha/beta alloys. Therefore, stress shielding effect caused by the difference in modulus between bone and load-supporting implants could be reduced by using LCB.

2.2 Solution treatment and aging (STA) of titanium alloys

Named STA for short, this two-step procedure is often carried out for some Ti alloys to increase their mechanical properties (in particular strength). The temperature for solution treatment (850 °C) was chosen due to it being around 40 °C below the beta-transus, which is the suggested temperature in the literature (Williams & Starke, 1984 and Kosaka et al., 2005).The solid solution treatment followed by aging effectively precipitates the fine alpha-phase particles in the beta matrix phase. The volume fraction and morphology of the alpha precipitates control the strength level, while the beta grain size has a strong effect on ductility (Ivasishin et al., 2003). Solution treatment also works to homogeneously distribute alloying elements into the beta phase; thus ensuring uniform mechanical properties. STA is used with α+β and β alloys to ensure the necessary strength required of this material. An accepted temperature selection for solution treatment is 40 °C below the β transus and then a cold-water quench (Williams & Starke, 1984). If the temperature exceeds the beta transus, the fine grain structure of TIMETAL LCB alloy is lost which reduces strength and increases ductility (Kosaka et al., 2005). In a documented experiment with TIMETAL LCB, solution treatment was carried out for 0.5hrs (Ivasishin et al., 2005). The immediate water quenching after the treatment was reported to produce a relatively coarse β grain size of approximately 200μm. The Ti6Al4V alloy requires a much longer duration of solution treatment to obtain the same strength increase. Documented experiments consistently treat this alloy for 60 hour periods (Guleryuz & Cimenoglu, 2005).

Aging involves further heat treatment, often at a lower temperature and for a longer time, without the final quenching which introduces alpha precipitates back into the bulk material, thus regaining the strength lost from solution treatment. TIMETAL LCB was aged at 811K (538 °C) for 0.5-8 hours in Ivasishin's work (Ivasishin et al., 2005). It was found that a slow heating rate of 0.25 K.s-1 (0.25°C.s-1) produced a finer, more uniform microstructure than when a rate of 20 K.s-1 was used. The slower heating rate also resulted in higher tensile strengths of LCB compared to the faster rate due to coarse α plates produced in this method. The same temperature (538 °C) was found to produce the best age when done for 4 hours by Kosaka et al. (2005).

2.3 Tribological characteristics of titanium

Titanium and its alloys have a considerable drawback in that they have poor surface properties when in a tribological environment. The natural oxide film that forms on titanium has been found to easily rub off, leaving the metal in a state of poor friction resistance and poor wear resistance (Dong & Bell, 2000). This is a problem in all tribological applications and so greatly limits titanium and its alloys from being used in an untreated condition. Inferior tribological properties include high and unstable coefficient of friction against a harder counterface material and a strong scuffing tendency (Dong, 1999). The reasoning for this stems from three physical properties of titanium and its alloys: their electron configuration, their incompatibility with lubrication aids and their inherent crystal structure (Dong & Bell, 2000). The electron configuration is such that extremely high chemical activity occurs within titanium. This increases the potential for new covalent bonds to form and hence, high adhesion strength is caused between surfaces in tribological contact. The ineffectiveness of lubrication is thought to be caused partially by the low heat

conduction and surface oxide films of titanium and its alloys. Metal-on-metal direct contact is therefore present leading to a large friction coefficient and a high tendency to scuffing. Also, the crystal structure of titanium lends itself to high ductility and plastic flow due to having nine possible slip systems (Dong & Bell, 2000). This leads to considerable junction growth during adhesive wear.

Due to the poor tribological properties of titanium, wear during motion is a real problem. Wear occurs when two surfaces are interacting in motion and may be defined as the loss of material from one or both surfaces. Five main different mechanisms of wear exist: adhesion, abrasion, third body, fatigue and corrosion (Schmalzreid et al., 1999). Adhesion and abrasion are the two most likely to affect the ceramic rutile layer on heat treated titanium (Buckley & Miyoshi, 1984).

Adhesive wear occurs when the atomic forces occurring between the materials of two surfaces under loading are stronger than the inherent material properties of either surface (AAOS, 2001). Abrasive wear occurs between two surfaces of different relative hardness. Micro-roughened regions and small asperities on the harder surface locally plough through the softer surface. This mechanism of wear results in the softer material being removed by the track traced by the asperity during the motion of the harder surface (AAOS, 2001).

2.4 Surface Engineering of Titanium Alloys

The surface engineering of titanium alloys must be developed and carried out to ensure the longevity of tribological parts (Bell, 1987). This is not as straight forward as just increasing the surface hardness since wear resistance has been found not to be proportional to mechanical properties such as hardness and ultimate tensile strength of the alloy (Li et al.

2004). Increased hardness may even decrease the wear resistance of a titanium alloy due to the wear mechanism changing from plastic deformation to brittle fracture of the surface (Feng, 2008).

Many different surface engineering techniques exist to improve a wide range of material properties. These can be split into surface coatings which are just a layer of new material added to the substrate surface; and surface modification which actually changes the compositions and/or microstructure of the substrate to produce the improved surface property.

2.4.1 Surface Coatings

Physical vapour deposition (PVD) can be carried out via a variety of processes to deposit metals, alloys, compounds, or metastable materials onto a substrate. The most successful engineering application is the coating of tool material substrates by reactive ion plating or reactive sputtering of TiN and related materials (Bloyce et al., 2002). The PVD treatment of titanium alloy substrates has found limited application so far, but arc evaporation has been used to deposit 4.5 μm of TiN, and sputter deposition has been used to deposit 0.5 μm of TiN on gears for space mechanisms (Bloyce et al., 2002).

2.4.2 Surface Modification

2.4.2.1 Nitriding

Nitrogen has a high solid solubility in α-Ti and the strength increase imparted by the interstitial nitrogen is significant (Bloyce at al., 2002). The compound of Ti_2N is formed at temperatures below 1100 °C (2010 °F) and has a tetragonal crystal structure with a

hardness of 1500 HV. At nitrogen contents higher than 12wt%, TiN with a NaCl-type crystal structure and a hardness of 2200- 2500 HV is formed. Nitriding aims to produce a thin compound layer of TiN at the surface above a thicker compound layer of Ti_2N, which is above a diffusion zone of nitrogen-strengthened titanium. The surface differs from that achieved through oxidizing in that a useful, hard compound layer structure is present. Nitriding cannot be achieved in air because of the tendency of titanium to form TiO_2 in preference to either of the nitrides. Instead, it is achieved in a nitrogen gas atmosphere or alternatively in a nitrogen plasma. A type of nitriding that proceeds by glow discharge methods is used to harden biomedical parts. Under this method a fourfold rise in hardness of grade 5 titanium and an eightfold rise in hardness of grade 3 titanium are possible, when using cathode nitriding under a supporting screen (Fraczek, 2009).

2.4.2.2 Ion Implantation

Wear resistance of titanium and titanium alloys may be improved by ion implantation of interstitially-located species such as nitrogen or carbon. This involves the acceleration of ions at a sufficiently high velocity to allow them to penetrate the surface of the substrate material being implanted. Implant layer thicknesses vary with many different factors but they typically exist up to several hundred nanometres. An increase in near-surface hardness allows the material to resist plastic deformation and support the oxide layer at higher stresses. The improvement in wear resistance however can only be achieved under light loads because of the extremely thin modified layer. A threefold increase in Vickers micro-hardness at loads of 1 to 2 g can be achieved in these alloys (Sioshansi, 1990). There are three mechanisms from which hardening of ion-implanted titanium arises: ion-induced damage, solid solution hardening, and precipitation hardening (Bloyce et al. 2002). Ion-induced damage arises from the creation of a dense network of dislocations similar to that

achieved during cold working or in shot peening. Solid solution hardening may be achieved by either substitutional or interstitial alloying elements. Precipitation hardening is effected by dislocations being pinned by coherent or incoherent precipitates. For the maximum precipitation hardening effect, a fine distribution of coherent precipitates is required. The magnitude of ion dosage dictates the effect achieved. For very low ion doses, damage-induced hardening effects dominate; for intermediate doses, solid solution hardening becomes dominant; for high doses, precipitation hardening dominates.

2.4.2.3 Plasma electrolytic oxidation (PEO)

Plasma electrolytic oxidation (PEO) is an advanced form of anodic electrochemical conversion that utilises an electrolytic plasma discharge to produce oxide ceramic layers (Yerokhin, et al. 2003). During the PEO process, oxide film formation is influenced by plasma microdischarge events (Figure 2.4-1, Khan R.H.U. 2008) which provide multiple heating/cooling cycles to the surface, affecting the film structure, phase composition and stress state. The microdischarge characteristics can be controlled by the PEO process parameters e.g. applied current mode, current densities and electrolyte concentrations. Plasma electrolytic oxidation (Yerokhin, et al. 2003) has attracted considerable attention due to its major advantages such as environmental friendliness, capability of fabricating oxide films with controlled morphology and composition, good adhesion to substrate, wear- and corrosion-resistance. These advantages allow the consideration of PEO as an alternative to conventional acid-based anodising processes for Ti and its alloys. PEO coatings on titanium are of interest in biomedical applications, since they impede release of metal ions and assist tissue development (Yerokhin, et al. 2000). PEO coatings on Ti can contain amorphous and crystalline titania constituents, with the latter normally being in the form of anatase and/or rutile (Teh, 2003).

2.4.3 Thermal oxidation (TO) treatments

2.4.3.1 Thermal oxidation

Thermal oxidation (TO) involves titanium being heated in an oxygen containing atmosphere for a period of time. This introduces oxygen into the titanium to create a hardening effect. Unfortunately at a temperature high enough (850-1000°C) to achieve an appreciable hardening effect, a considerable amount of surface scale is also formed (Hanzel, 1954). A further study however, heated titanium in air at 550 °C for 17 hours and found that the friction coefficient markedly decreased and remained low after the removal of the brittle compound layers. (Machlin & Yankee, 1954, Yankee & Machlin, 1954)

To overcome this, Dong et al. (1996, 1997a) developed a novel surface treatment based on TO. Results showed a significant decrease in the friction and wear of the Ti-6Al-4V alloy. The wear rate of the TO treated specimen was reduced by more than 2 orders of magnitude from the untreated metal. It was postulated that the TiO_2 rutile lowered the plastic deformation and shear strength of the surface to result in a lower friction coefficient. Similar, an oxide of Nb_2O_5 formed on Ti-29Nb-13Ta-4.6Zr and was found to have very good lubricating properties. Nb has a higher affinity to interstitial oxygen; therefore Ti-29Nb-13Ta-4.6Zr is an easier surface to oxidise than Ti-6Al-4V. The parameters for thermal oxidation of titanium depend largely on the microstructure. For grade 2 Ti, an α phase alloy, thermal oxidation to produce a rutile structure was achieved at 550 °C for 70 minutes in a standard laboratory atmosphere (Eisenbarth, 2002). Thermal oxidation has been carried out on the common Ti6Al4V α+β phase alloy with parameters ranging from 150 °C for 1 hour in air (Lausman, 1995) to 650 °C for 100 hours in an O_2/N_2 controlled atmosphere.

2.4.3.2 The oxidation mechanism of titanium

The mechanism of oxidation of titanium has been found to be very complex and vary greatly due to different temperatures and pressures. The main reason for these diverse phenomena is the high oxygen solubility of titanium and the resulting competition between oxide film formation and oxygen dissolution effects (Kofstad et al., 1958).

From a thermodynamic reasoning, one might expect a layered oxide scale to form; changing from TiO near the metal/oxide phase boundary to Ti_2O_3 and then TiO_2 at the outer oxide scale. The amounts of each oxide would also then be assumed to follow the Wagner theory of oxidation so be dependent upon the rate of formation of the independent oxides. In fact, both X-ray diffraction and metallographic studies have shown that the oxide scale is made up entirely of just the rutile TiO_2 phase and any TiO or Ti_2O_3 that forms is in amounts smaller than a few percent (Kofstad et al., 1958).

The following diffusion of oxygen into the titanium metal is thought to be facilitated by oxygen ion vacancies in the rutile layer. Consequently, it is thought that the inward diffusion of oxygen from the outer layer of the oxide might be expected to determine the rate of oxidation of titanium (Kofstad et al., 1958).

2.4.4 Oxygen diffusion hardening

Thermal oxidation treatments were found to be suitable only for low to medium loads and deep case hardening is necessary for high load-bearing applications.

Higher temperatures or longer treatment times of TO are often not effective in hardening titanium alloys as they render the metal commercially unviable due to scaling and stratification (Dong, 1999). Therefore, oxygen diffusion (OD) has been developed as an

alternative surface modification. This produces a dense adherent oxide layer onto the surface, followed by a high temperature vacuum diffusion treatment of the oxygen from the layer into the substrate. A hardened case of about 200μm is able to be formed; 20 times that of the TO layer. Oxygen diffusion hardening (ODH) of Ti-6Al-7Nb alloys results in a gradation in hardness from the surface to a depth of 50 μm. The maximum hardness is 900 HV, compared with 360 HV for the untreated alloy. However, the corrosion resistance of the ODH- treated titanium alloy is only equal to that of commercially pure titanium and untreated Ti-6Al-7Nb alloy (Streicher et al., 1991). An advanced oxygen diffusion process known as Tifran has been found to produce gears that exhibit the best wear resistance and the lowest power losses, compared to other surface treated components (Gaucher & Zabinski, 1975).

2.4.5 Duplex treatment

It should be pointed out that under a high load and/or at a high sliding speed, severe adhesive wear can still occur. This is because although the ODH can produce a deep hardened case, it is at the price of dissociating the surface oxide layer formed in the first oxidation stage, which is effective in combating adhesive wear and galling of titanium and its alloys.

It follows that it is wise to use a duplex treatment which combines the deep case hardening with a surface layer such as diamond-like coating (DLC) or TiO_2 rutile. Both these materials have a high hardness and very low friction coefficients, making them ideal for distributing stresses evenly and preventing damage. Dong et al. (1998) designed such a treatment and found it to be effective in increasing the load-bearing capacity of Ti6Al4V fivefold. Weight-loss measurements, SEM images and X-ray mapping were used to

systematically characterise the enhanced tribological properties of the treated alloy and all confirmed the increase in material performance over untreated material and a steel counterpart (Dong & Bell, 2000).

2.5 Surface property evaluation

2.5.1 Scratch testing

Measuring the fracture toughness of the oxide film is difficult due to the thinness of the ceramic layer. There is also no standard procedure for this kind of measurement currently published (Zhang et al., 2005). The scratch test is a simple means of assessing adhesion strength of a film on a substrate. A diamond indenter is drawn across the coated surface under a progressively increasing load. The critical load is quantified when a well-defined failure event occurs. If the failure mechanism is by coating-substrate separation, then this gives a qualitative measure of the coating-substrate adhesion level. However, other failure modes can also occur which depend on plastic deformation and failure within the coating itself (Bull, 1991). This is additional useful information when deducing the quality of the coating so visual observations need careful recording.

2.5.2 Wear testing

Tribological behaviour of surface engineered materials can be evaluated by laboratory wear tests under simulated service conditions. Wear tests can include variables such as: counterpart material, sliding speed, applied load, orientation of sample, lubrication, humidity level, surface preparation, number of cycles and temperature (Divakar & Blau, 1992). Existing wear tests include: pin-on-disc, ball-on-flat, block-on-ring and rolling four-

ball apparatus (Divakar & Blau 1992). There are also numerous specific application tests that attempt to replicate in-vivo situations. For testing an oxide film, pin- or ball-on disc testing has been found suitable and the ASTM gives the standard test method for wear testing with a pin-on-disk apparatus (ASTM standard).

2.6 Summary

This literature review covers the physical metallurgy, the properties and application, the tribological behaviour of titanium and its alloys and LCB alloy in particular. This review reveals that titanium and its alloys are characterised by poor tribological properties in terms of high friction and wear. Thermal oxidation treatment has been developed to address this problem and TO treatments of such α+β alloys as Ti-6Al-4V has achieved great success; however, little or no work has been conducted to apply the thermal oxidation treatment to beta alloys since this process cannot be directly applied to β-alloys. Clearly, this is an important research topic from both a scientific and technological point-of-view, which forms the theme of this MRes study.

CHAPTER III

EXPERIMENTAL METHOD

3.1 Materials

The substrate material used for research purposes was TIMETAL LCB titanium alloy supplied by Titanium Metals Corporation. It had been previously solution treated at 850 °C and then aged for 4 hours at 565.5 °C. The nominal composition of the material was (wt %): 6.8%Mo, 4.5%Fe, 1.5% Al and balance Ti.

3.2 Sample preparation

3.2.1 Cutting and grinding of samples

A rod of 27mm in diameter was cut into 5mm sections to produce the coupon samples (Fig. 3.2-1). A Struers Accutom-5, version 2 saw was used, coupled with an abrasive silicon carbide blade turning at 3000 rev min-1. Standard sample preparation procedure was used to grind the surface of the samples up to 1200 grit, after which they were cleaned with acetone and dried under hot air.

3.2.2 Design of Surface treatments

As discussed in Chapter II, thermal oxidation is known to produce a hard and wear resistant oxide layer on an oxygen diffusion hardened case on the surface of alpha + beta alloys. However, prolonged (50- 100h) exposure to high temperatures (600-650 °C) compromises the mechanical properties of the LCB alloy because of the potential undue growth of its grains at high-temperature due to its metastable beta nature. Therefore, a new

surface engineering approach tailored for beta titanium alloys has been designed by combining solution treatment (ST) and aging with thermal oxidation treatment.

For solution treatment, samples were loaded into an Elite electric furnace, heated at a ramp rate of 10 °C/min from 23 °C to 850 °C and then held for either 0.5 or 6 hours. Immediately after the holding time finished, samples were removed from the furnace and dropped into cold water for quenching.

Solution treated samples were then aged at 500, 550 or 600 °C for 8 hours. The preliminary evaluation of the quality of the surface oxide layer revealed that the 500 °C aged samples showed the best surface oxide layer among these aged samples. Therefore, in order to identify the optimal aging time, some samples were aged at 500 °C for 4, 16 or 32 hours. A summary of the treatment matrix and sample codes is given in Table 1 and the treatment order procedure is given in Fig. 3.3-2.

3.2.3 Preparing cross-sections

Metallographic cross-sections of the treated samples were prepared by cutting using the same machinery used to cut the coupon samples. A slow feed rate (0.08mm s-1) and a cooling lubricant ensured that alterations to the treated surfaces were minimized. These were then mounted in conductive Bakelite using a MET-PREP PA 30 Mounting press.

These cross-section samples were ground down to 1200 grit and polished using 6μm and 1μm diamond paste and finished with ½ μm polishing using colloidal silica. Samples were then cleaned with distilled water and acetone.

3.2.4 Etching of mounted samples

Etching of the cross-sections revealed the microstructure and allowed for SEM observation of the oxide layer and diffusion zone. An etching solution of 2% HF, 10% HNO_3, and 88% H_2O was used. The required etching time was judged by eye to the point when the shiny appearance turned dull. For many samples, this was a very rapid process with the surface apparently turning black immediately, so it was necessary to transfer the stub into water as quickly as possible.

3.3 Characterisation

For analysing and characterising the effects of each treatment, a range of materials characterisation techniques were used. These were split into three categories: i) microstructure, ii) phase and chemical composition and iii) mechanical properties.

3.3.1 Microstructure

3.3.1.1 Scanning electron microscope (SEM) observation

A Phillips XL-30 microscope was used for observation of different microstructural features under magnifications of 100x to 4000x. Sample surfaces, grain boundaries and size of grains were examined. After heat treatment, cross-sections of all specimens were taken and used to observe the oxide layer and oxygen diffusion zone (ODZ).

3.3.1.2 X-ray diffraction (XRD) analysis

A Philips X'pert X-Ray Diffractometer was used to carry out phase analysis of the 'as-received' samples and phase identification of the treated samples. The machine scanned over a range of 2θ between 20-100° C. The X-Pert Highscore program was used to identify

diffraction peaks for indication of the phase and/or elements and compounds present. These were identified through comparison with the internal database (PDCPFWIN).

After initial analysis of the results, it was decided that the top oxide layer should be removed and a secondary set of XRD results collected to identify phases at the interface between the top oxide layer and the sub-surfaces. To do this a micro-hardness machine was used. For each sample, the thickness of the oxide layer was known from SEM analysis and this was termed the target depth. Four indents at the depths (V) closest to the target were made at four corners of an imaginary square filling the disc face of each sample. 'V' was calculated by using the model: 'the diagonal of the indent is equal to 7 times its depth' (Fig. 3.3-2). Having four indents allowed the oxide layer to be polished off more evenly. The samples were then analysed for a second time using XRD.

3.3.1.3 Transmission electron spectroscopy (TEM)

Two slabs with a cross-section area of 2.2x2.2 mm^2 were cut from the sample STA500_8 and glued with G-1 epoxy (Gatan product) in such a way that treated surfaces were facing each other. This assembly was sliced to ~1mm thickness and ground and polished to 50 μm by using SiC paper from 600# to 1200# and 6 μm diamond paste. Then thin assembly was carefully fractured away from glued centre using tweezers, ensuring that on both slices, the coating was adherent on the surface for further thinning. A schematic of this pre-thinning preparation is shown in Fig. 3.3-3.

One of the pre-thinned two slices was then transferred to a Quanta 3D FEG focused ion beam (FIB) miller for final thinning to 100nm. Prior to milling, tungsten coating was deposited along the surface of the region where the sample was to be thinned in order to promote uniform milling and preserve the coating structure, as shown in Fig. 3.3-4. Rough

mills were performed with beam currents from 50 nA to 5 nA at 30 kV and fine thinning was achieved using beam currents 1 nA ~ 0.1 nA at 30 kV. A final polish at 5 kV 48 nA for few minutes completed the process, cleaning any artificial features, such as superficial amorphous layer caused by the ion beam thinning under high beam currents.

A JEOL JEM-2100 LaB_6 transmission electron microscope and FEI Philips TECNAI F20 with the operating voltage of 200 kV was used to characterise the phase constituent and microstructure of the coatings.

3.3.2 Chemical composition

3.3.2.1 Energy dispersive X-ray spectroscopy (EDX)

An Oxford EDX, model 6650 connected to the Phillips XL-30 SEM was used to study the composition of the grain-boundaries on the 'as-received' samples and the wear scars caused by wear testing. INCA computer software was used.

3.3.2.2 Glow discharge spectroscopy (GDS)

A Spectrumat GDS-750 machine was used for probing concentration depth distribution of chemical elements. A controlled stream of ions was bombarded the sample surface and the atom excitation and emissions were then analysed by the spectrum wavelengths produced. These wavelengths are specific to the elements from which they came and so element concentration versus depth data can be collected after careful calibration.

3.3.3 Mechanical properties

3.3.3.1 Surface and cross-section micro-hardness

A Mitutoyo MVK-H1 hardness testing machine was used with a Vickers indenter at 100g

load for microhardness measurements. Surface hardness was taken of the ‘as-received’ samples. It was found that the oxide layer cracked under a load of 100g so could not give valid data for surface hardness. However, when this oxide layer was removed the hardness of the oxygen hardened case could be found. Polished cross-sections of the samples were used to generate hardness-depth profiles from the oxygen diffusion zone beneath the top oxide layer.

3.3.3.2 Load bearing capacity tests

Load bearing capacity tests gave the critical load at which the oxide layer cracked. A Vickers indenter was used to apply loads from 10g to 1000g. To avoid interference among neighbouring indentations, the interspacing between neighbouring indentations was about 1.5 times of the diagonals of the indentations. At each load, three indentations were inserted and the average value taken.

3.3.3.3 Scratch testing

Scratch tests were conducted to assess the bonding of the oxide layer to the hardened substrate on samples STA500_4, STA500_8 STA500_16 and STA500_32. A Rockwell diamond indenter with a 200μm radius tip was used. Tests were conducted at a linear velocity of 10 mm/min and loading rate of 100 N/min from 0.5 to 40 N.

3.3 4 Surface roughness measurement

Surface roughness measurements were carried out using an Ambios Technology XP-200 machine and the Ambios Profiler computer program to examine the effect of surface treatment on the surface roughness.

3.4 Tribological properties

3.4.1 Ball-on-disc wear testing

Reciprocating ball-on-disc sliding wear tests on STA500_4, 8, 16 and 32 were conducted using the TE79 multi-axis tribology machine. Sets were carried out with two different counterparts; an 8 mm tungsten carbide ball and an 8mm hardened steel ball, and two different environments; dry and engine oil lubricated. One drop of engine oil was administered for each test using a plastic pipette. Loads used were 1, 5, 10 and 20 N. Tungsten carbide was used as this material is extremely hard so hardly any wear occurs on the ball; therefore it is commonly used for comparison between components. Hardened steel was used as it would be a likely in-vivo pairing with the LCB alloy. All tests used a sliding distance of 10mm and an average sliding speed of 10 $mm.s^{-1}$.

3.4.2 Wear loss evaluation

The resultant wear tracks were measured using a profilometer and the wear loss was calculated by integrating the cross-sectional area of the wear track and then mulitipying by the length of wear track. The coefficient of friction was calculated according to the recorded friction force and the applied normal load. More detailed and 3D cross-sections of wear tracks were obtained using a Ambios Technology XP-200 machine and the program 'Ambios Profiler (XP-Plus Stylus).' This gave a less 'average' picture of the wear track than the 2D profile so was used to check the 2D profiles were correct recordings. Post-examination of the wear tracks was carried out with the SEM to investigate the wear mechanisms involved.

CHAPTER IV

EXPERIMENTAL RESULTS

4.1 As-received material

4.1.1 Microstructure

The microstructure of as-received TIMETAL LCB was observed under SEM and it can be seen from Figure 4.1-1 that the microstructure consisted of alpha precipitates within a beta matrix. The alpha precipitates were most evident at grain boundaries as the black areas but are also distributed throughout the grey beta areas. This is in line with the solution/ageing heat treatment conditions for the as-received material.

4.1.2 Phase constituents

XRD charts revealed both alpha and beta peaks (Fig 4.1-2), supporting the SEM observations (Figure 4.1-1). There appeared to be a shift to the right of the beta titanium peaks from the standard position. This effect was caused by the smaller atoms of Mo and Fe within the Ti alloy reducing the lattice parameters. The atomic radius of titanium is 144.8pm whereas iron has a radius of just 126.0 pm and molybdenum a radius of 138.0 pm. This means that the d-spacing would decrease when titanium atoms are partially substituted by these relatively small atoms. The *d*-spacings for the first four beta peaks of the LCB alloy are given in Table 2.

4.1.3 Compositions

EDX analysis confirmed the given composition of TIMETAL LCB from the Titanium Metals Corporation chemical analysis test sheet.

EDX was then used to measure the composition of the alpha and beta phases as shown in SEM micrographs (Fig 4.1-3a). Point analysis was used to probe the elemental composition of two spots; one on a black area and one on a grey area. This confirmed that the black precipitates at the grain boundaries were alpha titanium since it contained lower amounts of the beta stabilisers of molybdenum and iron (Fig 4.1-3b).

4.1.4 Mechanical testing

No initial mechanical testing took place apart from micro-hardness indentations of the untreated coupon surface that gave an average Vickers hardness value of 502$Hv_{0.1}$.

4.2 Solution treated samples

4.2.1 Microstructure

Visual observation revealed partially spallated oxide layers on the long-time (6h) solution treated ST6 sample. Figure 4.2-1 shows a typical SEM picture of the surface morphology of the ST6 sample. No such spallation was observed for short-time (0.5h) solution treated ST0.5 sample. SEM observations revealed that no great change was present between the grain structure of ST0.5 and ST6 (Fig. 4.2-2). In both samples, the clear alpha-titanium areas at the grain boundaries of the as-received microstructure (Fig. 4.1-3) were no longer evident, as the alpha phase was dissolved during the solution treatment and the quenching kept the beta phase to the room temperature (Donachie, 2000).

Cross-section SEM images showed the oxide layer, oxygen diffusion zone (ODZ) and the grain structure of the substrate material (Fig. 4.2-3). It can be seen from Fig. 4.2-3 that the microstructure beneath the surface oxide layer differs greatly from that of the substrate with some secondary phase grains in the beta matrix. This is most probably alpha phase

formed during the solution treatment when oxygen diffused into the beta matrix since oxygen is an alpha stabiliser (see Section 2.1.2). This is confirmed by XRD analysis (Fig.4.2-5).

The sample treated for 0.5 hours had an average ODZ thickness of 61 μm and a maximum thickness of 105μm was recorded (Fig. 4.2-3a). The sample treated for 6 hours had an average ODZ thickness of 117μm with a maximum of 149μm (Fig. 4.2-3b). This is shown graphically in Figure 4.2-4. Clearly, the thickness of the ODZ increased with the solution treatment time.

XRD patterns from AR and ST0.5 revealed that the oxide formed was TiO_2 as expected (Fig. 4.2-5). Also noticeable was the decrease in peak intensity of the α-titanium. This is the result of the quenching process, which retards the α precipitate.

4.2.2 Chemical composition

The GDS composition depth-profiles of ST0.5 reveal a strong presence of aluminium in the first micron of the sample surface (Fig. 4.2-6). It is known that TiO_2 can only contain a very small amount of Al, which is likely to be pushed out of the rutile layer; either back into the substrate or onto the surface.

4.2.3 Surface Hardness

There was no significant difference in micro-hardness between the two different samples (Fig 4.2-7) even though the ODZ in ST6 was so much greater. These hardness values were taken from the samples where the oxide layer had been carefully removed in order to gain a true understanding of any effects the heat treatment may have had on the underlying metal.

Figure 4.2-7 also shows the hardness values from the AR samples. The decrease in hardness seen from the ‘as-received’ material to the solution treated samples is due to the solution treatment. The ‘as-received’ alloy was naturally precipitation hardened by ageing. This effect is lost after solution treatment because the high temperature heating caused the alpha phase precipitates to be dissolved back into the beta phase. However, this process is necessary because it forms the beta phase of the alloy before aging. Therefore, one of the reasons for aging is to reintroduce the alpha precipitates after the solution treatment.

4.2.4 Selection of optimal solution treatment conditions

Solution treatment at 850 °C for 0.5 hours was chosen as the optimal solution treatment. This is because it produced a far better surface finish and bonding of the rutile oxide layer to the substrate surface. Even though a far larger ODZ was formed after six hours, the hardness was not increased significantly. This suggests that a short solution treatment time is fully acceptable, both for hardness and for surface quality.

4.3 Solution treated and aged samples

4.3.1 Aging temperature effect on surface layer structure and properties

4.3.1.1 Microstructure

SEM images were taken of the edge cross sections from each sample to allow comparison of the oxide layer thickness and structure of the oxidation diffusion zone at different magnifications (Figs. 4.3-1a, b & c). Spallation of surface oxide layers was observed for high-temperature aged samples (Fig. 4.3-1b). The thickness of the oxygen diffusion zone increased only very slightly with the longer aging time (Fig 4.3-2). A clear trend emerged

of a gradual increase in rutile layer thickness with the longer aging time but effectively the same ODZ thickness. The values from the ST0.5 sample are given for comparison.

Figure 4.3-3 shows evolution of phases during ageing for 8h as a function of ageing temperature. It can be found that in general the intensity of the TiO_2 and α-Ti peaks increased with the ageing temperature. As the titanium was heated at an increasing temperature, an increased amount of α-Ti was precipitated from β-Ti. This left an increased weight percentage of molybdenum within the β-Ti matrix since Mo is a beta stabiliser. This lowers the d-spacing in the unit cell of β-Ti which caused an increased shift towards a higher angle, as evidenced particularly by the 57.58◦ peak (Fig. 4.3-3). It is also evident on a close up of the beta peak at 39.68, however due to this being at a lower angle, the shift is less noticeable due to the Sin θ scale.

When comparing an aged sample (STA500_8) to the solution treated sample, it can be seen that the shift of the alpha peaks has increased further (Fig. 4.3-4). The shift seen in the alpha titanium peaks is primarily due to oxygen diffused into hexagonal interstices which causes the hexagonal unit cell expansion.

Fig. 4.3-5 shows XRD patterns of sample STA500_8(2) (from which the surface oxide layer was removed by polishing), compared to AR and STA500_8 XRD patterns. It can be seen that with the removal of the oxide layer, peaks for TiO_2 disappeared but the left shift of the α-Ti peaks remains, indicating that oxygen is present as solid solution within the diffusion layer.

4.3.1.2 Chemical composition

4.3.1.2.1 Energy Dispersive X-ray (EDX) spectroscopy

EDX line-scans were carried out to examine the dark features seen in the oxidation diffusion zone of the aged samples. It was found that the darker areas contained significantly less iron and molybdenum and slightly more titanium than the grey areas (Fig 4.3-6). This confirms that these are alpha phase as molybdenum is a beta stabiliser.

EDX was also used to examine the levels of oxygen in the surface of the samples. A higher temperature of oxidation is known to cause greater amounts of surface rutile TiO_2 to form (Rastkar and Bell, 2005). This was the trend seen from STA500_8, STA550_8 and STA600_8 and links in with the thicker oxide layer measured from SEM images.

4.3.1.2.2 Glow Discharge Spectroscopy

The element concentration depth profile for sample STA500_8 was very similar to that of ST0.5 (Fig. 4.3-7a). However, due to spallation of the porous surface oxide layer on samples STA550 and STA600, the GDS graphs for these are unlike that of ST0.5 (Figs 4.3-7b&c). There is no suggestion of an alumina layer. However, a high titanium and oxygen content is still observed although they are reduced sharply in the first micron depth. This indicates that these two high temperature aging treatments are not suitable as the bonding of the oxide layer to the substrate simply becomes too poor to be at all effective for tribological usage. This was also observed from SEM images.

4.3.1.3 Mechanical testing

4.3.1.3.1 Micro-hardness

Cross-section mounted STA samples were tested under a Vickers micro-hardness indentation at 100g load (Fig. 4.3-8). Indents started at 25μm from the surface, moving into the bulk of the sample. If they were short of this, the metal deformed outwards into the Bakelite and gave an inaccurate hardness value. The micro-hardness depth profiles of the aged samples showed that STA600_8 had a higher initial hardness at 25μm depth, but this decreased sharply, as did that of STA550_8, whilst STA500_8 kept at this higher level for the entirety of the oxygen diffusion zone. Large hardness value error bars evident for the STA600_8 sample indicate non-homogeneous hardness. This could be caused by over-aging and the coarsening of α-Ti precipitates.

4.3.1.3.2 Load bearing capacity

Load was applied from 10 to 1000g and the measured hardness values decreased with increasing the load used (Fig. 4.3-9). When the applied load was 10g, the hardness of STA600_8 was lower than both STA550_8 and STA500_8. This was because even though the hardness of surface oxide layer was much higher than that of the oxygen diffusion hardened case, the adhesion of the oxide layer formed on STA600_8 was very poor and easily delaminated. The measured hardness is a composite value of the surface oxide layer and the beneath ODZ. When the applied loads exceeded 50g, more effect came from the ODZ and therefore, it was seen that samples aged at a higher the temperature had a slightly better hardness.

SEM observation of the micro-hardness indents on the surface revealed differences in the resistance to cracking of the treated surfaces from the different samples. The applied load

at which cracking appeared around the indent is plotted in Fig. 4.3-10 for four samples. It can be seen that ST0.5 sample does not show any cracking up to the maximum applicable load of 1kg with the equipment available. With the additional aging heat treatment, the rutile layer becomes weaker. However, STA500_8 still withstands a reasonable load, cracking at 300g; whereas, STA600_8 sample cracks under just 75 g.

Instead of the cracks being initiated by the four edges of the cubic pyramid indenter and spreading out from there as is usually the case (radial cracks), circular cracks formed around the indents (Fig. 4.3-11) for STA500_8. These are termed 'nesting' cracks or circular 'ring' cracks (Buckley & Miyoshi, 1984). They are formed when there is a significant difference in hardness between an oxide layer and the substrate underneath. The oxide layer is forced to collapse in around the indent, resulting in the circular cracking.

Significant spallation of surface oxide layers occurred to STA550_8 and STA600_8 samples around the indents. Clearly, although the ODZ is hard and thick, the surface oxide layers were no longer adherent to the subsurface. Therefore, it is expected that such oxide layers could not provide reasonable wear protection to the substrate because of their poor bonding to the subsurface.

4.3.2 Aging time effect on surface layer structure and properties

From the above sections it can be seen that 500°C is the optimal aging temperature. The higher temperatures produced poor quality oxide layers in term of brittleness and low adherence to the substrate, which cannot create a positive effect. Therefore, more detailed research was conducted to identify the optimal ageing time at 500 °C.

4.3.2.1 Oxide layer thickness

SEM images of the samples aged for 4, 8, 16 & 32 hours at 500 °C show that they exhibit ODZs of similar thicknesses through the different aging times (Fig.4.3-14). Measurements from the high magnification SEM images (Fig. 4.3-15) demonstrated that with a longer aging time of 32 hours compared to 8 hours, the rutile layer thickness increased from 1.8μm to 2.6μm and the thickness of the ODZ increased from ~ 65μm to an average of 75μm (Fig. 4.3-16).

4.3.2.2 Hardness and load bearing capacity

The cross-sectional hardness of the samples was similar although STA500_32 was markedly lower than the others (Fig. 4.3-17). The hardness was higher throughout the ODZ due to the higher oxygen content within the layer. This then decreased slightly to a substrate hardness of around 500$Hv_{0.1}$. The low hardness of STA500_32 within the surface case might have been caused by the growth of the α-plate during long time aging and thus the loss of precipitation hardening.

As was seen with samples comparing aging temperature, the apparent surface hardness of the samples decreased with an increasing applied load (Fig. 4.3-18).

The critical load, that at which cracking appeared around the indents, decreased as the aging time increased (Fig. 4.3-19). This gives a quantitative representation of the quality of the oxide film; a higher load of crack initiation being the preferred outcome of the treatment conditions. The sample that performed best in this test was STA500_4, cracking at 300g. However, STA500_32 sample cracked under just 100g a substantial amount, indicating cracking may have happened between 50g and 100g had that load been available. SEM observation revealed that the cracking occurred via a circular-ring mechanism, as

seen previously (Figs. 4.3-11 to 13).

4.3.2.3 Adhesion of surface oxide layers

Scratch testing of the aged samples was carried out from a starting load of 1 N to 40 N. On the shorter aging time samples that the pin ran along the surface at first without breaking the oxide layer (Fig. 4.3-20 a & b). With STA500_4 and STA500_16, the pin then broke the oxide film but did not immediately form a track into the ODZ (see areas marked 'A' in Fig. 4.3-20a and Fig 4.3-21a). This delamination of the oxide layer demonstrates the mechanisms of failure; loss of adhesion between the oxide layer and the ODZ (Berg *et al*., 1997). With all samples the pin caused increasingly extensive spallation of the oxide film formed when the load was increased (Figs. 4.3-20 & 21).

Digital data of friction force and first derivation of the friction force collected from the testing process allows a comparison of which sample performed best under dynamic loading (Fig. 4.3-22). In scratch testing, data is analysed by looking at two critical loads; L_{C1} and L_{C2}. L_{C1} is where the line that indicates the interactions between the surface and scratch tool (the first derivative) changes from relatively smooth to a large fluctuation. L_{C2} is where the line indicating friction rises sharply upwards. It can be seen from the graphs that the first big deviation (L_{C1}) is at 22, 13, 10 and 14 N for STA500_4, 8, 16 and 32 respectively, suggesting that spallation occurs when the oxide film exceeds a certain thickness (which is reached between 4 and 8 hrs of treatment). The friction trends are similar for the three samples below 30 N load but after this point, the STA500_4 sample particularly, shows a large $L_{C2.}$

4.3.2.4 Microstructure of the oxide layers

GDS profiles for all four aging times showed similar results to the ST0.5 and STA500_8 sample profiles shown in Figure. 4.2-6 & 4.3-7a. The size of the aluminium peak and the titanium trough at around 0.35μm depth increased slightly from 4 hours of aging to 8 hours but then stayed the same for up to 32 hours of treatment. This suggests that it may be possible to force higher amounts of aluminium into the oxide layer when samples are heated for longer but that there is a maximum amount that can be formed.

From XRD examination, it was seen that, with longer treatment times, a greater shift to higher angles of two-theta of the beta titanium peaks occurs and an increase in the amount of alpha titanium is seen (4.3-23). The intensity increase in alpha peaks is caused by the greater dissolution of oxygen (a strong alpha stabiliser) into the sample surface, thus causing the change from beta to alpha titanium in the oxygen diffusion zone. No aluminium peak was found from XRD.

XTEM observation and SAD pattern analysis of the oxidised layer on sample STA500_8 found that the surface oxide layer consisted of equiaxed grains of TiO_2 and Al_2O_3 in the size of 100-200 nm and 20-30 nm, respectively (Fig. 4.3-24). As can be seen from Fig. 4.3-24, Al_2O_3 particles are distributed in two areas: 250 nm beneath the surface and at the bottom of the TiO_2 layer. Two kinds of Al_2O_3 were identified: α-Al_2O_3 (JCPDS reference no. 42-1468) and β-Al_2O_3 (JCPDS reference no. 10-0414) (Fig 4.3-25). It was also found that an interface layer between the TiO_2 + Al_2O_3 and the ODZ was formed in columnar structure, which revealed to be a Ti_3O_5 oxide by SAD pattern analysis (JCPDS reference no. 23-0606). No oxides were found in the diffusion zone and oxygen was dissolved in both α-Ti and β-Ti (Fig.4.3-26).

4.3.2.5 Surface roughness

One important factor affecting the tribological characteristics of a material or coating is the surface roughness. The sizes of the asperities are often what affect the magnitude of wear. 3D images and 2D profiles were used to determine the surface of AR, ST0.5 and STA500_4 (Fig. 4.3-27). Surface roughness (Ra) values were taken from horizontal, vertical and diagonal measurements and averages calculated. The as-received material was found to have a surface roughness of 0.13µm. This increased slightly to 0.16 µm after 0.5 hrs solution treatment and slightly more to 0.21 µm after 4 hrs aging at 500 °C. It was found that a longer aging time did not increase the surface roughness further than this (Fig. 4.3-28).

4.4 Tribological assessment

Wear testing was carried out on samples AR and ST0.5 and those with different aging times (STA500_4, 8, 16 & 32). The technique of wear testing was a reciprocating ball-on-disc method. The two counterparts used were made of tungsten carbide and another of hardened steel (SAE52100). Wear tracks were made and analysed at 1 N, 5 N, 10 N and 20 N normal load at a 10mm sliding distance. Wear resistance was tested both in air and under engine oil lubrication conditions (Table 3).

4.4.1 Tungsten carbide ball as counterpart

4.4.1.1 Under dry conditions

Figures 4.4-1, 2 & 3 show the 2D profiles of the wear tracks at the different loads on samples AR, ST0.5 and aged samples. The original TIMETAL LCB material wore significantly under even the lowest load of 1 N, which for ST0.5 and aged samples hardly

marked the surface. The aged samples did however show wear tracks under heavier loads and the longer aging times (16 and 32 hrs) generally showed wider tracks than the shorter (4 and 8 hrs). The wear tracks for STA500_4 have sloping sides and a curve is formed (Fig. 4.4-2a); however, wear tracks for STA500_16 under 10 and 20 N have abrupt, steep sides that step down an immediate 2µm into the track. This implies that spallation of the surface oxide layers may have occurred during the wear process due to the tangential friction force and poor bonding strength. Different mechanisms of wear were suggested by the shape of the profiles and further discussion over the wear mechanisms will be given in the following chapter.

3D imaging of the profiles shows further detail of wear tracks on the surface of the samples (Fig. 4.4-4). The 2D profiles were seen to be true representations of the overall surface. Surface roughness values taken from a cross section of the wear track showed that the track roughness was far greater on the as-received sample than on the treated samples. This is due to greater depth difference from the track on the AR sample than the track on the treated sample. The Ra for the AR track was 5.73 µm and for the STA500_4 was 0.43µm.

The wear loss of each track was calculated and, along with the maximum friction coefficient from each test, plotted on a graph (Fig. 4.4-5a). Due to the extent of wear loss from the 'as-received' sample, a second graph was made excluding this data so that comparison between the treated samples could be better observed (Fig 4.4-5b). It can be seen that the untreated sample underwent significantly more wear loss than the treated samples. Wear loss values from the untreated sample of 0.5, 2.46, 4.98 and 7.92 (x10 mm^{-3} mm^2), for 1, 5, 10 and 20 N respectively, compare to 0.05, 0.10, 0.28 and 0.48 (x10 mm^{-3} mm^2) for sample STA500_4. All aged samples showed low wear loss compared to the

untreated sample but wear resistance of the aged samples decreased slightly with increased length of aging time. Respective values to compare sample STA500_32 to the given STA500_4 values above are; 0.08, 0.14, 0.93 and 1.04 (x10 mm^{-3} mm^{2}).

From the stated values, it can be seen that an increased load leads to an increased loss of material. The pattern of this increased differed between samples. ST0.5 and STA500_8 both showed very low wear loss at 1 N but then dramatically increased loss at the other three loads, with ST0.5 showing an abnormally large loss under a 5 N load. STA500_4 and STA500_16 however, follow a fairly consistent increase with each step up in load. STA500_32 showed similar wear loss values for 1 and 5 N and then increased but similar again for 10 and 20 N.

The maximum friction coefficients followed similar trends to wear loss figures; they were higher for sample AR than treated samples and they were generally higher for greater loads on each sample. However, there was not a significant trend of increasing or decreasing frictions coefficients between each of the treated samples.

SEM observation further demonstrated the extent of the improvement in wear resistance. As can be seen in Figs. 4.4-6a & 4.4-7, a 1 N load caused substantial material loss and a severe track on the AR sample but hardly a mark on STA500_8. Under heavier loads, the wear of the ‘as-received’ metal was very severe, causing a deep groove and typical adhesive wear features in the wear track (Fig. 4.4-6b). Also under these heavier loads, the outer oxide layer was partially removed on the treated samples (Fig. 4.4-8) but no further wear grooves could be found. This is evidenced by the continuous machining marks across the wear tracks. Wear on the STA500_4 sample (Fig. 4.4-8a) showed that less of the oxide layer was removed compared to that of STA500_32 (Fig. 4.4-8b).

Fig. 4.4-9 shows part of the wear track from AR under a 10 N load, pictured with an EDX line-scan. The green line indicates that transfer of the counterpart material (tungsten) occurred onto the titanium surface and was pushed to the outside of the wear track.

Line-scans across the wear track of a 10 N load on STA500_8 show the removed areas of outer oxides layer (Fig. 4.4-10). This is confirmed by the element graphs whereby oxygen percentage is decreased in this area and the alloy elements increased.

As seen from the 2D profile graph (Fig 4.4-2a), a 5 N load on the STA500_4 did not break the oxide layer. This is seen in the SEM image (Fig 4.4-11) and also the EDX element percentage spectra accompanying it. The tungsten carbide ball pushed the oxides film to the sides of the wear track but not enough stress had built up at the low load to cause spallation. This is confirmed from the table of spectrum compositions since all three have very similar values for both oxygen and titanium weight percentages. In EDX analysis of spalled areas of oxide film, the oxygen percentage is much lower and the titanium percentage much higher in the spalled area than on the oxide film.

In contrast to STA500_4, the oxide layer of STA500_16 did spall under a 5 N load. However, this was mainly the case at the outer edges of the wear track (Fig. 4.4-12). EDX spectrum analysis confirms that in the centre of the wear track most of the oxide film was not removed (Spectrum 1). As with STA500_4, material from the oxide film could have first been moved outwards with the low load rather than immediate brittle fracture. This would have caused stress concentrations to build up here, resulting in this area of oxide being torn away.

Wear debris was carefully tipped onto a carbon tab in order to be studied under the SEM and analysed using EDX (Fig. 4.4-13). The debris was mostly made up of brittle chunks of

the oxides ranging from around 10 to 150μm in diameter. Only a very small percentage of the debris was found to be tungsten.

Examination of the tungsten carbide ball, after pin-on disc testing of STA500_16 at 20N for 500 cycles using EDX, revealed that transfer of titanium had occurred. Mapping illustrates the location of the titanium (Fig. 4.4-14) whilst the spectrum data shows the amount of transfer in weight and atomic percentage values.

4.4.1.2 Under oil lubricated conditions

A tungsten ball counterpart under a load of 20 N was tested on sample STA500_16 in a lubricated environment and the results compared to those of the dry condition (Fig. 4.4-15). As can be seen from the graph with the dry environment however, only a patch of the outer oxide layer was removed, while under oil lubrication wear loss was increased with a wider wear track formed. Therefore, matching with scientific theory, lubrication was ineffective in stopping wear loss occurring. It may be that oil penetrates into the interface between the outer oxide layer and the inner oxide layer through the defects in the outer oxide layer; the high oil pressure in contact area would peel the outer oxide layer off from the sample surface, the inner oxide layer remained intact and prevented deep wear loss occurring into the ODZ.

4.4.2 Hardened steel balls as counterpart

4.4.2.1 Under dry conditions

Wear tests using a hardened steel ball as the counter-part material produced remarkably different results for all treated samples. The balls were of the same diameter but the wear tracks were far wider when using the hardened steel balls. Figure 4.4-16 shows wear tracks

for loads of 1, 5, 10 and 20 N on STA500_16 samples. Even under a low load, the track is wider and the outer oxide layer is removed completely in contrast to the patchy appearance of tracks caused by a tungsten carbide ball (Fig. 4.4-8).

Observation of the ball after each wear test showed a flattened area, where material had been worn away and hence increased the contact area between sample and ball as the test proceeded. Under microscopic observation of the steel ball after wear testing with a 20 N load, the circular flattened areas were measured to be an average of 0.81mm in diameter and almost perfect circles. A schematic of the area in Figure 4.4-17 gives dimensions. Hardness values taken from the hardened steel ball were then compared to hardness values taken from the tungsten carbide ball (Fig. 4.4-18). The tungsten carbide ball was found to be almost twice as hard as the hardened steel ball.

When using hardened steel as the counter-part material, it was seen that a far deeper track was worn in the ‘as-received’ sample by a load of only 1 N (Fig. 4.4-19a) compared to the same test using a tungsten carbide ball (Fig. 4.4-1a). As noted from the SEM images, the wear track profiles on the treated samples were wide and shallow (Figs. 4.4-19b, 20 & 21). A load of 1 N had no effect on STA500_4 and STA500_8 but apart from these, all aged samples had wear tracks of the same depth and varying widths. The standard depth was around 2μm (see Fig. 4.4-22). Clearly, the outer oxide layer was removed but the inner oxide layer underneath was not worn away and therefore acted as the wear resistant layer supported by the ODZ beneath.

From the 3D image of the 20 N wear track profile on STA500_16, the flat-base can be seen in more detail (Fig. 4.4-22) and shows that the 2D profiles were representative of the wear track shape.

The wear loss values calculated from the 2D profiles and maximum friction coefficient data retrieved direct from the wear test machine is given in figure 4.4-23. As seen previously, the treated samples experienced far less material loss in wear testing than the untreated material in almost all test comparisons. However, under a 1 N load, samples STA500_16 and STA500_32 obtained a greater wear loss than sample AR. This was due to the delamination of the brittle outer oxide layer caused by the longer aging times and the wide track caused by the wear of the steel ball. The amount of wear loss was similar between the aged samples. Sample STA500_8 showed the best wear resistance under 5, 10 and 20 N compared to samples aged for 4, 16 or 32 hours. The longer aging times of 16 and 32 hours resulted in greater wear loss than the samples aged for 4 and 8 hours. There was a general trend of increasing wear loss with an increasing applied load. However, sample STA500_8 had an almost identical wear loss at 5, 10 and 20 N. Wear loss values are increased compared to the wear tests undertook with a tungsten carbide counterpart. This is due to wear of the steel counterpart creating a greater contact surface area between the reciprocating surfaces.

As seen from inspection of the hardened steel ball, much of its surface wore away during testing. EDX examination of a wear track on STA500_16 from a 10 N load (Fig. 4.4-24) shows that ball material was transferred to the wear surface since a highly increased amount of iron is present as well as a small amount of chromium.

4.4.2.2 Under oil lubrication conditions

After wear tests under 10 and 20 N loads, visual inspection on the wear tracks with oil found that they were almost identical to those wear tracks without oil. However, under SEM observation, the tracks showed marked differences. Where the steel balls in the dry environment had removed the oxide layer, there was also evidence of transferred ball material to the wear surface (Fig 4.4-25b). However, when oil was used in the test environment, these marks were no longer present, apart from the removed oxide layer (Fig.4.4-25a).

Examination of a 10 N wear track on STA500_8 from a hardened steel ball with oil was carried out using EDX (Fig. 4.4-26). No chromium was picked up and there was no increase in iron percentage in the wear track. This revealed that when oil lubrication was used, there was not the adhesion of the counterpart material (hardened steel) onto the wear track as had been seen when lubrication was not present.

All samples are compared against each other under a 20 N load in Figure 4.4-27. The treated samples gave very similar results to each other, while the AR sample again wore greatly. The widest track was seen from STA500_4 which may have been caused by the thinner oxide film that this sample possessed.

STA500_4 had undergone the least amount of wear loss from the tungsten carbide ball tests so this sample was tested under all four loads with the steel + oil condition. All loads caused a removal of the outer oxide film, shown by the depth profile, with the width of track increasing with the increased load (Fig. 4.4-28).

The wide, sharp drop, wear track profile can be seen in more detail from the 3D image

given in Fig. 4.4-29 of a 20N wear track on STA500_32. The surface of the wear track is smoother than when oil was not used (Fig. 4.4-22) which reflects what was seen under SEM observation. The average surface roughness taken from a cross section of the wear track was 0.89 µm compared to 1.16 µm when oil was not used.

As in the dry environment, the hardened steel ball showed signs of adhesive wear loss by gaining a circular flat surface after each wear test. In the oil lubricated tests, three-body abrasion of the steel was the cause of wear to the ball.

4.4.3 Comparison of wear tests

Comparison of all conditions was done using the results of wear tests on sample STA500_16 with a 20 N load (Fig. 4.4-30). All wear tracks possessed similar maximum depths, showing that only the outer oxides layer was removed in a tribological situation. Wear loss of the outer oxide layer was greater under a steel counterpart due to the severe wear of the steel ball contact surface. No wear scar could be seen on the tungsten ball after lubricated testing which suggested that oil surface tension and the pressure of oil in the cracks of the oxide layer was also the cause of complete outer oxide layer removal in the path of the reciprocating counterpart.

CHAPTER V

INTERPRETATION & DISCUSSION

5.1 Evolution of Treated Surface Cases

5.1.1 Formation of surface oxide layers

From analysis of the treated samples using various techniques, a comprehensive picture of the layer structure was gained. SEM observation showed a white oxide layer on top of the underlying oxygen diffusion zone (ODZ). For example, an oxide layer of 2.3 μm in thickness was formed on the ODZ for STA500_8 sample (Fig. 4.3-1a). XRD analysis revealed that this oxide layer was TiO_2 rutile.

However, GDS composition-depth profiles exhibited two peaks of aluminium: one at approximately 0.3μm below the surface and the other near the oxide/substrate interface (Fig. 4.2-6). This is in agreement with Rastkar and Bell (2005) who found that a protective outer layer of alpha-Al_2O_3 was not formed on air-oxidised titanium; instead, an alumina rich intermediate layer formed near the topmost surface layer.

XTEM examination revealed a far more complex layered oxide structure: a TiO_2 dominated outer oxide layer and an inner Ti_3O_5 oxide layer. Two thin white strips were found within the surface oxide layers: one is close to the surface and the other is at the interface between outer TiO_2 oxide layer and inner Ti_3O_5 oxide layer. The electron diffraction patterns from these white strips were then interpreted as being alumina. This is in good agreement with the GDS analysis results which showed the pile up of aluminium close to the surface and at the TiO_2/Ti_3O_5 interface. This also implies that the amount of alumina in the treated surface is below the detection limit of the θ/ 2θ Bragg-Brentano

geometry XRD method.

This multi-layered oxide structure has also been reported by Du et al., (1996) in oxidised Ti6Al4V alloy. When the alloy was oxidised in a $H_2/H_2O/H_2S$ environment, researchers found that 'some Al_2O_3 precipitated in the external portion of the outer TiO_2 layer. When the alloy was oxidised in air, a 'multilayered oxide scale' formed with 'alternating layers of Al_2O_3/ TiO_2'.

The formation of such multi-layered structure consisting of alternating layers of Al_2O_3/ TiO_2 could be explained by the two competing reactions during the combined treatment of thermal oxidation and STA: (i) oxidation of titanium to form titanium oxide and (ii) oxidation of aluminium to form alumina.

It is known that both titanium and aluminium have a strong affinity to oxygen but the Gibbs energy change is more negative for reaction (ii) than for reaction (i). Hence, alumina is a more favourable oxide to form than titanium oxide from a thermodynamics point-of-view (Gaskell, 1981). However, aluminium only holds a 1.5 wt% in TIMETAL LCB compared to titanium's share of 87.2 wt%. Therefore, titanium has a much higher activity than does aluminium in TIMETAL LCB. Clearly, titanium oxides (such as Ti3O5 or TiO2) would preferentially form when the TIMETAL LCB alloy is treated in air. In view of the relatively low treatment temperature and diffusion features of oxygen and aluminium/titanium, it is reasonable to believe that oxygen inward diffusion dominates the oxidation process of TIMETAL LCB.

Because these oxides can only contain a very small amount of aluminium within it, aluminium will be driven out of the oxide layer, thus leading to accumulation of aluminium at the oxide/substrate interface. The locally increased aluminium activity will favour the

formation of alumina below the top titanium oxide layer. Further inward diffusion of oxygen will promote the formation of titanium oxide layer. This explains the formation of alternating titanium oxide layer and aluminium oxide layer.

5.1.2 Microstructure and bonding

According to the results reported in Chapter IV, the treated surface of TIMETAL LCB can be divided into three parts: (1) outer oxide layers, (2) inner oxide layer and (3) oxygen diffusion zone (ODZ).

When oxygen diffuses into the substrate, an oxygen diffusion zone (ODZ) will form first when the oxygen content is below its solid solubility in titanium. This will result in significant solid solution hardening. This hardening effect arises from oxygen atoms being contained within the titanium interstitial sites and may be either caused by direct interaction with solute atoms and dislocations (Gleiter, 1983). It is known that the solid solubility of oxygen is larger in beta phase than in alpha phase. Hence, a thick ODZ can be easily formed in beta alloys than in alpha alloys. According the nature of the ODZ, there should be no spallation problem associated with the ODZ.

On the top of the ODZ is a thin (0.5-1.0 microns) inner Ti_3O_5 oxide layer. As evidenced in Figure 4.3-24, the inner oxide layer has a similar microstructure and density to that of the ODZ, and therefore good bonding to the ODZ underneath is expected. This has been supported by the fact that although the top oxide layer was removed when rubbing against a WC or hardened steel ball during sliding wear tests, the inner oxide layer provided the wear resistance that prevented wear tracks from being more than 2 μm in depth (Figs. 4.4-19, 20 & 21). Hence, the inner oxide layer is of most importance since it is this inner oxide

layer that provides tribological protection to the alloy.

In the present work, it has been observed that the top oxide layers can be removed during wear (Figs. 4.4-8 & 4.4-16) and scratch tests (Figs. 4.3-20 & 4.3-21), especially for the high-temperature and/or long-time treated samples. This can be attributed to the high value of the Pilling-Bedworth ratio (PRB) between rutile and Ti (PBR= 1.75) (Bertrand et al., 1983). As a consequence of a high compressive stress in the oxide, high tensile stress in Ti may develop at the interface. In addition, the presence of Al_2O_3 may have also contributed to outer oxide layer spallation. This is because of the large difference in hardness, modulus and thermal expansion coefficient between titanium oxide and alumina, which contribute to interfacial stresses during cooling after thermal treatment and loading.

5.2 The mechanisms of wear

Different variables were used for wear testing and with these changes differing wear mechanisms were observed. The wear resistance was seen to greatly improve from untreated to treated material. The wear mechanisms are also affected by the test conditions such as counterpart materials and lubrication.

5.2.1 Dry sliding against WC balls

Typical adhesive wear features, such as adhesive craters and deep ploughing grooves, were seen from wear tracks on as-received material (Fig. 4.4-6b). This strong adhesive wear tendency is related to the nature of titanium in terms of electron configuration and crystal structure (See Section 2.3). The removed titanium then became work-hardened under the repeated sliding, resulting in abrasive wear damage on the titanium surface (Dong & Bell, 2000).

By contrast, the wear morphologies of the treated surfaces differ greatly from that of the above untreated material. As shown in 4.4-7, when tested under a light load of 1N, very little (if any) wear was observed as evidenced by the persistence of original machining marks. When the applied load increased to 5N, mild abrasive wear was observed (Fig. 4.4-11) for all STA treated samples. The mechanism in place here was abrasive wear. This occurred from the sliding motion between the sample surface and the ball which caused mechanical interaction of asperities and breaking of these junctions to form removal of the oxide layer and thus wear particles. These wear particles were then catalysts for three-body abrasive wear (Qu et al.,2005). A diagrammatic explanation of this mechanism is given in Figure 5.2-1 which shows the tungsten carbide ball under loading sliding across the oxide layer (a) which causes break-off of asperities (b) and therefore three-body abrasion wear of the outer oxide layer (c).

When further increasing the applied load, partial spallation of the surface oxide layer occurred. Wear and friction were significantly increased, especially under 20 N (Fig. 4.4-8b). This spallation was caused by increased tangential friction force proportional to the applied load. The above mechanism is supported by that fact that, the wear of the STA treated samples increased with the aging time when tested under 10 and 20N (Figure 4.4-5). This is because the scratch tests had revealed that the bonding of the outer surface oxide layer decreases beyond a certain aging time.

5.2.2 Dry sliding against steel balls

It is of great interest to note that the wear of the STA treated samples increased rather than decreased as expected when the hard WC balls were replaced by relatively soft hardened steel balls (Fig. 4.4-23 vs Fig. 4.4-5). Clearly, this cannot be explained from an abrasive

wear point-of-view because abrasive wear mainly depends on the hardness difference between the sample surface and the sliding ball.

Therefore, with this change in counterpart material, an entirely different wear mechanism took place; that of fatigue or delamination wear. Fatigue wear of a material is caused by cyclic loading during friction. Microcracks form at or below the surface, which then spread and cause wear particles to delaminate.

In this process, the surfaces in contact are very different in their hardness, causing wear loss to occur from the hardened steel ball counterpart firstly. This resulted in a large contact area between the articulating surfaces and hence large frictional forces. Therefore, a high level of shear stress will generate at the oxide/substrate interface. Due to the bonding strength of the outer oxides layer being low, as seen from scratch testing, microcracks would have been initiated within the rutile layer. These cracks would then spread along the interface between the outer rutile layer and inner layer of Ti_3O_5 as a result of repeated stress by the steel ball. Eventually the outer rutile oxide layer delaminated from the surface (Fig. 4.4-24).

This new rougher surface increased the rate of the wear on the ball and widened the wear tracks. This wear of the ball was caused by abrasion from spalled rutile particles. Material transfer then occurred from the steel counterpart to the wear track it was creating (Fig. 4.4-24). However, wear seemed to stop at the interface probably due to the strong and adherent inner oxide layer of Ti_3O_5.

5.2.3 Effect of lubrication

The effect of lubrication on the wear of untreated and surface engineered samples sliding against WC and steel balls was investigated. It was surprising to find that wear of STA treated LCB samples increased by oil lubrication (Fig.4.4-30). The wear tracks were wider than in a dry environment but there was however no adhesion of the removed steel ball material within the wear tracks (Fig. 4.4-24) as had been seen without oil (Fig. 4.4-25). The increased wear could be attributed to the penetration of high-pressure oil within the contact area into the oxide layer, which sped up the delamination of the outer oxide layer.

The proposed mechanism is schematically shown in Figure 5.2-2 using steel balls as example. When a hardened steel ball is sliding across the oxide layer in an oil lubricated environment (Fig5.2-2a); the steel ball firstly undergoes wear which widens the contact area between the two articulating surfaces and forces oil downwards into the microcracks of the outer oxide layer, and repeated stress and high oil pressure causes growth of cracks at the interface (Fig5.2-2b); and finally sections of the outer oxide layer to be delaminated and severe wear loss from the hardened steel ball causes wide track to be formed (Fig5.2-2c). However, wear does not proceed into the inner oxide layer and ODZ (both are included in the darker grey area on the diagrams). This is supported by the observation that the wear tracks have almost vertical sides and the depth of the wear track formed in the STA treated surfaces is the same as the thickness of the outer oxide layers on these samples (Figs. 4.4-27, 28 and 30).

The mechanism involved in the wear pair of WC ball/titanium surface under oil lubricated conditions is similar. The only difference lies in the width of the wear tracks. Because the steel ball is not as hard as the WC ball (Fig. 4.4-18), more severe abrasive wear occurs to

the steel ball than to the WC ball. Therefore, the contact area is larger under a steel ball than under a WC ball. This may not only cause larger shear stress at the interface but also increase the probability of penetration of oil into the oxide layers.

5.3 Optimum treatment parameters

A new surface engineering technique has been developed by combining bulk STA heat treatment with thermal oxidation. This is driven by the fact that the standard thermal oxidation process developed by Dong et al. (2000) involves long-time (50-100h) oxidation at 600-650 °C, which would cause undue growth of grains and lose core strength for such beta alloy as LCB.

The temperature for solution treatment (850 °C) was chosen due to it being around 40 °C below the beta-transus, which is the suggested temperature in the literature (Williams & Starke, 1984 and Kosaka et al., 2005). Two heating periods, 0.5 and 6 hours, have been investigated in the present work. The results have shown that a short heating time of 0.5 hours is better than a long heating time of 6 hours from both bulk microstructure and surface quality viewpoints. This is because although both heating times can produce a microstructure with full β phase grains (Fig. 4.2-2), severe surface damage was observed for the ST6 samples (Fig. 4.2-1).

It has been found from the literature that aging below 500 °C is not sufficient to allow enough alpha precipitates to form in the beta matrix, thus lowering the strength of the bulk material (Donachie, 2000). Therefore, three temperatures, 500, 550 and 600 °C, have been studied to identify the optimal ageing parameters. Although the thickness of surface oxide layer and oxygen diffusion zone increase with increasing ageing temperature, ageing at 550

and 600 °C produced oxide layer with high brittleness and low adherence (Figs. 4.3-12 & 13). Therefore, the optimal aging temperature for the combined treatment is 500°C, which produced the highest critical load (Fig. 4.3-10).

The optimal aging time for the combined treatment has also been identified based on systematic characterisation of the microstructure, evaluation of scratching and wear tests and assessment of the bulk hardness. As has been reported in Chapter 4, although long-time (16 & 32 hours) aging can produce a relatively thick oxide layer and ODZ (Fig. 4.3-16), the bonding strength of the surface oxide layer reduces with increasing aging time (Fig. 4.3-19). Moreover, wear test results also demonstrate that the long-time (16 & 32 hours) aged samples possess a lower wear resistance than the short-time (4 & 8 hours) aged samples.

Aging for 8 hours gave a sufficiently thick oxide layer and a hardness-depth profile that was better than that of sample STA500_4 (Fig. 4.3-17). The STA500_8 samples also performed well under wear testing especially when sliding against steel balls (Fig. 4.4-23).

As has been shown in Figure 4.3-17, the hardness of the STA500 samples is very close to that of the untreated materials. Therefore, it can be deduced that the combined treatment would not negatively affect the mechanical properties of the substrate.

It thus follows that the best parameters for the combined treatment of TIMETAL LCB are solution treatment for 0.5 hours at 850 °C with post-treatment quenching into water, followed by aging at 500 °C for 8 hours. These treatment parameters can ensure that the strength of the bulk material will be retained and the surface wear resistance can be significantly increased, hence satisfying the aims of this research project.

CHAPTER VI

CONCLUSIONS AND RECOMMENDATIONS FOR FUTURE WORK

1. A novel surface engineering process for low-cost beta titanium alloy, TIMETAL LCB (Ti-6.8Mo-4.5Fe-1.5Al), has been developed by combining bulk solution and aging treatment with surface oxidation treatment.

2. Solution treatment for 0.5 hours at 850°C in air can produce a thin, dense and adherent oxide layer followed by an oxygen diffusion hardened zone on top of the substrate with a hardness of 400Hv0.1.

3. For a given aging time of 8 hours, although the thickness of surface oxide layer and oxygen diffusion zone increase with increasing aging temperature, aging at 550 and 600°C produced brittle and poorly-adherent oxide layers; on the other hand, aging at 500°C produced a high-quality surface case with the highest load bearing capacity.

4. When aged at 500 °C, long-time (16 & 32 hours) aging can produce a relatively thick oxide layer and ODZ but the bonding strength of the surface oxide layer is much lower than that generated by short time (4 & 8 hours) aging.

5. SEM observations reveal that a typical treated surface consists of a surface oxide case followed by an oxygen diffusion zone (ODZ). The ODZ contains a high amount of alpha grains embed in the beta matrix because of the alpha stabilising effect of oxygen.

6. Detailed XRD and XTEM analyses indicate that the surface oxide case is composed of two major oxide layers: an outer rutile TiO_2 layer and an inner Ti_3O_5 layer; two Al_2O_3 rich strips are revealed by XTEM microstructure: one is close to the top of rutile layer and the other is at the TiO_2/Ti_3O_5 interface.

7. The wear resistance of TIMETAL LCB alloy can be improved by 4-16 times by the novel combined bulk/surface treatment when sliding against a hard WC-Co ball under unlubricated conditions. The coefficient of friction is reduced from 0.8-1.0 for the untreated material to 0.2-0.4 for most treated samples.

8. The wear mechanisms evolve from severe adhesive wear for the untreated material to mild abrasive wear (under low-load) and mixed abrasive/delamination wear (under high loads) for the 500°C/8h aged material when sliding against a WC-Co ball in air.

9. An improvement by 4-8 times in wear resistance of TIMETAL LCB alloy has been observed when the treated material slides against a hardened steel ball in air. Severe wear to the steel counterpart occurred and a large flat contact surface and hence large frictional forces formed. This led to delamination wear because of the large shear stress at the oxide/substrate interface.

10. Oil lubrication can prevent material adhesive transfer, but cannot reduce (and rather increases) the wear of treated surfaces especially when sliding against a hardened steel ball. This is largely because the oil at the contacting area will penetrate into the interface, thus promoting the delamination of surface oxide layer. However, there is no appreciable wear to the dense and adherent Ti_3O_5 beneath.

11. Based on the experimental results, the optimal treatment conditions for the novel combined bulk/surface treatment of TIMETAL LCB are solution treatment for 0.5 hours at 850 °C followed by aging at 500 °C for 4-8 hours.

SUGGESTED FUTURE WORK

Some very significant observations have been made in the development of novel combined bulk/surface treatment for TIMETAL LCB alloy in the present research project. However, this technology is still at its early stage and future work is needed to realise its potential:

- Fatigue tests on the treated TIMETAL LCB could be conducted to assess the effect of the combined bulk/surface treatment on its fatigue properties, which are very important for some applications.

- Comparative treatments should be carried out at less widely spaced temperature and time variables to create a more accurate database of the best parameters to use.

- Due to the findings that the Ti_3O_5 layer was the barrier to wear loss advancing beyond the outer rutile oxide layer, work should be done to investigate if it is possible to increase the thickness of this layer whilst decreasing the thickness of the TiO_2/Al_2O_3 layer.

- Because of the success of the novel combined bulk/surface in combating wear of TIMETAL LCB, the novel combined treatment should be tested on other beta titanium alloys to check its effectiveness.

REFERENCES

American Academy of Orthopaedic Surgeons. 2001 'What are the wear mechanisms and what controls them' [online] www4.aaos.org/product/implant/22chapter.pdf [Accessed on 15.06.10]

ASTM Standard G99, 2005 (2010) 'Standard Test Method for Wear Testing with a Pin-on-Disk Apparatus', ASTM International, West Conshohocken, PA, 2010, DOI: 10.1520/G0099-05R10 [www.astm.org]

Arciniegas, M, Manero, JM, Pena, J, Gil, FJ, Planell, JA. 2008 'Study of new multifunctional shape memory and low elastic modulus Ni-Free Ti alloys' Metallurgical and Materials Transactions A, vol. 39A, pp. 742-751

Berg, G, Friedrich, C, Broszeit, E, Berger, C. 1997 'Scratch test measurement of tribological hard coatings in practice' Fresenius Journal of Analytical Chemistry, vol. 358, pp. 281-285

Bloyce, A, Morton, PH, Bell, T. 2002 'Surface engineering of titanium and titanium alloys' ASM Handbook Volume 5 : Surface Engineering, 10th Edition, Materials Park, Ohio, USA, ASM International, pp. 835-851

Buckley, DH, Miyoshi, K. 1984 'Friction and wear of ceramics' Wear, vol. 100, pp. 333-353

Bull, SJ. 1997 'Failure mode maps in the thin film scratch adhesion test' Tribology International, vol. 30, no. 7, pp. 491-498

Collings, EW. 1984 'The physical metallurgy of titanium alloys' American Society for Metals, pp. 2

Destefani, JD. 1990 'Introduction to titanium and titanium alloys' ASM Handbook, vol 2, Materials Park, Ohio, USA, ASM International, pp. 586-591

Divakar, R, Blau, PJ (editors). 1992 'Wear testing of advanced materials' 10th Edition, STP 1167, West Conshohocken, Pennsylvania, ASTM publication

Diebold, U. 2003 'The surface science of titanium dioxide' Surface Science Reports, vol. 48, issues 5-8, pp. 53-229

Donachie, MJ. 2000 'Titanium: a technical guide' 2nd Edition, ASM Handbook, Materials Park, Ohio, USA, ASM International

Dong, H. May 2010 'Surface engineering of light alloys- aluminium, magnesium and titanium alloys' Cambridge, UK, Woodhead Publishing Ltd. (ISB N 978-1-84569-537-8)

Dong, H, Bell, T. 2000 'Enhanced wear resistance of titanium surfaces by a new thermal oxidation treatment' Wear, vol. 238, pp. 131-137

Dong, H, Bell, T, Mynott, A. 1999 ‘Surface engineering of titanium alloys for the motorsports industry’ Sports Engineering, vol. 2, pp. 213- 219

Dong, H, Bloyce, A, Morton, PH, Bell, T. 1996 ‘Surface engineering of titanium alloy with oxygen’ Titanium '95 - Science and technology; Proceedings of the 8th World Conference on Titanium, Birmingham, United Kingdom, pp. 1999-2006.

Dong, H, Sun Y, Bell, T. 1997 ‘Enhanced corrosion resistance of duplex coatings’ Surface and Coatings Technology’ vol. 90. pp. 91-101

Du, HL, Datta, PK, Lewis, DB, BurnellGray JS. 1996 ‘High temperature corrosion of Ti and Ti-6Al-4V alloy’ Oxidation of Metals, vol. 45, issue. 5, pp. 507-527

Eisenbarth, E, Velten, D, Schenk-Meuser, K, Linez, P, Biehl, V, Duschner, H, Breme, J, Hildebrand, H. 2002 ‘Interactions between cells and titanium surfaces’ Biomolecular Engineering, vol. 13, pp. 243-249

Feng, C, Khan, TI. 2008 ‘The effect of quenching medium on the wear behaviour of a Ti-6Al-4V alloy’ Journal of Materials Science, vol. 43, pp.788-792

Fraczek, T, Olejnik, M, Tokarz, A. 2009 ‘Evaluation of plasma nitriding efficiency of titanium alloys for medical applications’ Metalurgija, vol. 48, issue 2, pp. 83-86

Gardos, MN. 1994 ‘Determination of the tribological fundamentals of solid lubricated ceramics. Part 3: Molecular engineering of rutile (TiO2-x) as a lubricious oxide’ Report available from CASI HC A09/MF A03, #AD-A295170; WL-TR-94-4108

Gaucher, A, Zabinski, B. 1975 ‘Nouvelles Possibilities de Frottement des Alliages de Titane: Le Tifran’ Entropie, vol. 63, pp. 36-41 (in French) (information extracted from Bloyce et al., 2002–given in this list)

Guleryz, H, Cimenoglu, H. 2005 ‘Surface modification of a Ti-6Al-4V alloy by thermal oxidation’ Surface and Coatings Technology, vol. 192, pp. 164-170

Hanzel, RW. 1954 ‘Surface hardening processes for titanium and its alloys’ Metal Progress, pp. 89-96

Harper, CA, Sampson, RN. 1994 ‘Electronic materials and processes handbook’ 2nd edition, McGraw-Hill Handbooks, USA. pp. 5

Ivansishin, OM, Markovsky, PE, Matviychuk, YuV, Semiatin, SL. 2003 ‘Precipitation and recrystalisation behaviour of beta titanium alloys during continuous heat treatment’ Metallugical and Material Transactions A, vol. 34a, pp. 147-158

Ivansishin, OM, Markovsky, PE, Matviychuk, YuV, Semiatin, SL, Ward, CH, Fox, S. 2007 ‘A comparative study of the mechanical properties of high-strength β-titanium alloys’ Journal of Alloys and Compounds, vol. 457, pp. 296-309

Khan R.H.U. 2008, 'Characteristics and Stress State of Plasma Electrolytic Oxidation Coatings', PhD thesis (2008), The University of Sheffield, UK.

Kofstad, P, Hauffe, K, Kjollesdal, H. 1958 ‘Investigation on the oxidation mechanisms of titanium’, ACTA Chemica Scandinavica, vol. 12, pp. 239-266

Kosaka, Y, Fox, SP, Faller, K, Reichman, SH. 2005 ‘Properties and Processing of TIMETAL LCB’, Journal of Materials Engineering and Performance, vol. 14, pp. 792-798

Leyens, C, Peters, M. (editors) 2003 ‘Titanium and Titanium Alloys: Fundamentals and Applications’ DLR German aerospace centre, Institute of Materials Research, Koln, Germany, Wiley-VCH.

Li, SJ, Yang, R, Li, S, Hao, YL, Cui, YY, Niiomi, M, Guo, ZX. 2004 ‘Wear characteristics of Ti-Nb-Ta-Zr and Ti-6Al-4V alloys for biomedical applications’ Wear, vol. 257, pp. 869-876

Liu, YZ, Zu, XT, Wang, L, Qui, SY. 2009 ‘Role of aluminium ion implantation on microstructure, micro-hardness, and corrosion properties of titanium alloy’ Vacuum, vol. 83, pp. 444-447

Ma, H, Wang, M, Wu, W. 2004 ‘Oxygen permeation behaviours and hardening effect of titanium alloys at high temperature’ Journal of Material Science and Technology, vol. 20, issue 6, pp. 719-723

Machlin, ES, Yankee, WR. 1954 ‘Friction of clean metals and oxides with special reference to titanium’ Journal of Applied Physics, vol. 25, pp. 576-581

Molchanova, EK. 1965 ‘Phase diagrams of titanium alloys [translation of Atlas diagram sostoyaniya titanovyk spiovov], Israel Program for Scientific Translations, Jerusalem. Taken from; Collings, EW. 1994 Materials Properties Handbook, *ASM international*, page 9.

Qu, J, Blau, PJ, Watkins, TR, Cavin, OB, Kulkarni, NS. 2005 ‘Friction and wear of titanium alloys sliding against metal, polymer and ceramic counterfaces’ Wear, vol 258, pp. 1348-1356

Rastkar, AR, Bell, T. 2005 ‘Characterisation and tribological performance of oxide layers on a gamma based titanium aluminide’ Wear, vol. 258, pp.1616-1624

Schmalzreid, TP, Callaghan, JJ. 1999 ‘Current concepts review: Wear in total hip and knee replacements’, Journal of Bone and Joint Surgery. American volume, vol. 81, pp. 115-136

Sioshansi, P. 1990 ‘Improving the properties of titanium alloys by ion implantation’, Journal of Metals, pp. 30-31

Sritharan, T, Chandel, RS. 1997 ‘Phenomena in interrupted tensile tests of heat treated aluminium alloy 6061’ Acta Materials, vol. 45, pp. 3155-3161

Streicher, RM, Weber, H, Schon, R, Semlitsch, M. 1991 ‘New Surface Modification for Ti-6Al-7Nb Alloy: Oxygen Diffusion Hardening (ODH)’ Biomaterials, vol. 12, pp. 125-129

Takadoum, J, Roques-Carmes, C, 1992 ‘Influence of the oxidation activity of metals on

friction and wear of ceramic-metal systems' Surface and Coatings Technology, vol. 52, pp. 153—158

Teh T H, 2003 'Initial stages of plasma electrolytic oxidation of titanium' Corros. Sci. 45 (2003) pp2757–2768

Weiss, I, Srinivasan, R, Saqib, M, Stefansson, N, Jackson, AG, Leclair, SR. 1996 'Bulk deformation of Ti-6.8Mo-4.5Fe-1.5Al (timetal LCB) alloy' Journal of Materials Engineering and Performance, vol. 5, issue 3, pp. 335-352

Williams, JC, Starke, EA. Jr. 1984 'The role of thermomechanical processing in tailoring the properties of aluminium and titanium alloys', Deformation, Processing, and Structure, George Krauss, Ed., American Society for Metals

Wilkins group, 2006. Phase diagrams, Edited by: wilkins@mps.ohio-state.edu source: http://www.physics.ohio-state.edu/~wilkins/group/phases/index.html> [Accessed on: Tuesday, 31-Aug-2010 07:18:17 EDT]

Woydt, M, Skopp, A, Dorfel, I, Witke K. 1998 'Wear engineering oxides/ anti-wear oxides' Wear, vol. 218, pp. 84-95

Yankee, WR, Machlin, ES. 1954 'Influence of oxygen and nitrogen in solution in alpha titanium on the friction coefficient of copper on titanium', Transactions AIME, pp. 989-990

Yerokhin A L, Nie X, Leyland A and Matthews A 2000, 'Characterisation of Oxide Films Produced by Plasma Electrolytic Oxidation of a Ti–6Al–4V Alloy' Surf. and Coat. Technol. 130 (2000) pp195–206

Yerokhin A L, Snizhko L O, Gurevina N.L, Leyland A, Pilkington A., Matthews A 2003 'Discharge characterization in plasma electrolytic oxidation of aluminium', J.Phys. D: Appl. Phys. 36 (17) (2003) pp2110

TABLES

Table 1: Treatment parameters and specimen codes

Specimen code	Solution treatment time (at 850°C), hrs	Aging temperature ,°C	Aging time, hrs
ST6	6	-	-
ST0.5	0.5	-	-
STA500_8	0.5	500	8
STA550_8	0.5	550	8
STA600_8	0.5	600	8
STA500_4	0.5	500	4
STA500_8	0.5	500	8
STA500_16	0.5	500	16
STA500_32	0.5	500	32

Table 2: d-spacings and 2θ values from data base and their new values for TIMETAL LCB due to the presence of molybdenum in the matrix

No.	HKL	d (Å) – (44-1288)	d (Å) – TIMETAL LCB	2θ (°) - documented	2θ (°) – TIMETAL LCB
1	110	2.34	2.27	38.48	39.68
2	200	1.65	1.60	55.54	57.58
3	211	1.35	1.33	69.61	70.81
4	220	1.17	1.11	82.45	87.92

Table 3: Wear testing parameters

Condition		AR	ST0.5	STA500_4	STA500_8	STA500_16	STA500_32
Ball	Lubricant	Loads tested at (N)					
Tungsten Carbide	No	1, 5, 10, 20	1, 5, 10, 20	1, 5, 10, 20	1, 5, 10, 20	1, 5, 10, 20	1, 5, 10, 20
Hardened Steel	No	1, 5, 10, 20	1, 5, 10, 20	1, 5, 10, 20	1, 5, 10, 20	1, 5, 10, 20	1, 5, 10, 20
Hardened steel	Yes	10, 20	10, 20	1,5,10, 20	10, 20	10, 20	10, 20
Tungsten Carbide	Yes	x	x	x	x	10, 20	x

ILLUSTRATIONS AND FIGURES

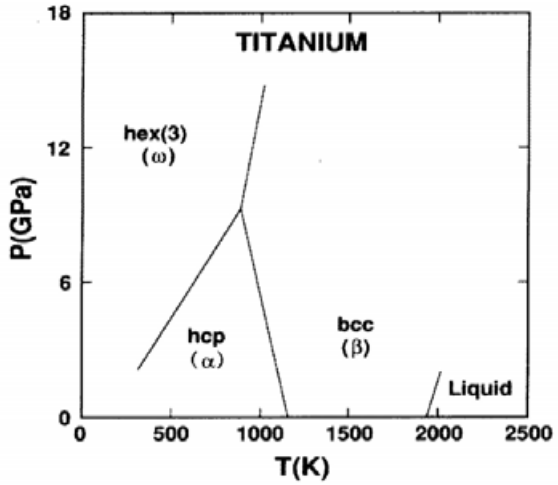

Figure 2.1-1: Titanium phase diagram. Source: http://www.physics.ohio-state.edu/~wilkins/group/phases/index.html>[

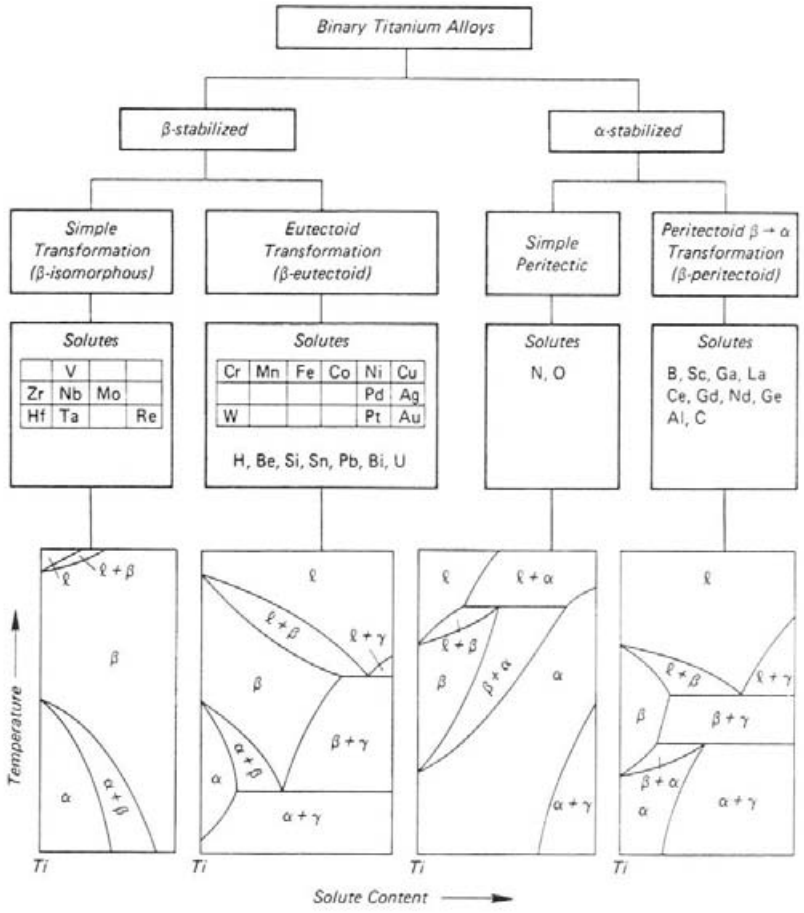

Figure 2.1-2: Classification scheme for binary titanium alloy phase diagrams. “α” and “β” are hcp and bcc solid-solution alloys, respectively, and “γ” represents an intermetallic compound (Molchanova 1965). Source: Materials Properties handbook, ASM international, page 9

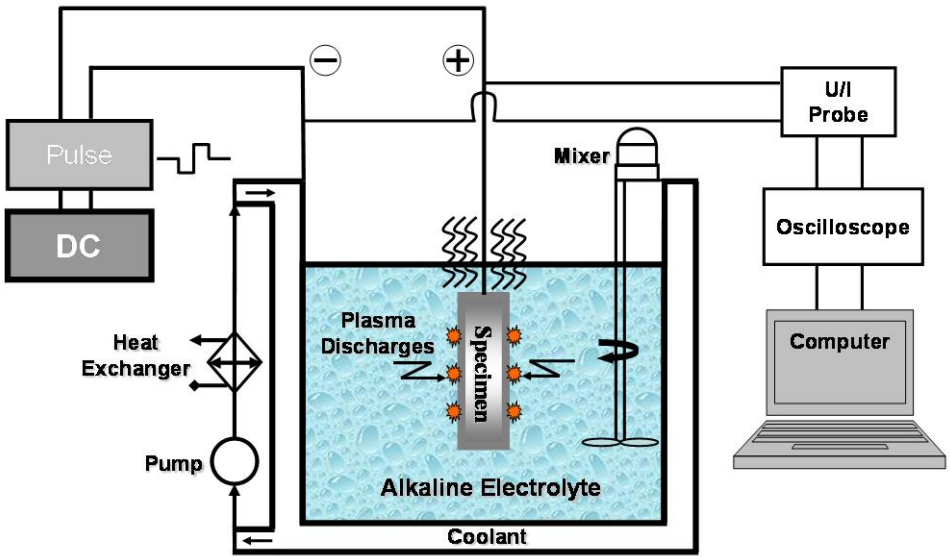

Figure 2.4-1: Schematic of PEO equipment

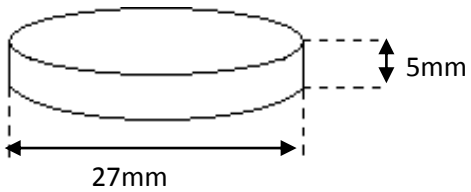

Figure 3.2-1: Coupon sample size

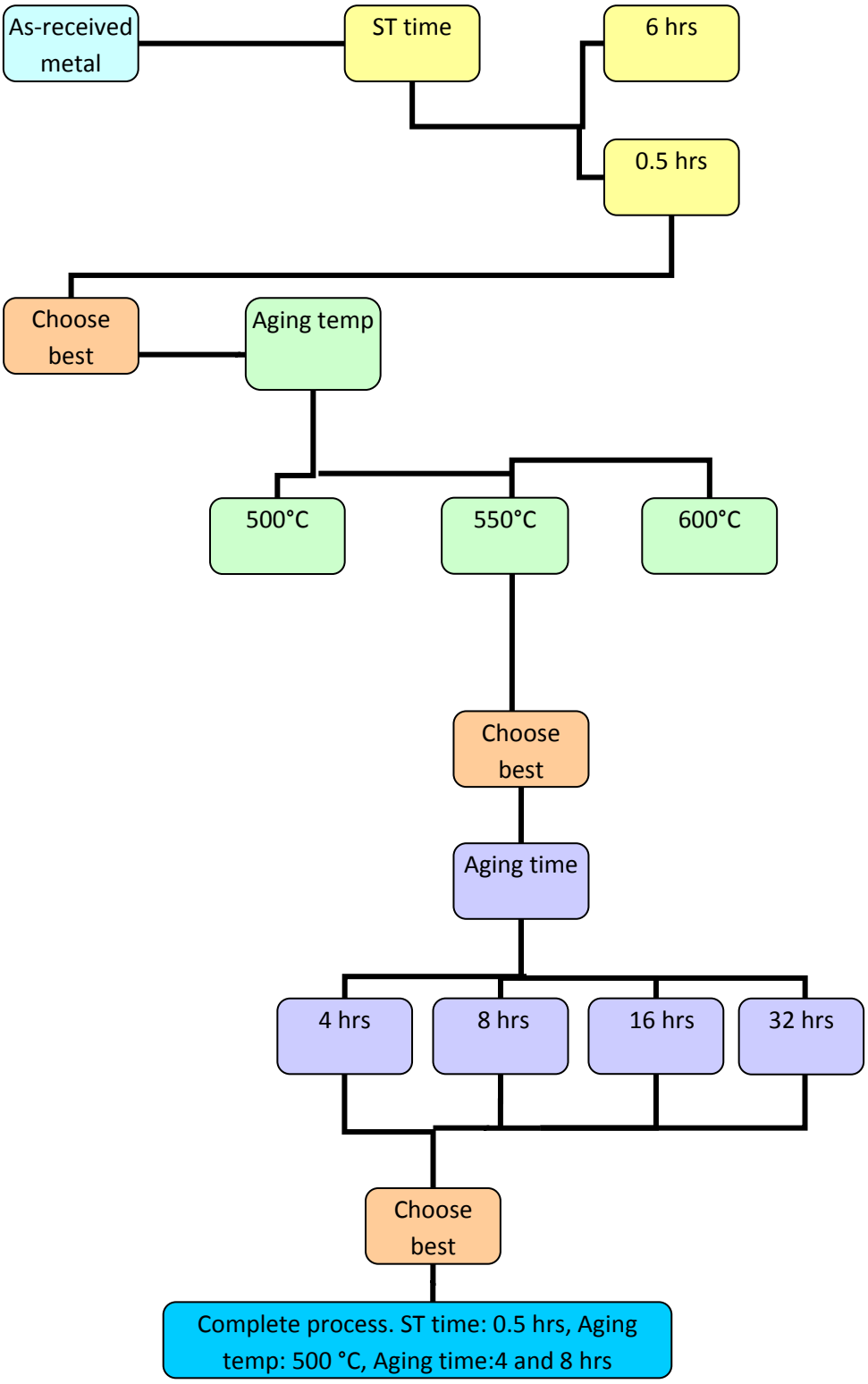

Figure 3.3-1: Flow diagram showing the treatment choice procedures

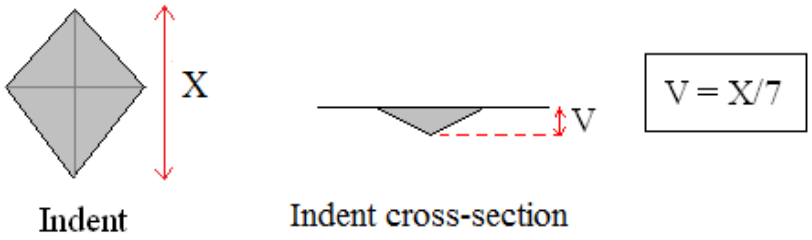

Figure 3.3-2: Schematic displaying method of removing oxide

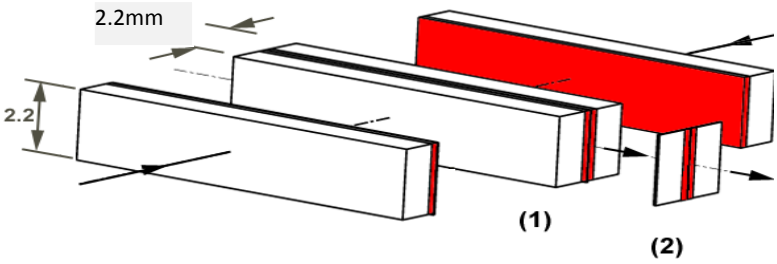

Figure 3.3-3: Schematic of pre-thinning XTEM sample preparation

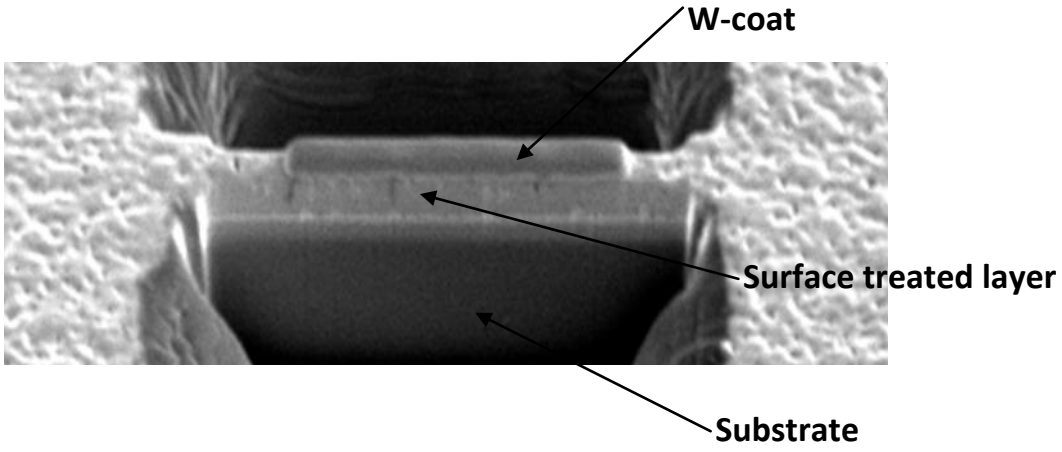

Figure 3.3-4: SEM image of FIB preparing cross-section TEM sample.

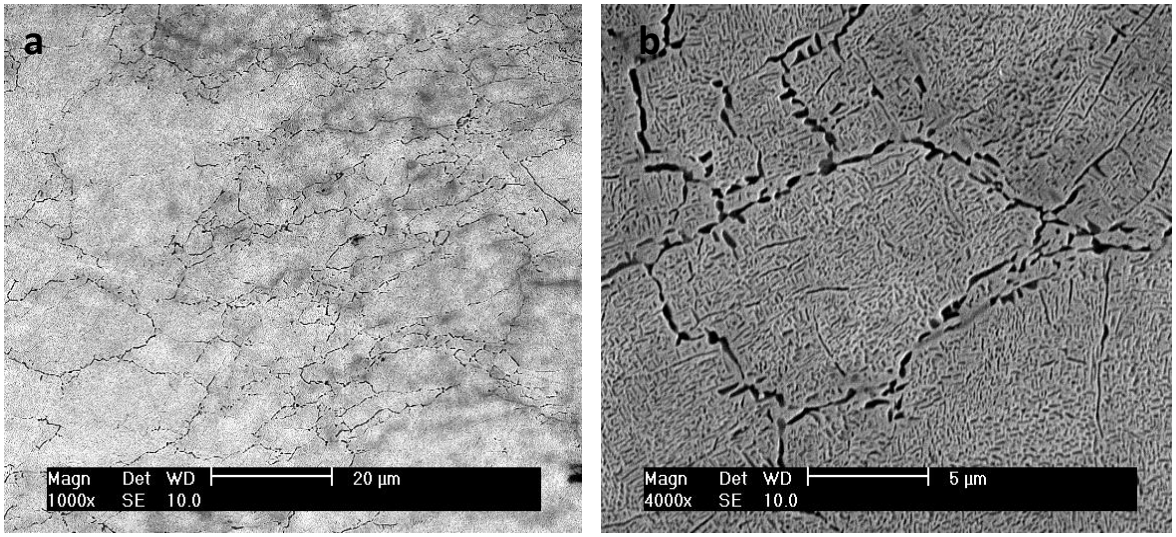

Figure 4.1-1: SEM micrographs of as-received (AR) TIMETAL LCB showing many grain boundaries (a) and a closer up image of the boundaries showing greater detail (b)

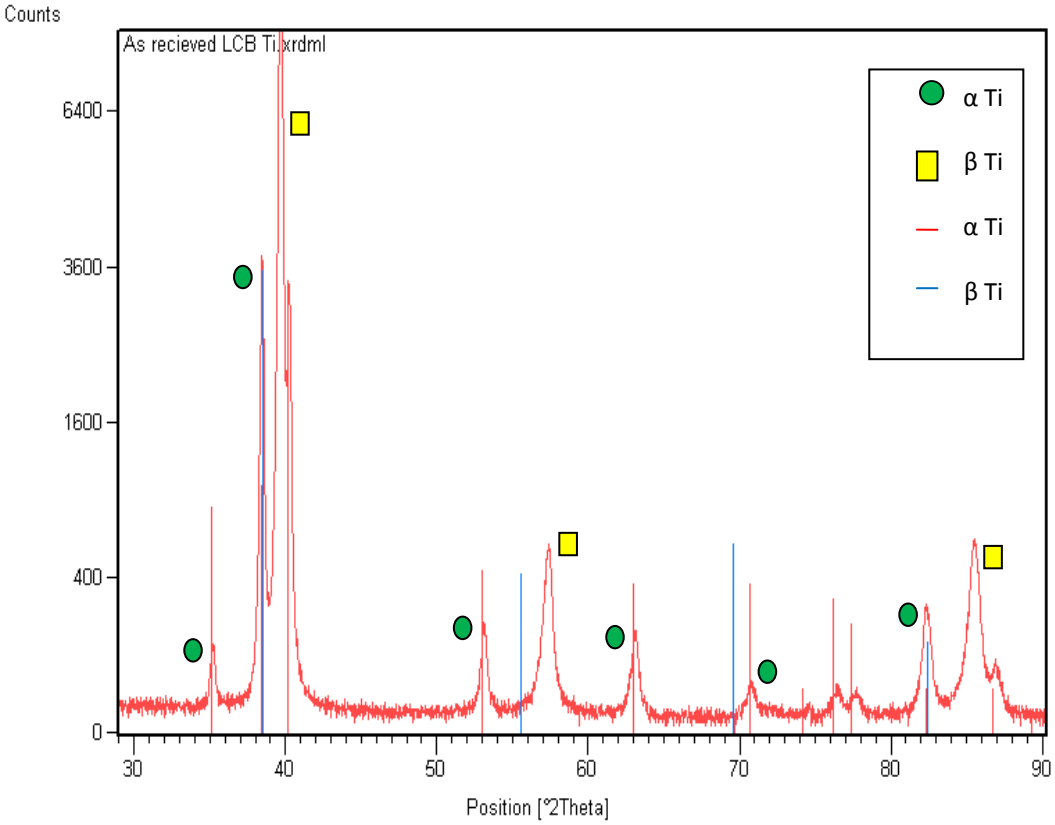

Figure 4.1-2: XRD graph showing the phase composition of the as-received material

a

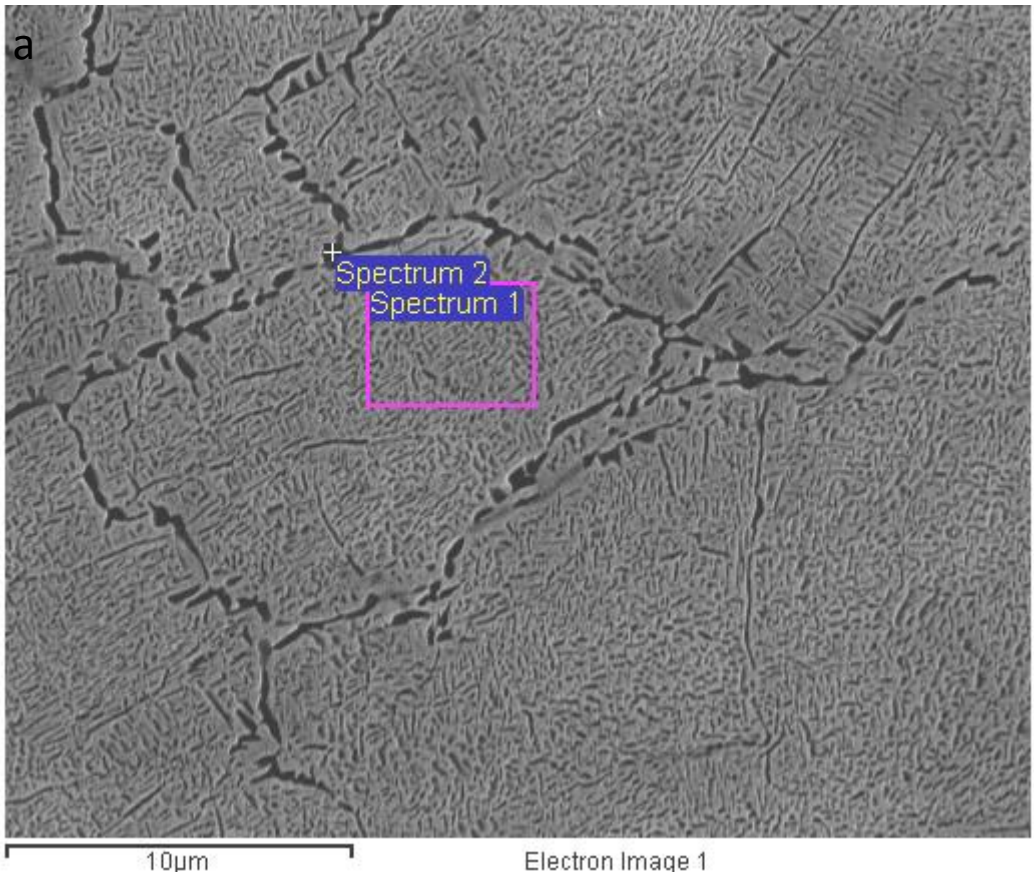

b

Spectrum	Ti	Mo	Fe	Al
1	87.89	6.49	4.21	1.41
2	86.69	7.14	4.71	1.46
Mean	87.29	6.82	4.46	1.44

Figure 4.1-3: SEM image of EDX points on as-received sample (a) and spectrum analysis (b). Spectrum 1 indicates an α+β Ti area, Spectrum 2 a α-Ti area

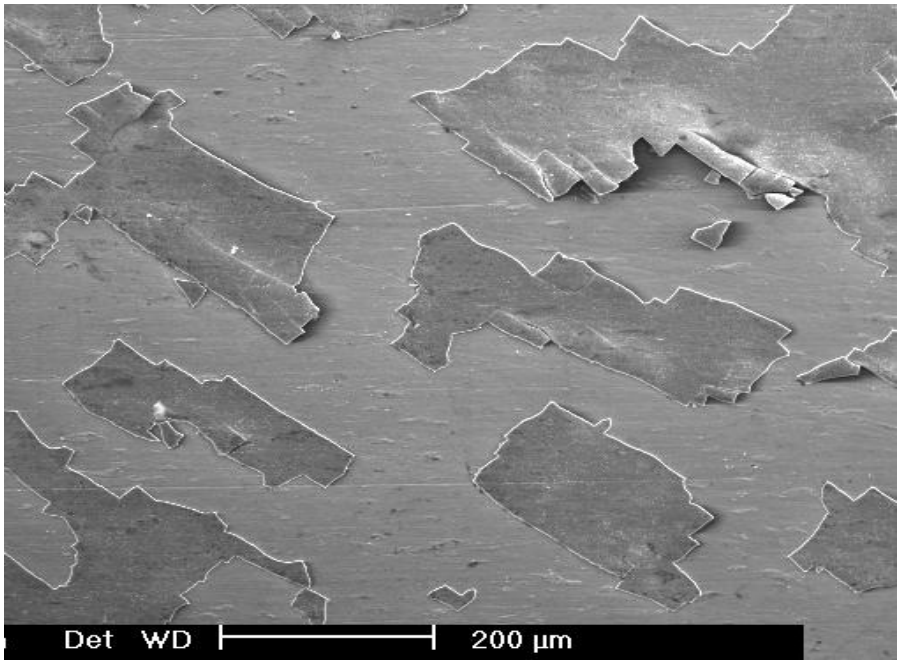

Figure 4.2-1: SEM image of the surface of ST6

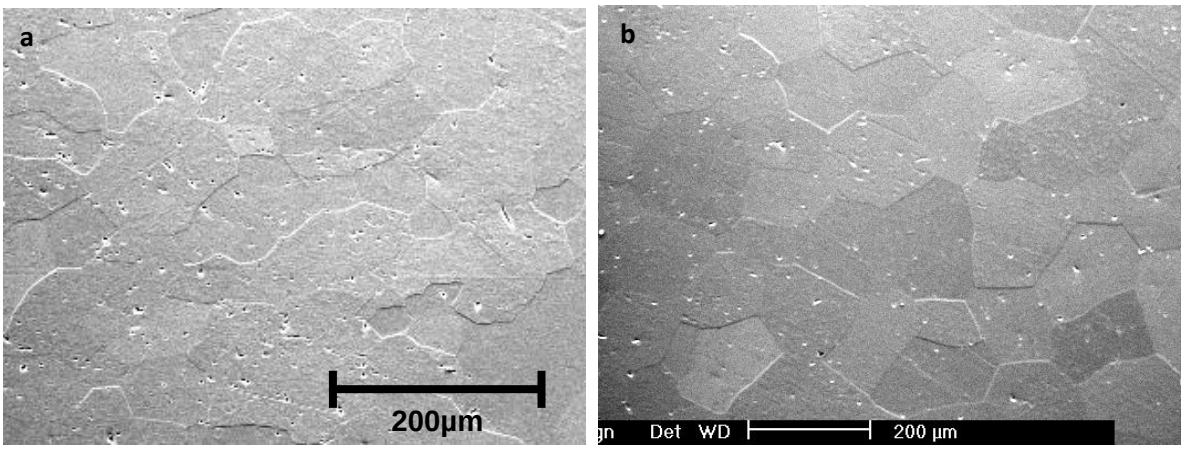

Figure 4.2-2: SEM images of the grain structure of ST0.5 (a) and ST6 (b)

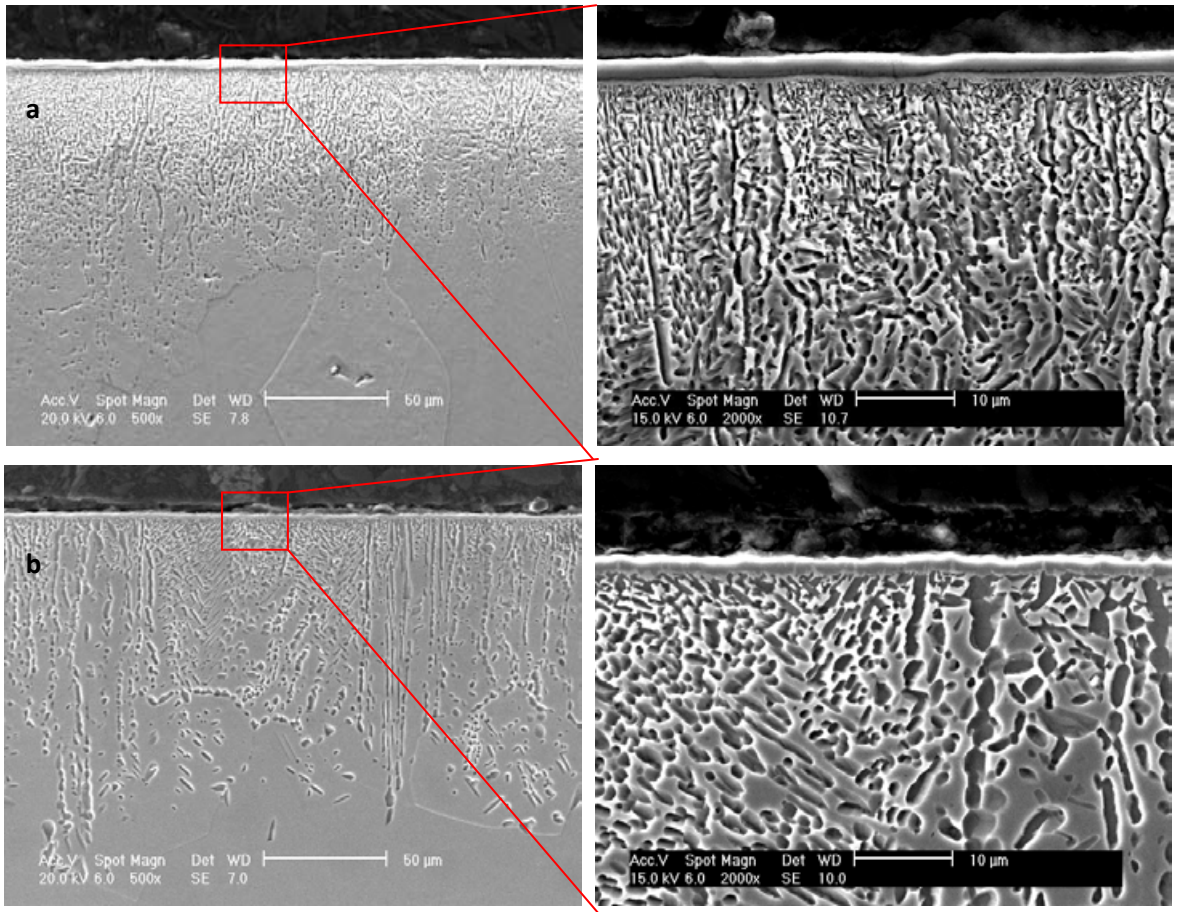

Figure 4.2-3: SEM images of the oxidation diffusion zone at far and close magnification of ST0.5 (a) and ST6 (b)

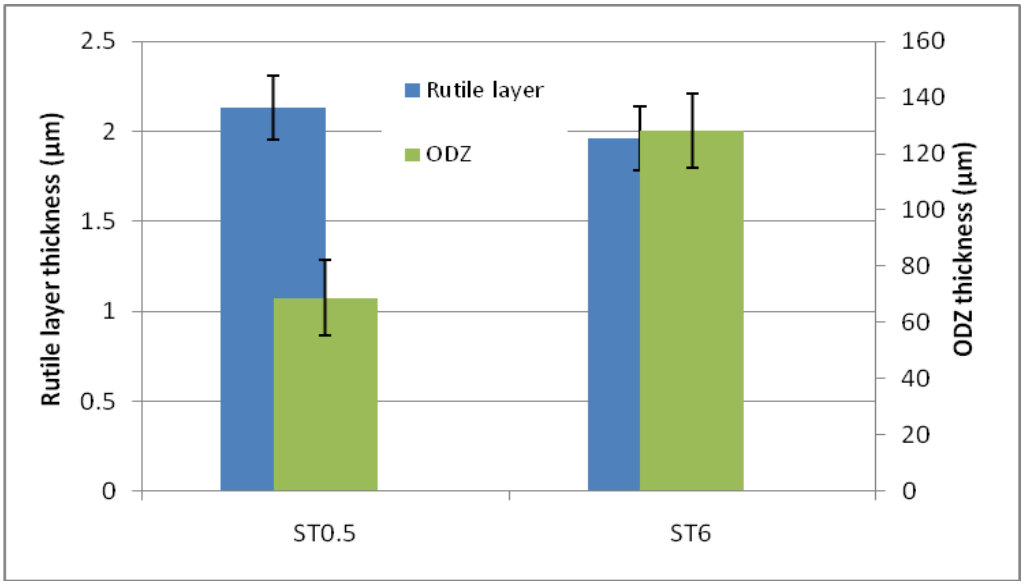

Figure 4.2-4: Bar chart displaying the rutile layer and ODZ thicknesses for ST0.5 and ST6 TIMETAL LCB samples

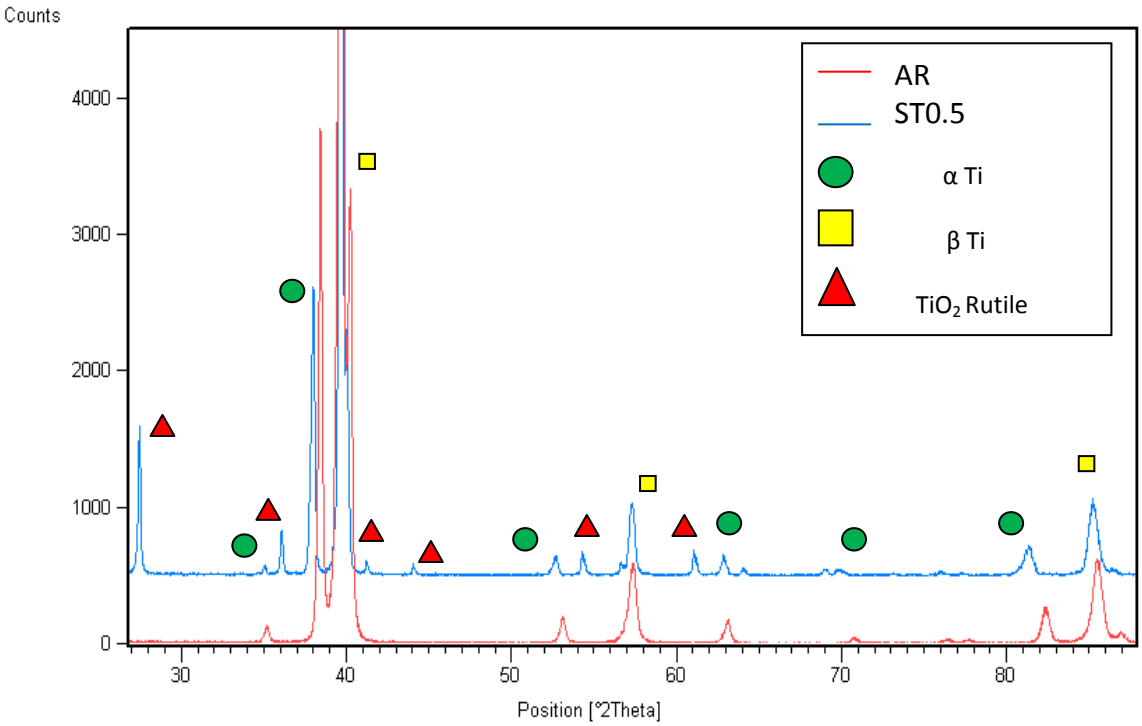

Figure 4.2-5: XRD patterns for as-received and ST0.5 TIMETAL LCB samples

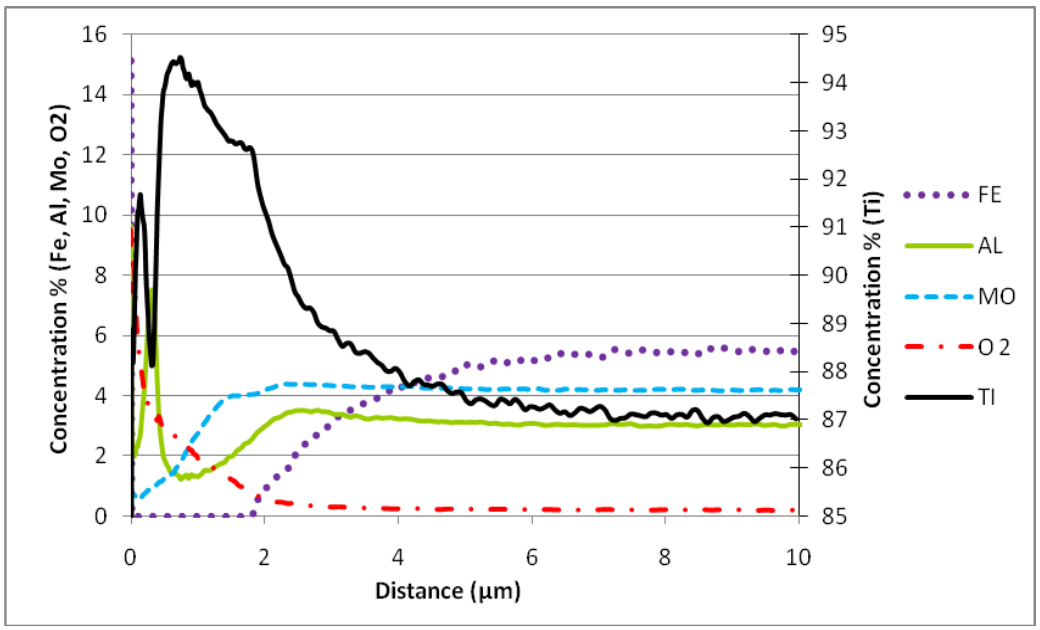

Figure 4.2-6: GDS mapping of elements present in depth profile of ST0.5

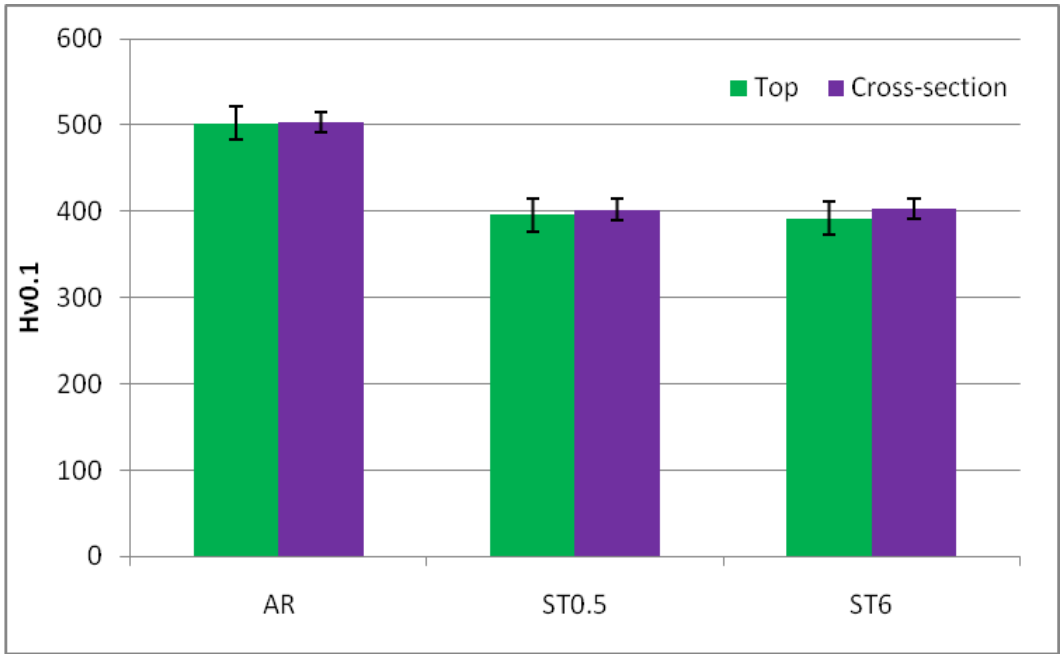

Figure 4.2-7: Microhardness values taken with a 100g load on as-received and solution treated samples. Averages of three indents are shown.

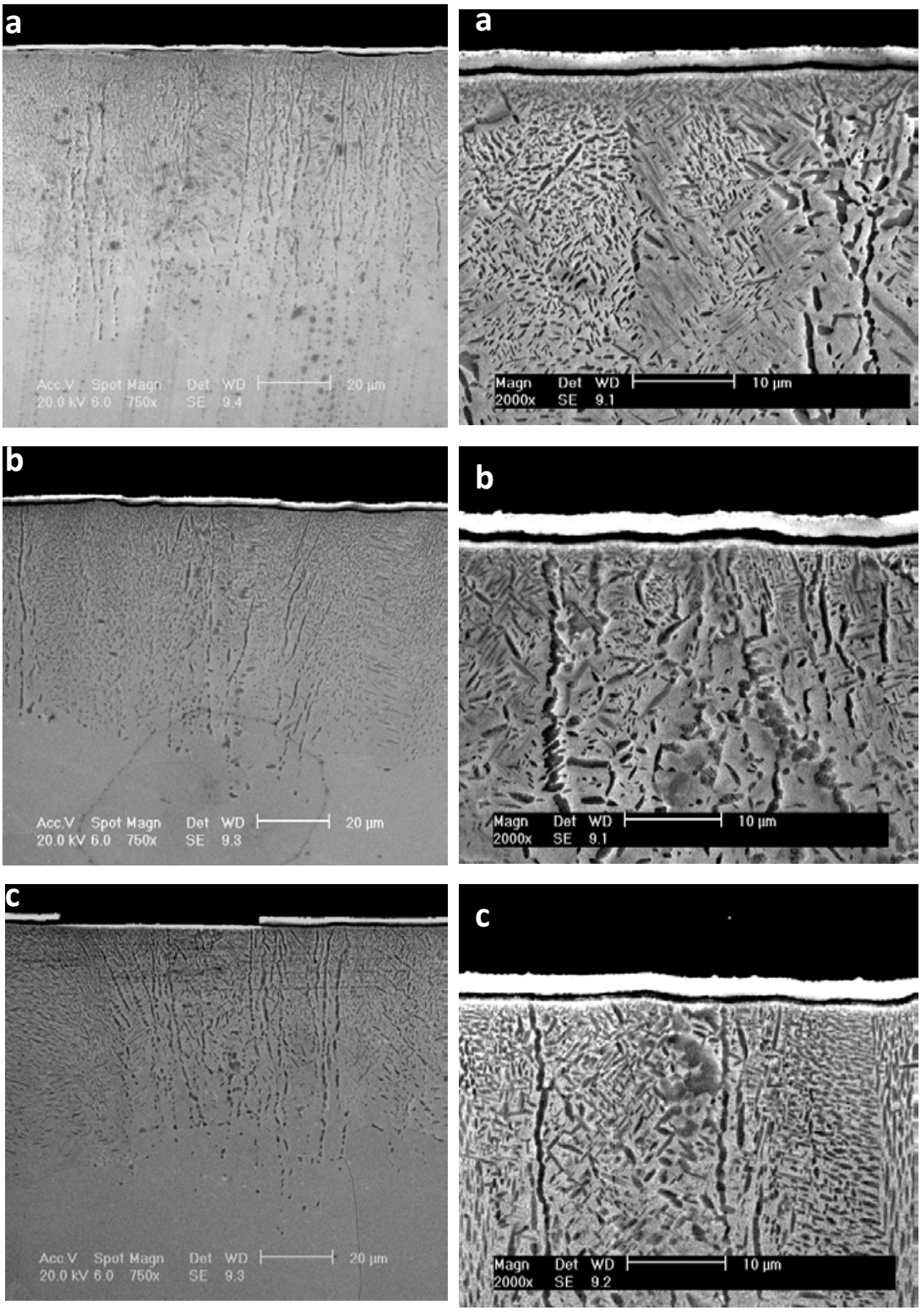

Figure 4.3-1: SEM micrographs of the oxygen diffusion zone at different magnifications from samples STA500_8 (a), STA550_8 (b) and STA600_8 (c)

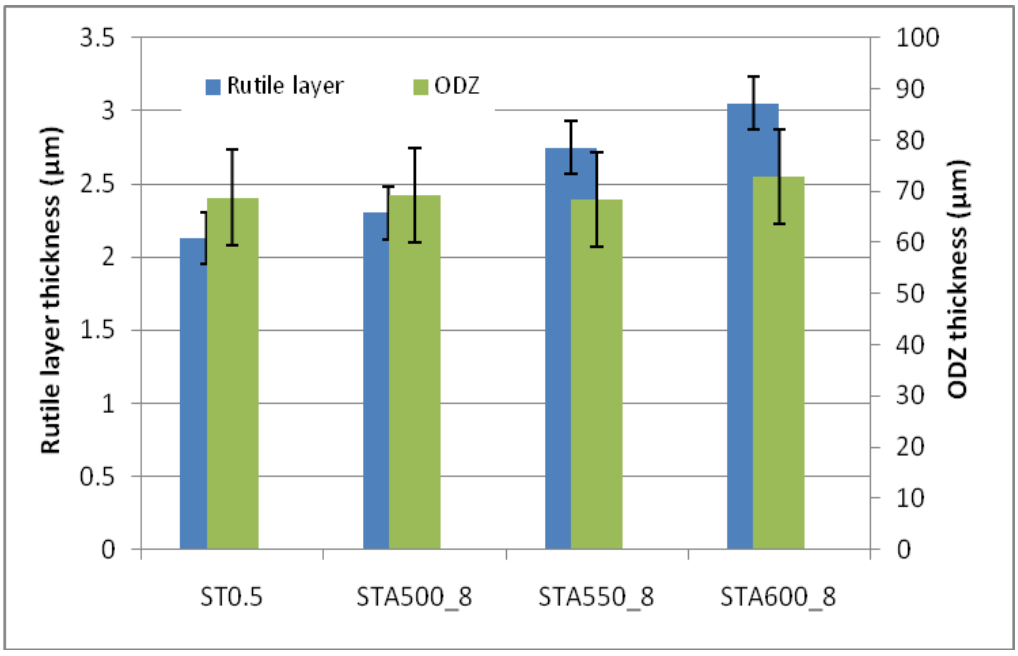

Figure 4.3-2: Bar chart displaying the thicknesses of the rutile TiO_2 layer and average oxygen diffusion zone (ODZ) from ST0.5 and samples aged for 8 hours at

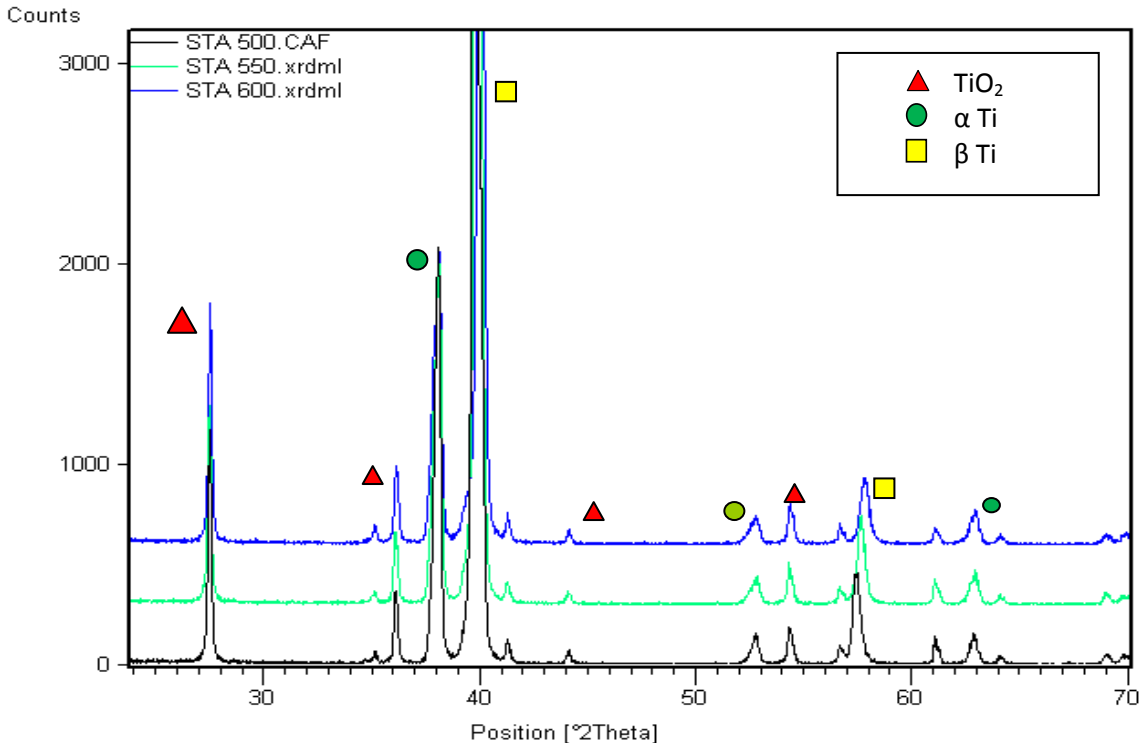

Figure 4.3-3: XRD patterns of samples STA500_8, STA550_8 and STA600_8.

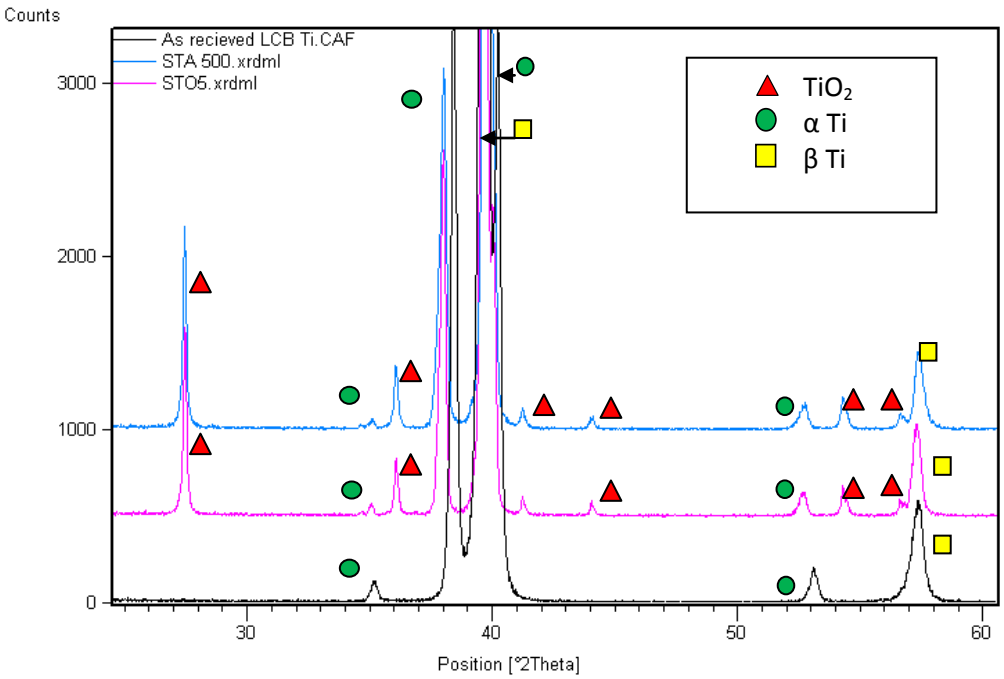

Figure 4.3-4: XRD patterns from three TIMETAL LCB samples; as- received (untreated) ST0.5 and STA500_8.

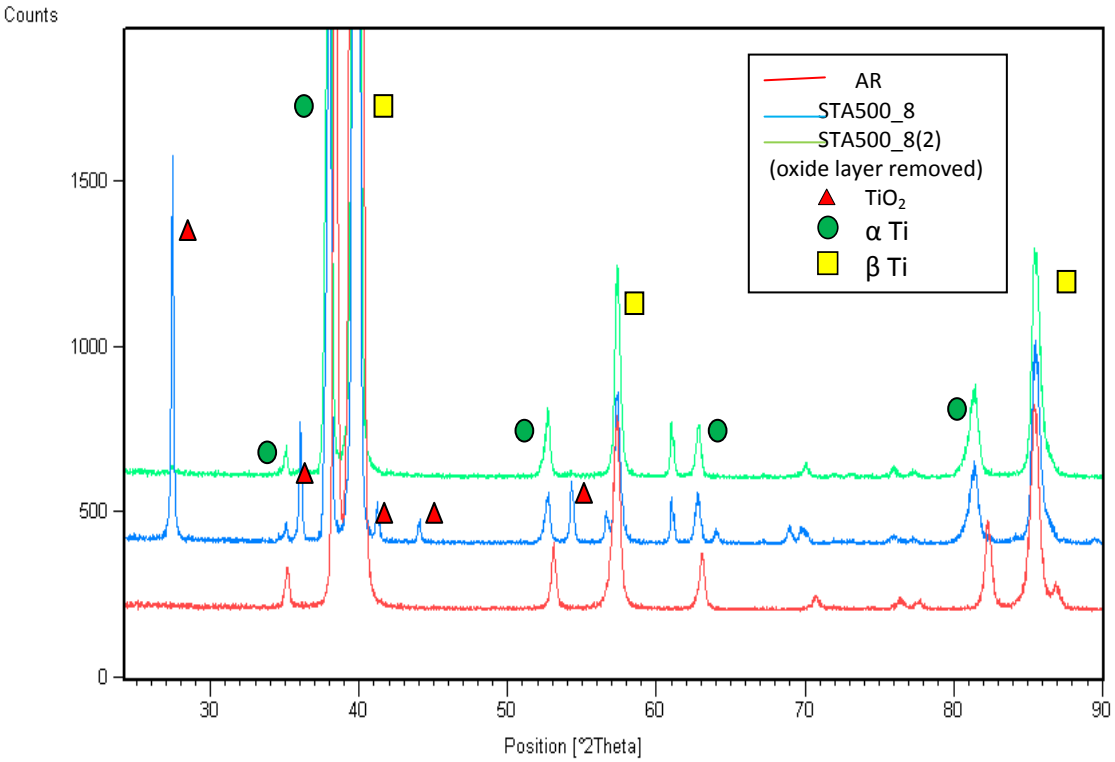

Figure 4.3-5: XRD reading of three TIMETAL LCB samples: as-received, STA500_8 and STA500_8 (2) which had its brittle oxide layer carefully removed

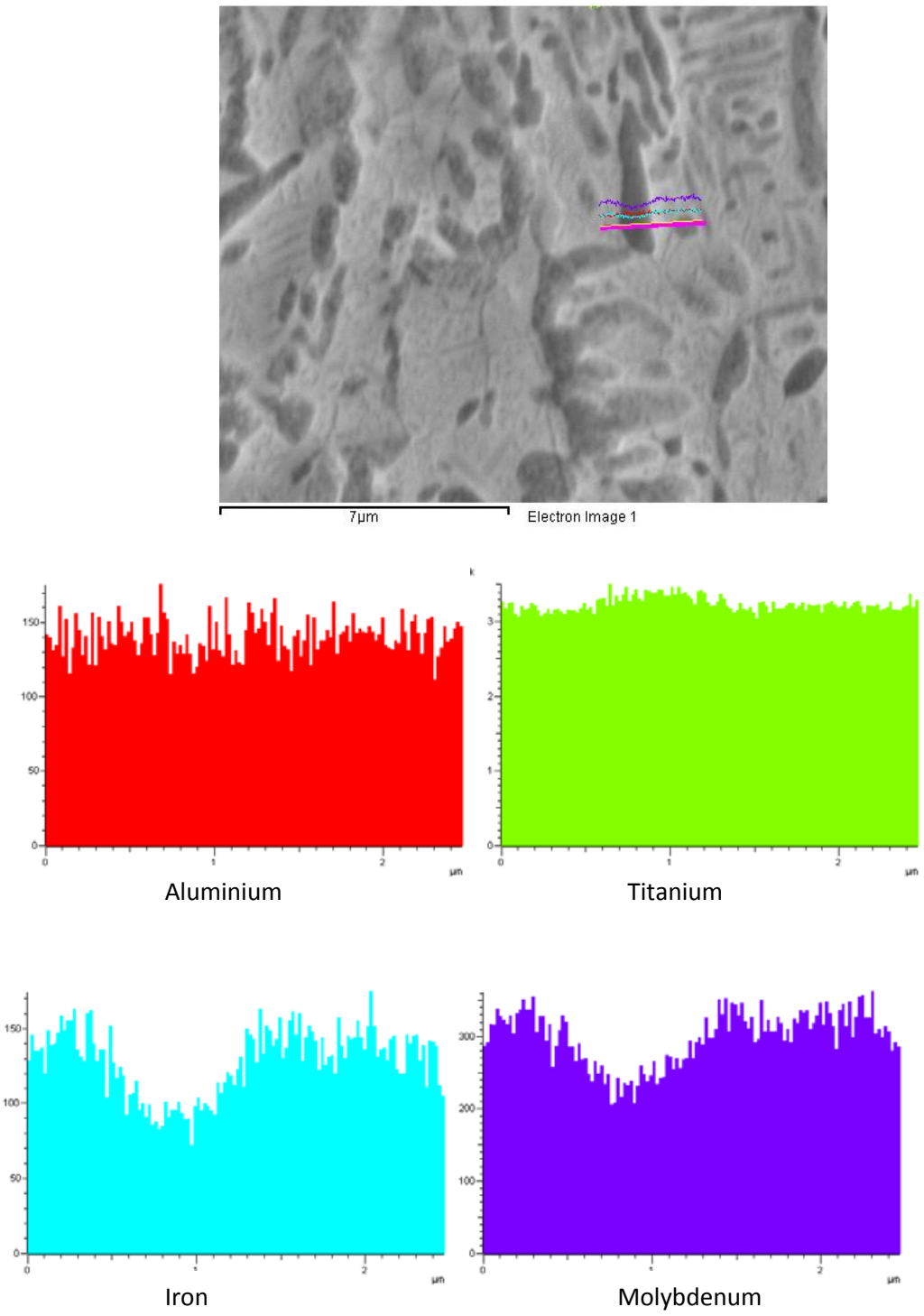

Figure 4.3-6: SEM image oxygen diffusion zone from sample STA500_8 and EDX elements line scans across an alpha titanium area (dark area).

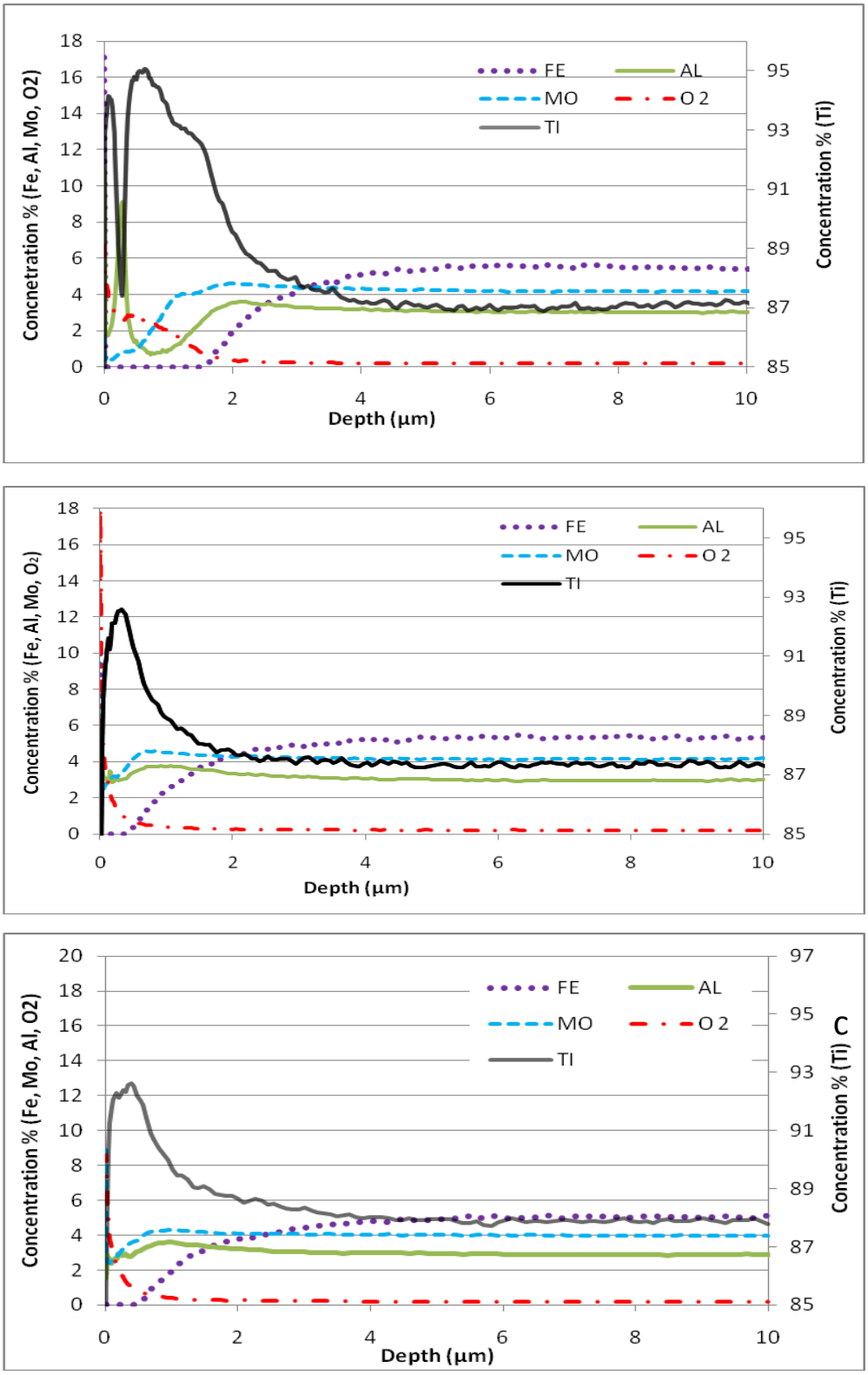

Figure 4.3-7: GDS depth profiles to show elemental change through the surface of STA500_8 (a), STA550_8 (b) and STA600_8 (c)

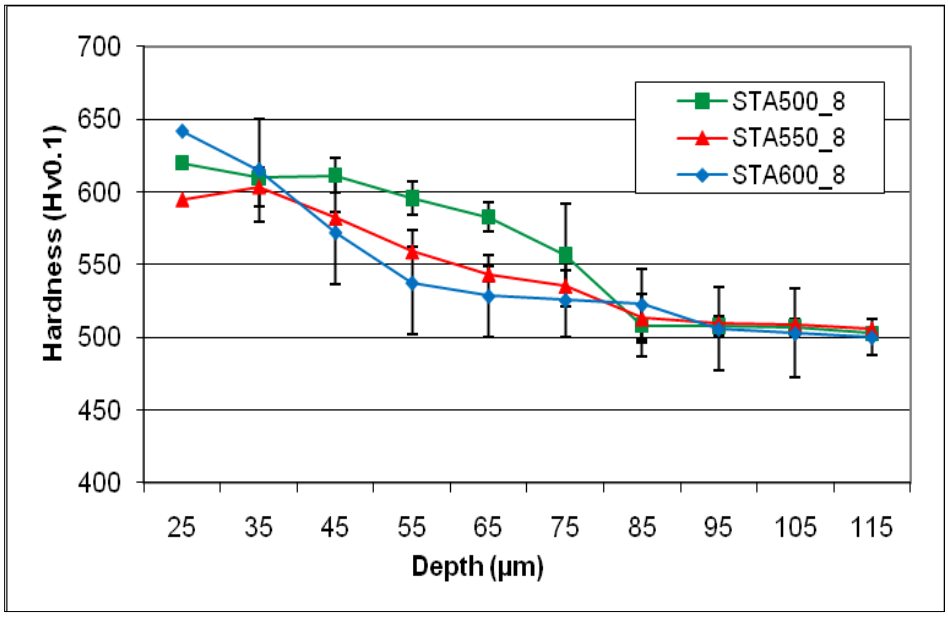

Figure 4.3-8: Hardness depth profiles of the samples aged at different temperatures for 8 hours

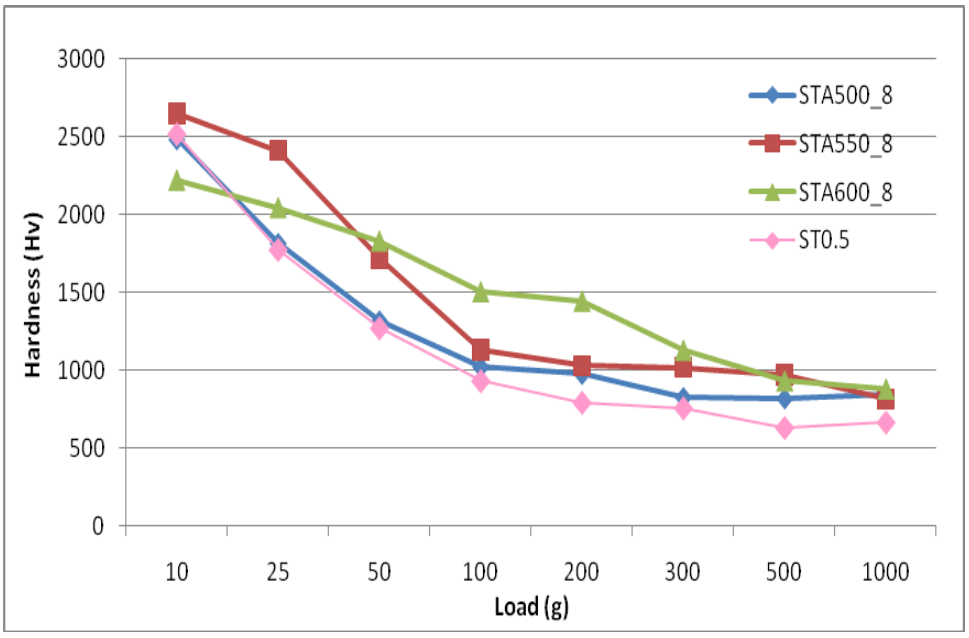

Figure 4.3-9: Load bearing capacity of samples ST0.5, STA500_8, STA550_8 and STA600_8

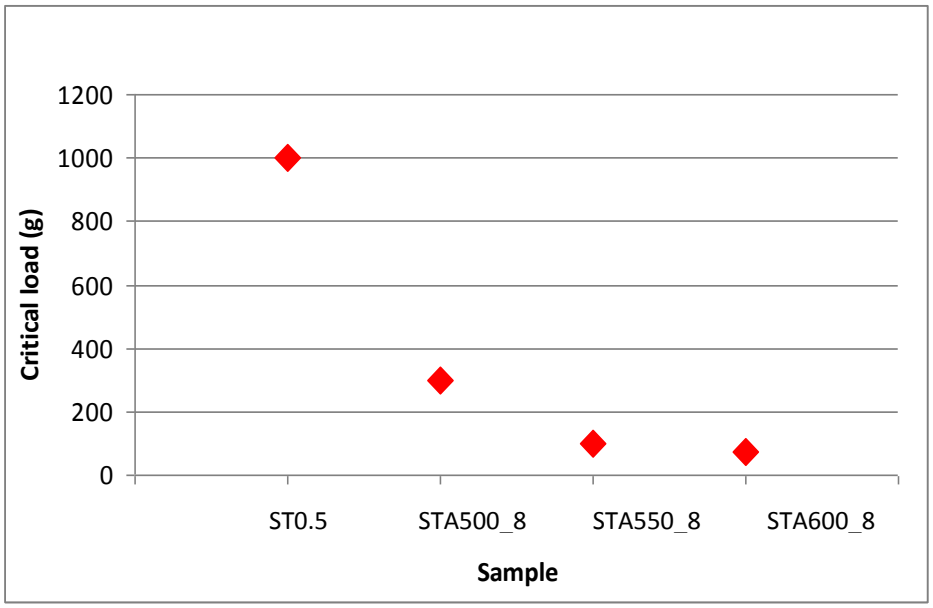

Figure 4.3-10: Critical loads for samples under different treatment conditions

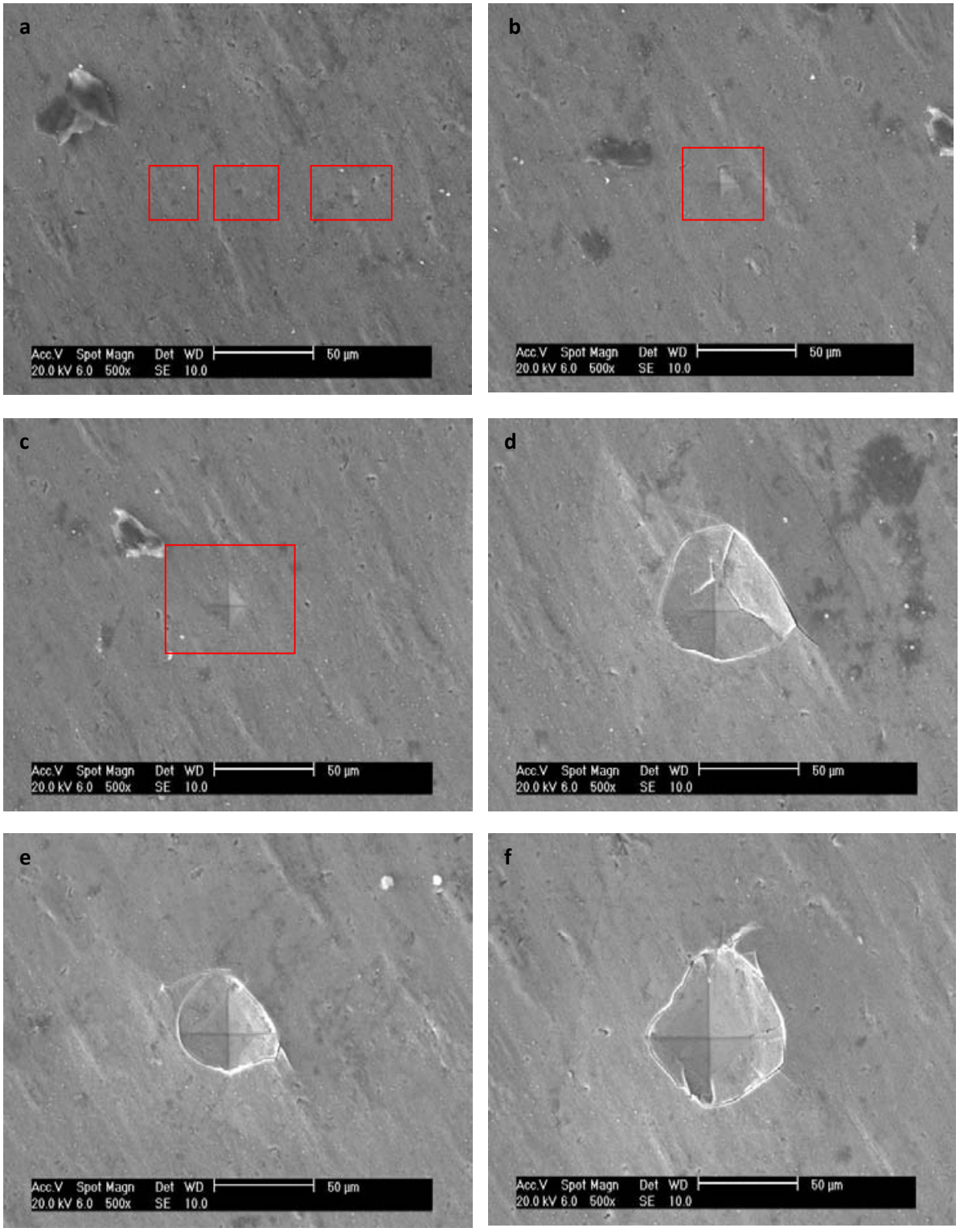

Figure 4.3-11: SEM images of micro-indents formed from increasing loads of 10g, 25g, 50g (a), 100g (b), 200g (c), 300g (d), 500g (e) and 1000g (d) on STA500_8.

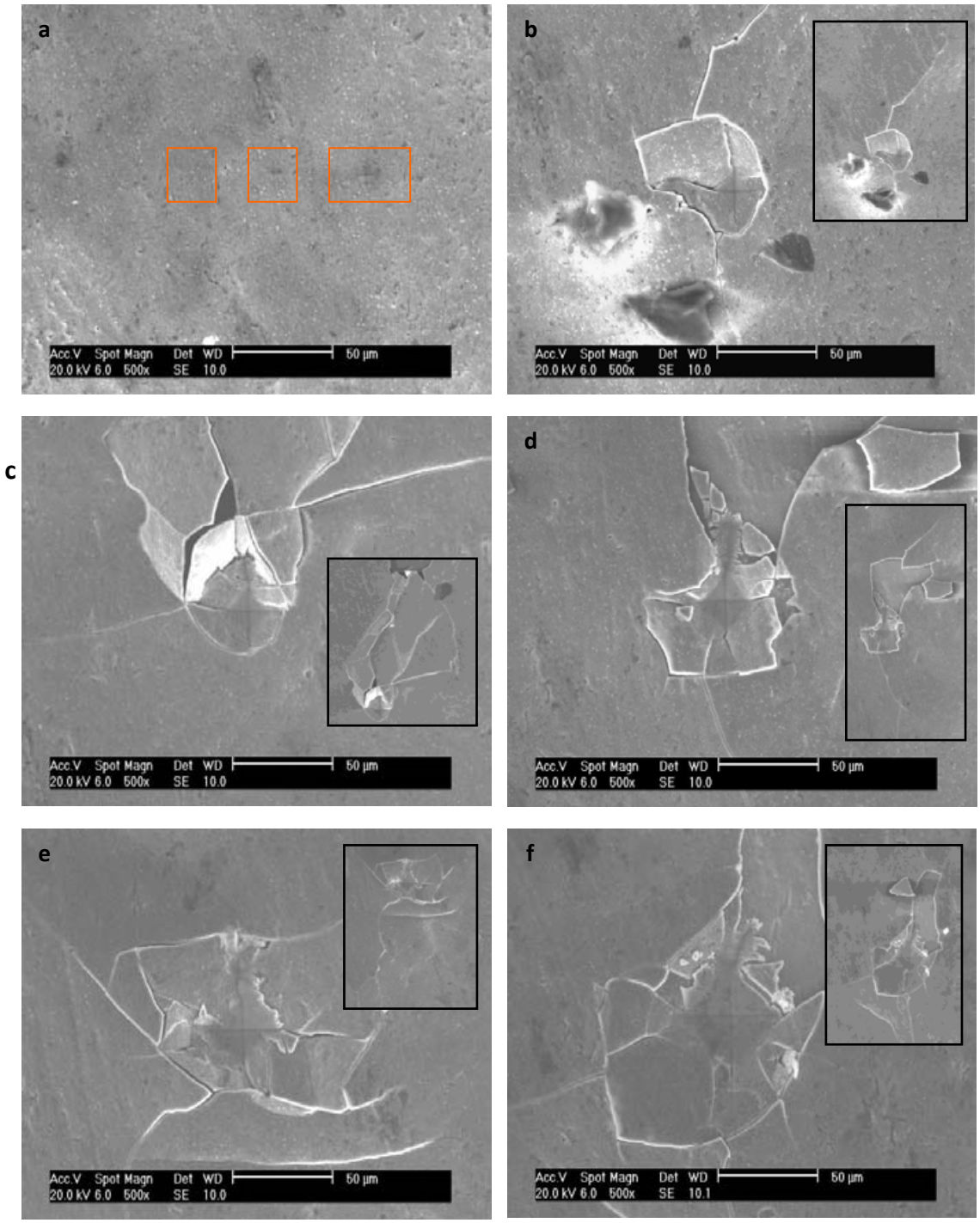

Figure 4.3-12: SEM images of micro-indents formed from increasing loads of 10g, 25g, 50g (a), 100g (b), 200g (c), 300g (d), 500g (e) and 1000g (f) on surface of STA550_8. Images at a lower magnification are provided in the corners to offer full view of the cracking.

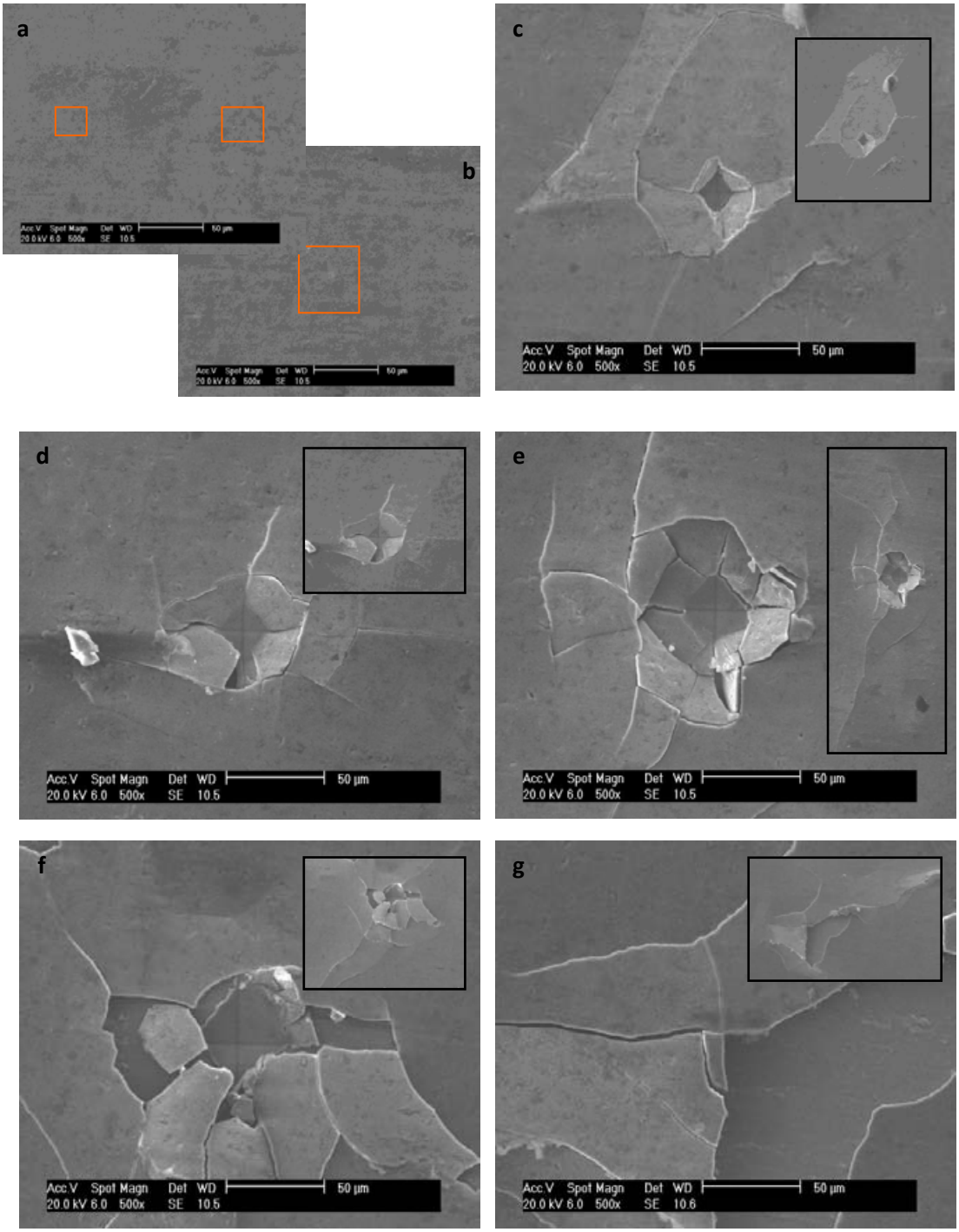

Figure 4.3-13: SEM images of micro-indents formed from increasing loads of 10g, 25g (a), 50g (b) 100g (c), 200g (d), 300g (e), 500g (f) and 1000g (g) on STA600_8. Images at a lower magnification of 200x are provided in the corners to offer full view of the cracking.

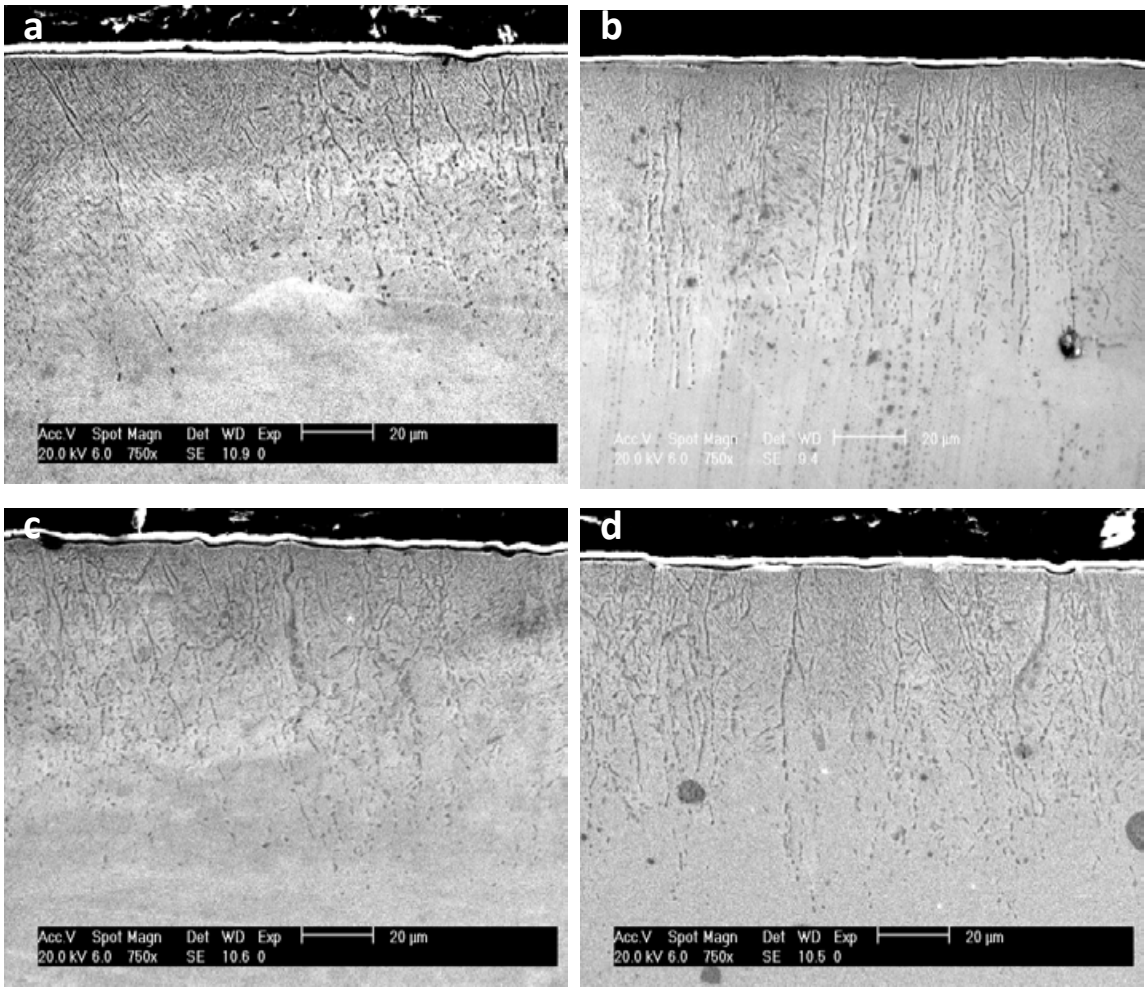

Figure 4.3-14: SEM images of cross-section layer structures for STA500_4 (a), STA500_8 (b), STA500_16 (c) and STA500_32 (d) samples.

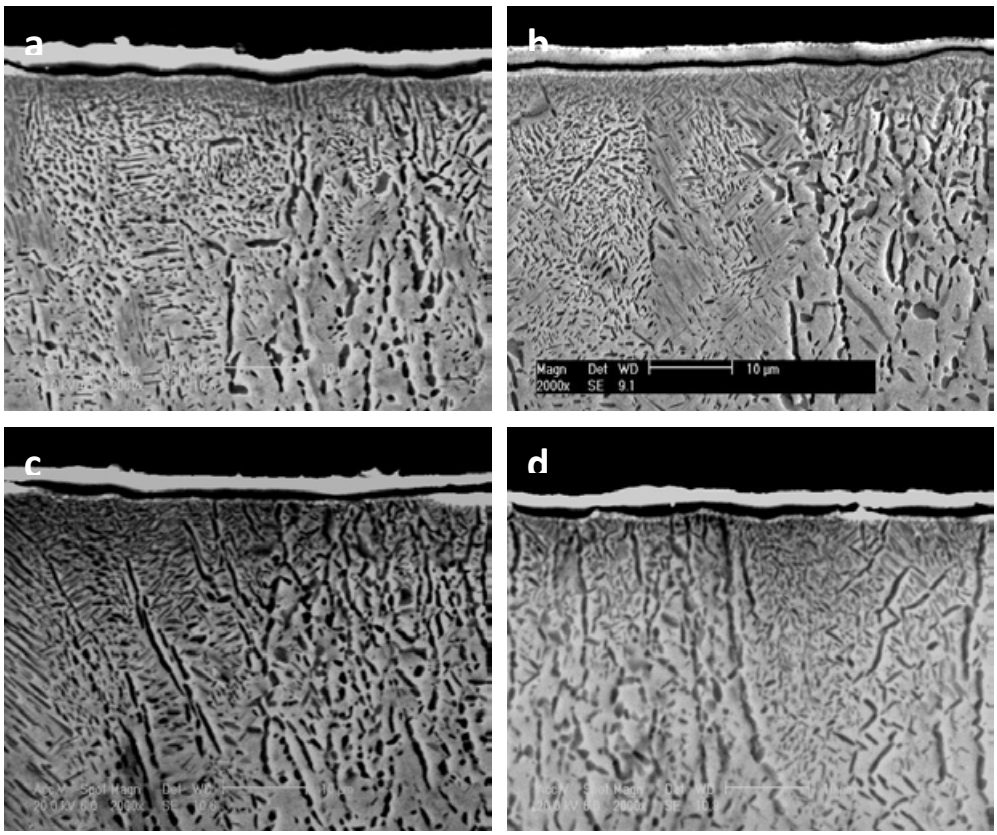

Figure 4.3-15: SEM images of cross-section layer structures for samples STA500_4 (a), STA500_8 (b), STA500_16 (c) and STA500_32 (d) showing the effect of aging time on the rutile layer thickness and ODZ structure

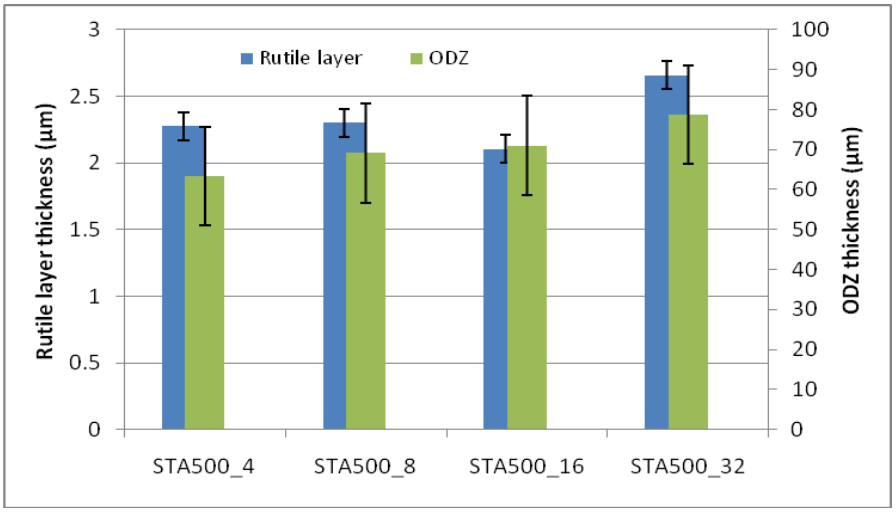

Figure 4.3-16: Rutile TiO_2 layer thickness and oxygen diffusion zone (ODZ) thickness for samples aged at 500 °C for differing lengths of aging time

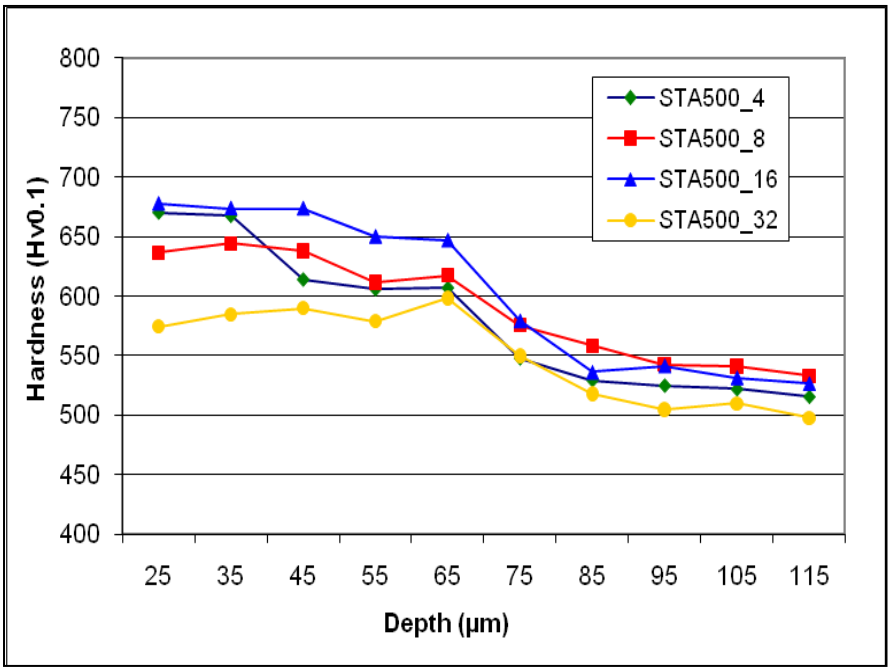

Figure 4.3-17: Microhardness depth profiles for samples solution treated at 850 °C for 0.5 hours, quenched and then aged at 500 °C for varying lengths of time.

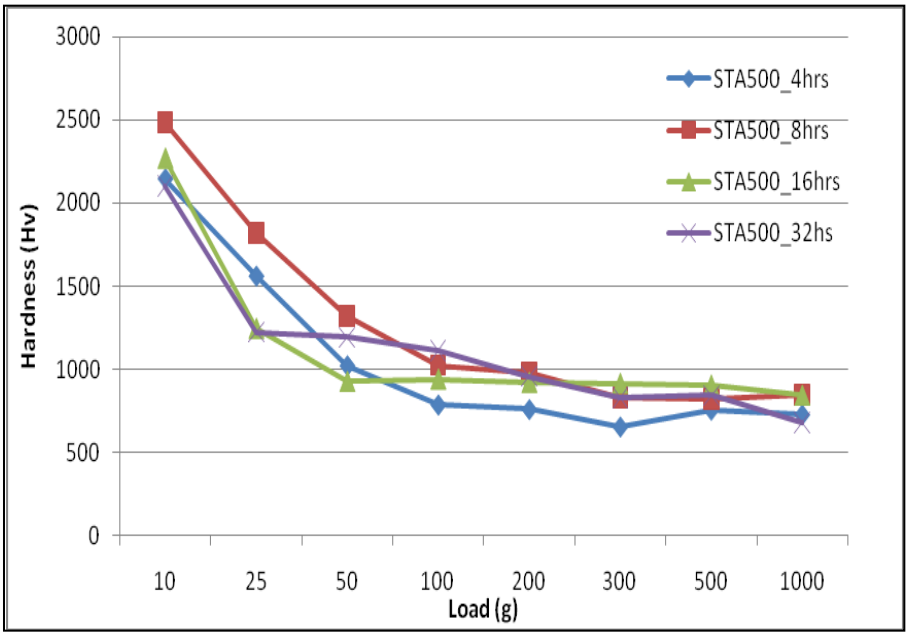

Figure 4.3-18 Load bearing capacity of the samples aged at different temperatures.

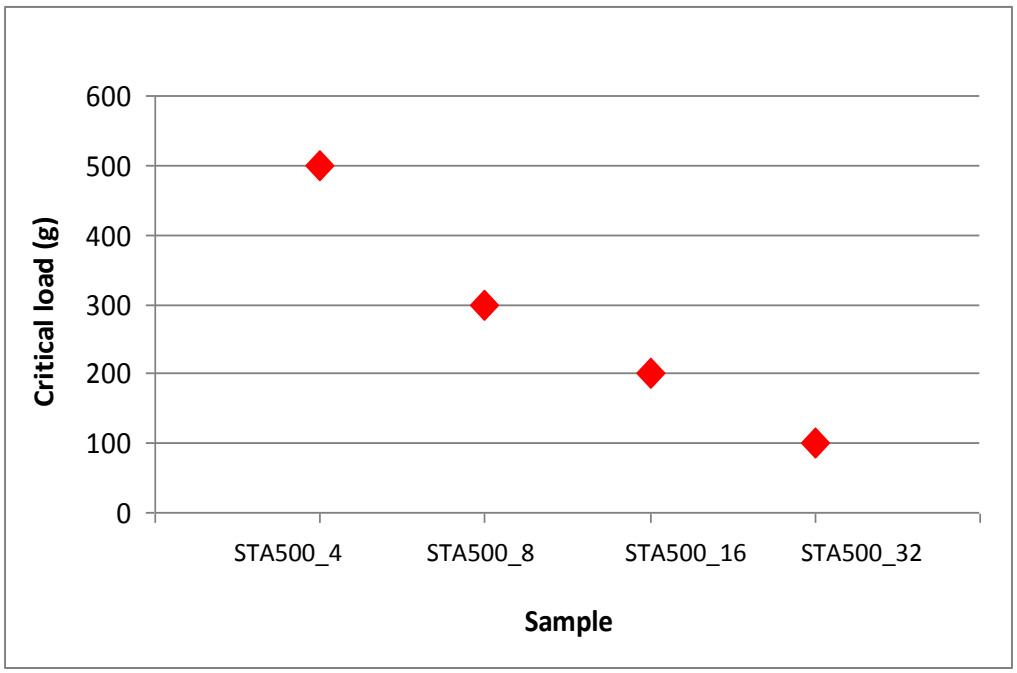

Figure 4.3-19: Aging time affect on the critical load at which the oxide film cracked.

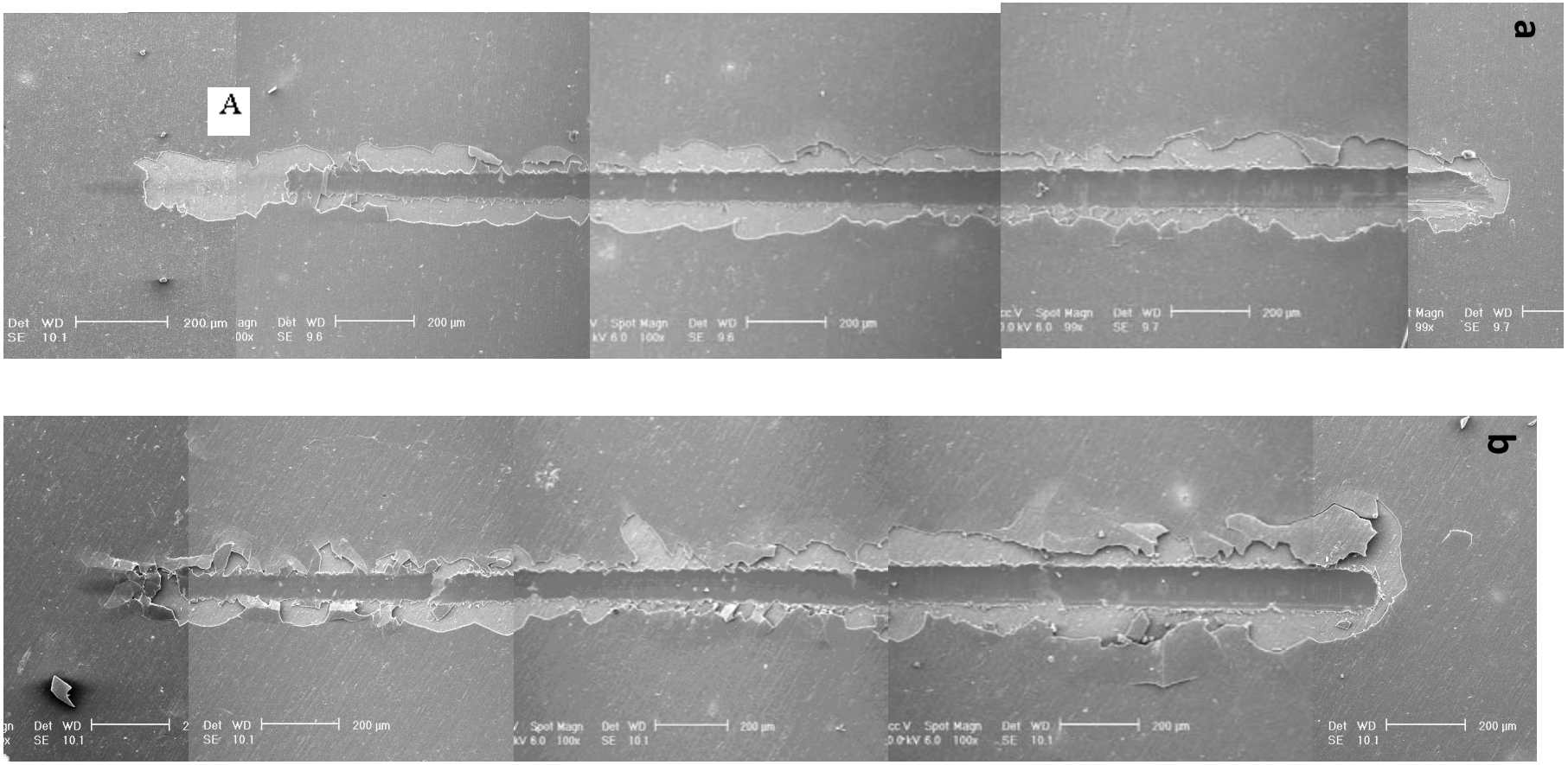

Figure 4.3-20 SEM images of scratch test marks on STA500_4 sample (a) and STA500_8

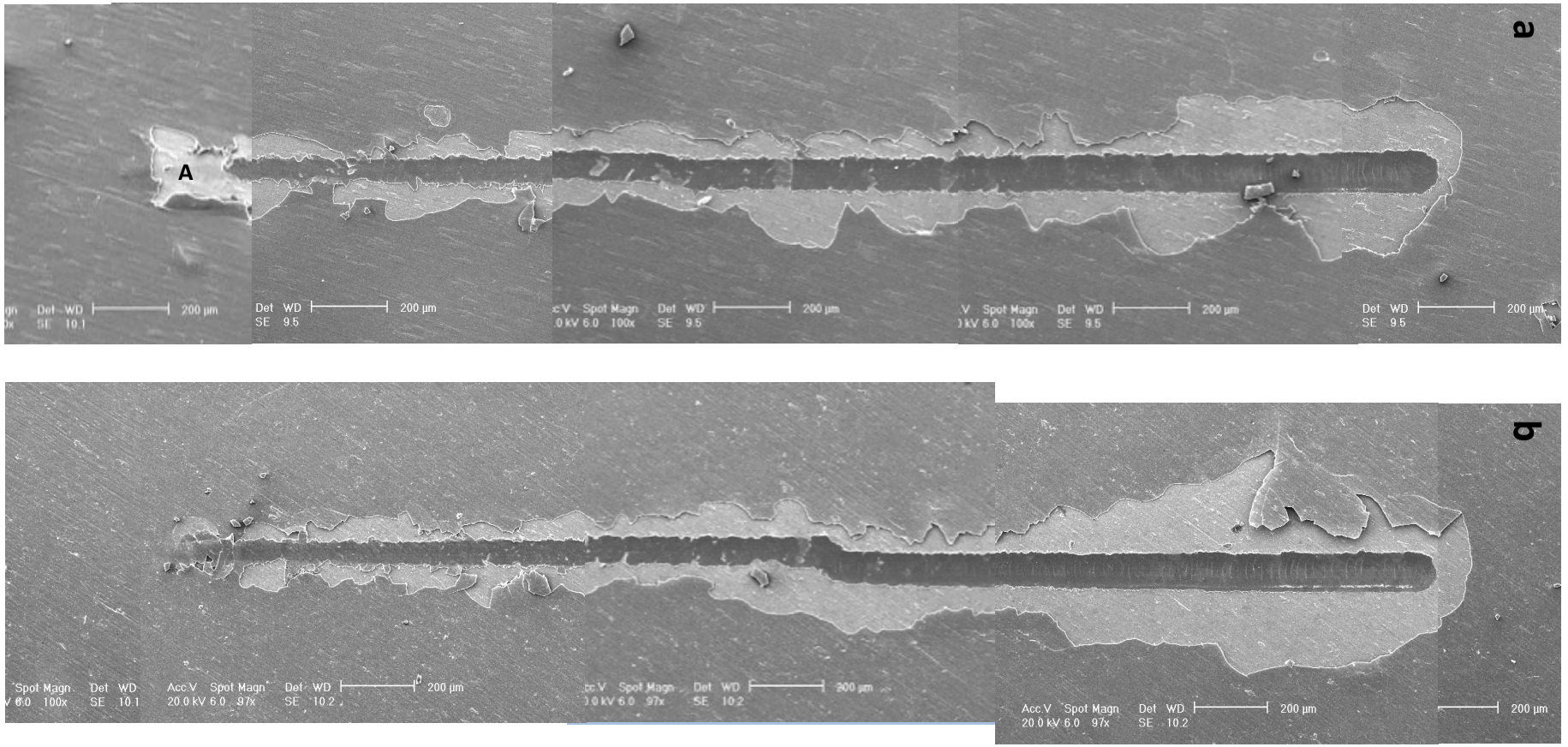

Figure 4.3-21 SEM images of scratch test marks on STA500_16 sample (a) and STA500_32

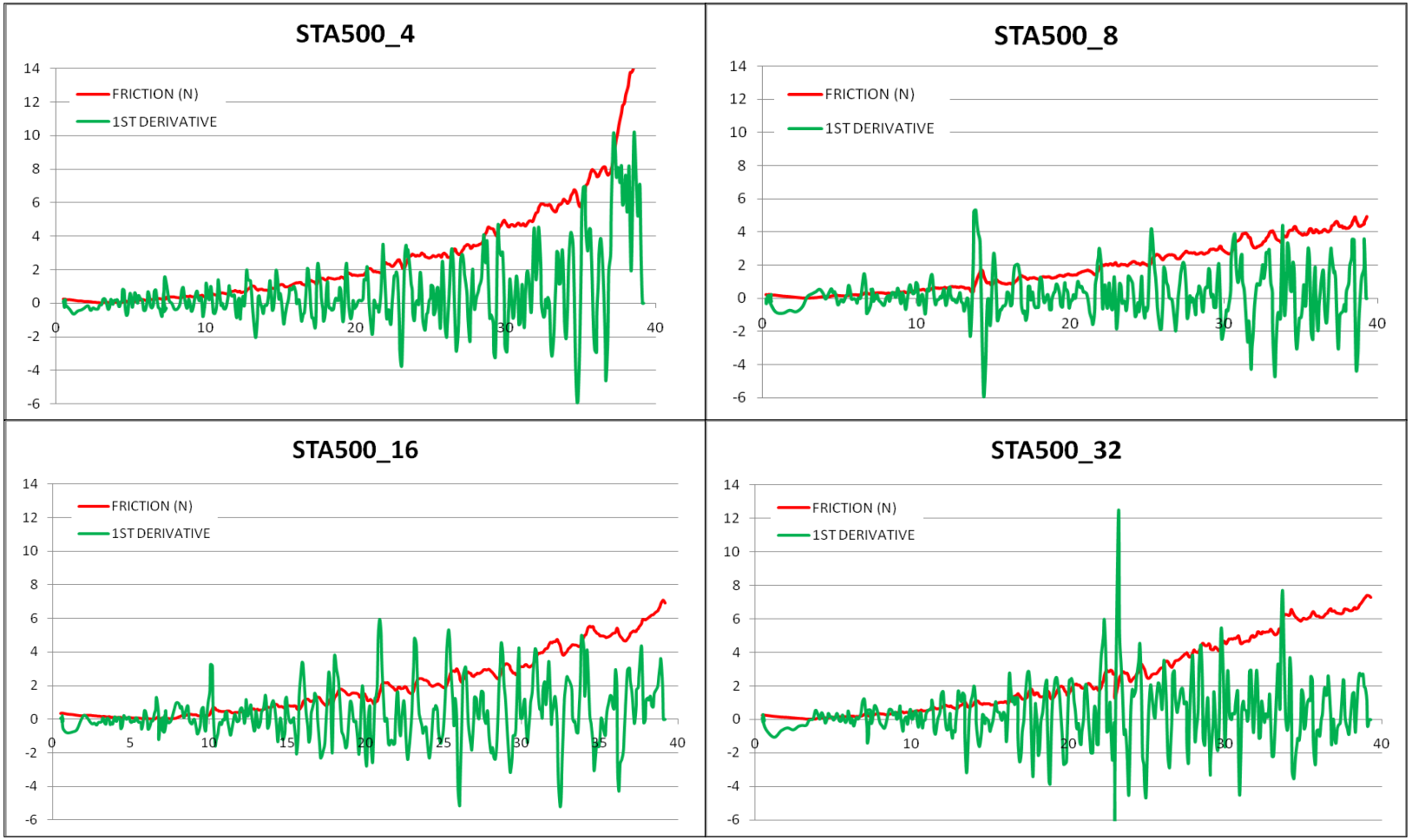

Figure 4.3-22: Scatter line graphs from the scratch tests on samples treated with process STA500 for 4 hours (a), 8 hours (b), 16 hours (c) and 32 hours (d)

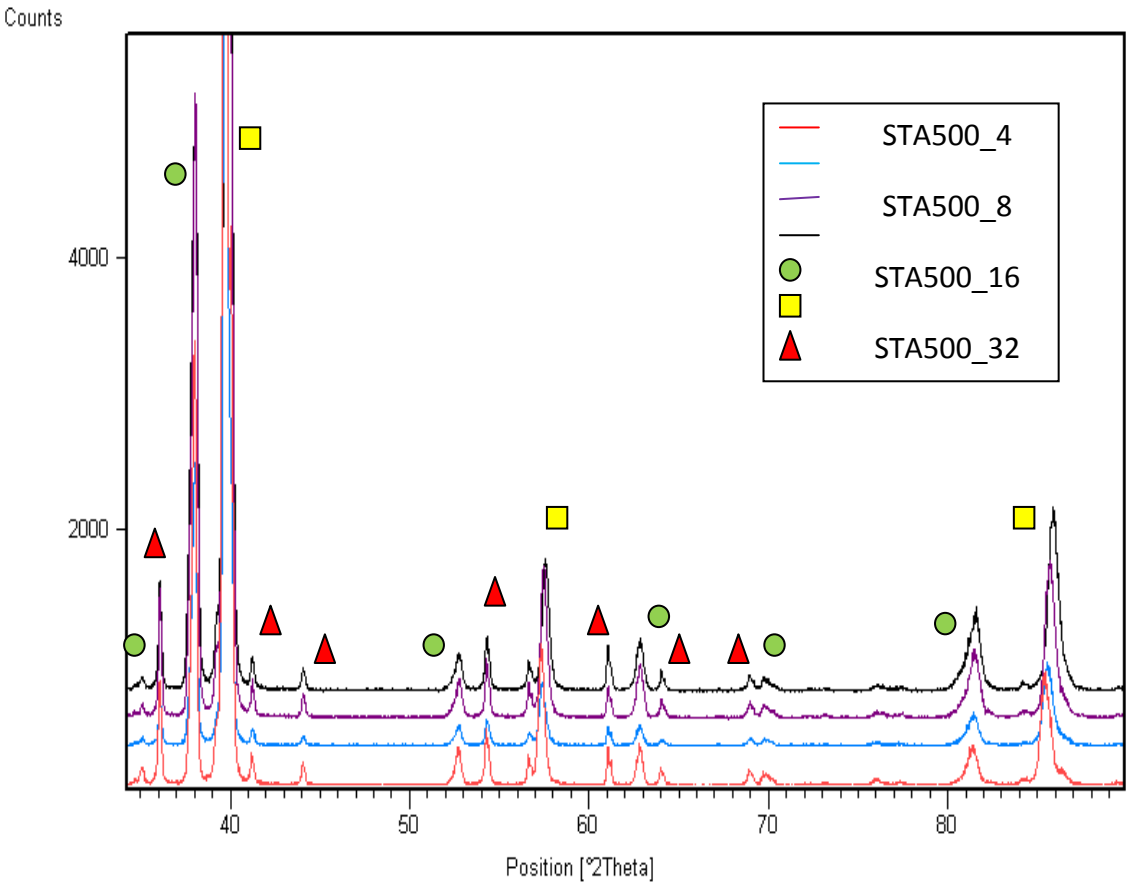

Figure 4.3-23: XRD patterns for samples aged at temperature 500°C for different length of times

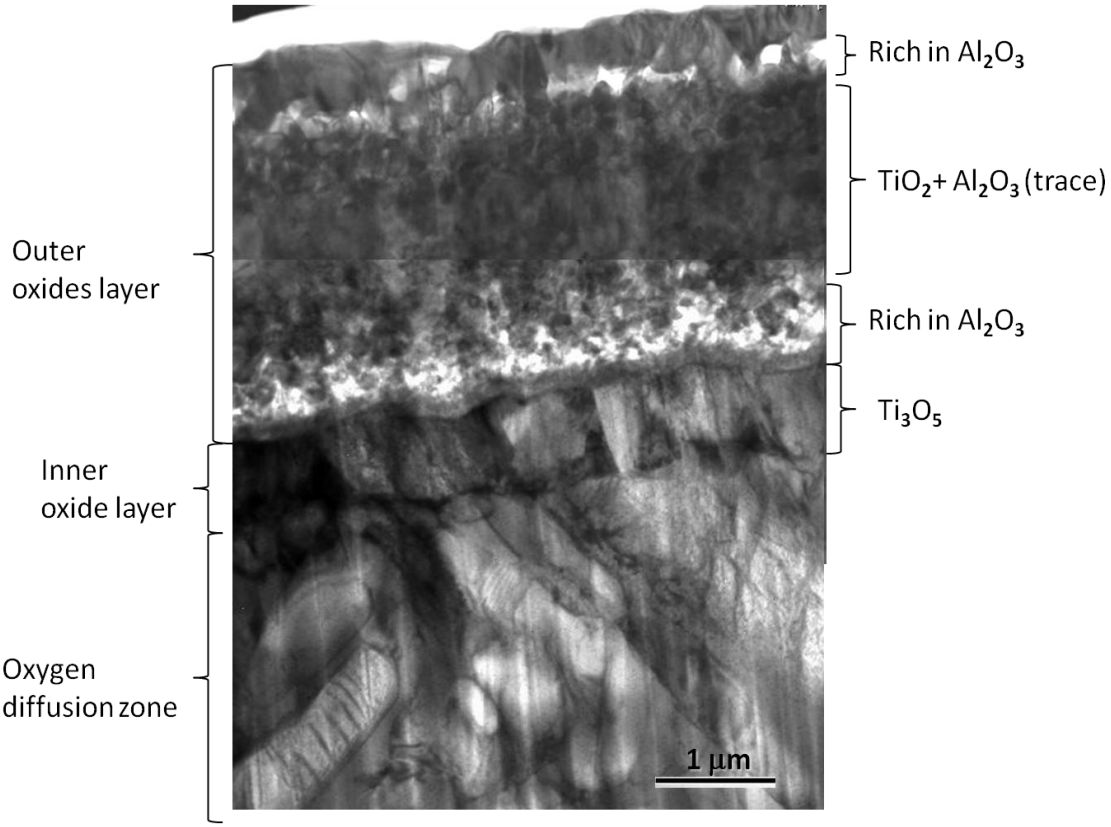

Figure 4.3-24: Cross-section TEM microstructure of the oxide layers and ODZ in sample STA500_8

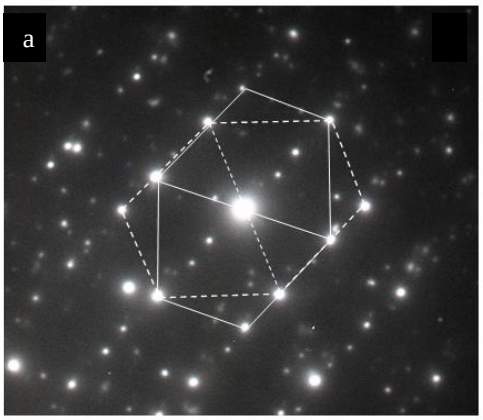

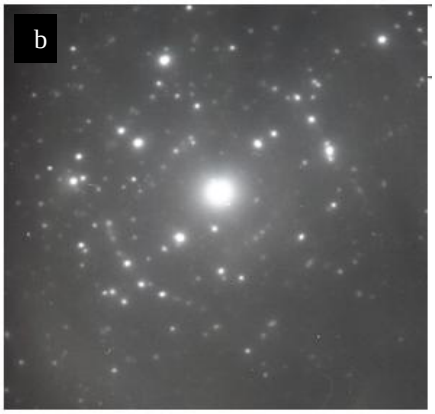

R, mm	d=Lλ/R, nm	HKL Ref(42-1468)	HKL Ref(10-0414)
13	1.154		002
29	0.517		004
39	0.385		006
43	0.349	012	
46	0.326	TiO_2 (110)	
58	0.259	TiO_2(101)	
60	0.250	104	
65	0.231	110	
72	0.208	113	
75	0.200	202	
86	0.174	024	

Figure 4.3-25: SAD patterns showing two sets of (111) TiO_2 from the middle of the outward oxide layer (a) and Al_2O_3 rings from bottom of the outward layer (b) (layers shown in Fig. 4.3-24)

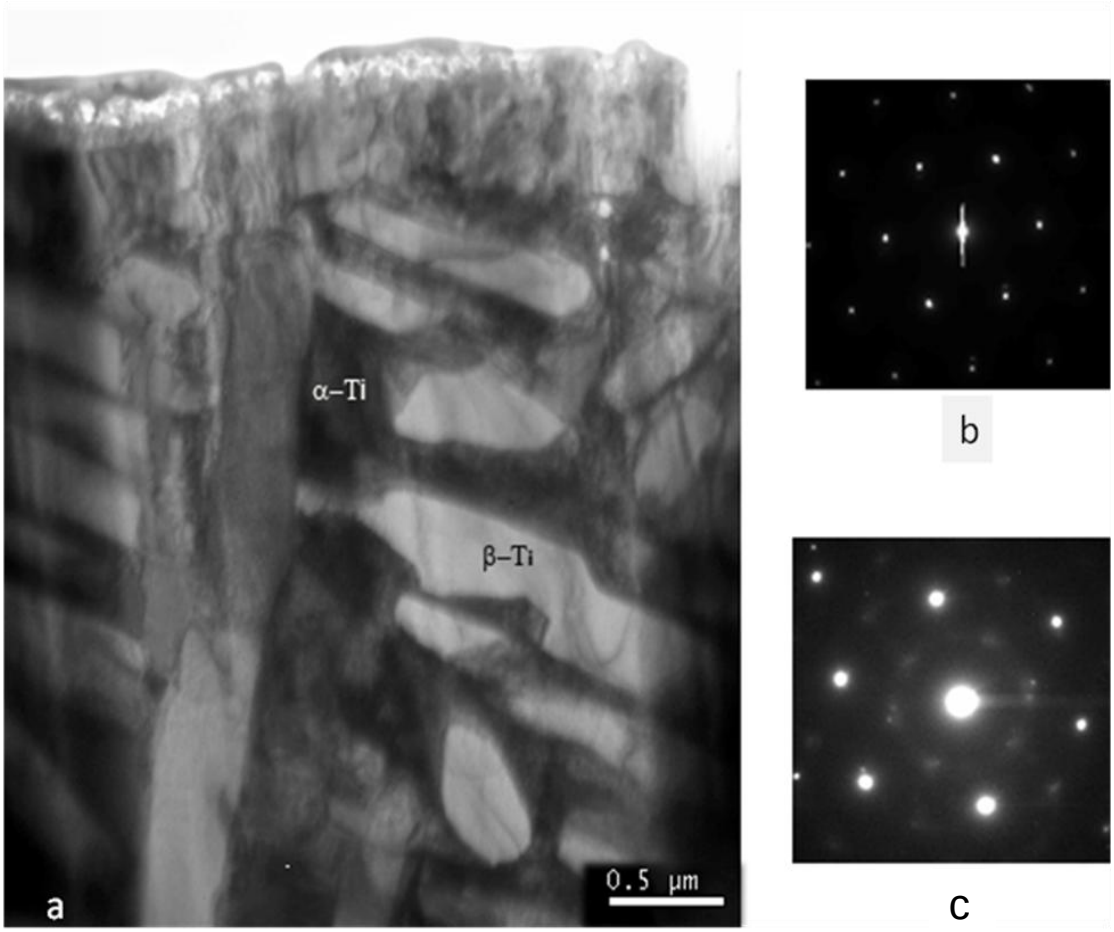

Figure 4.3-26: Cross-section TEM microstructure of diffusion layer showing clear Al_2O_3 particles near surface of the oxide layer (a); SAD patterns showing (001) hcp-Ti (b) and (012) bcc-Ti (c) from the areas as indicated in (a)

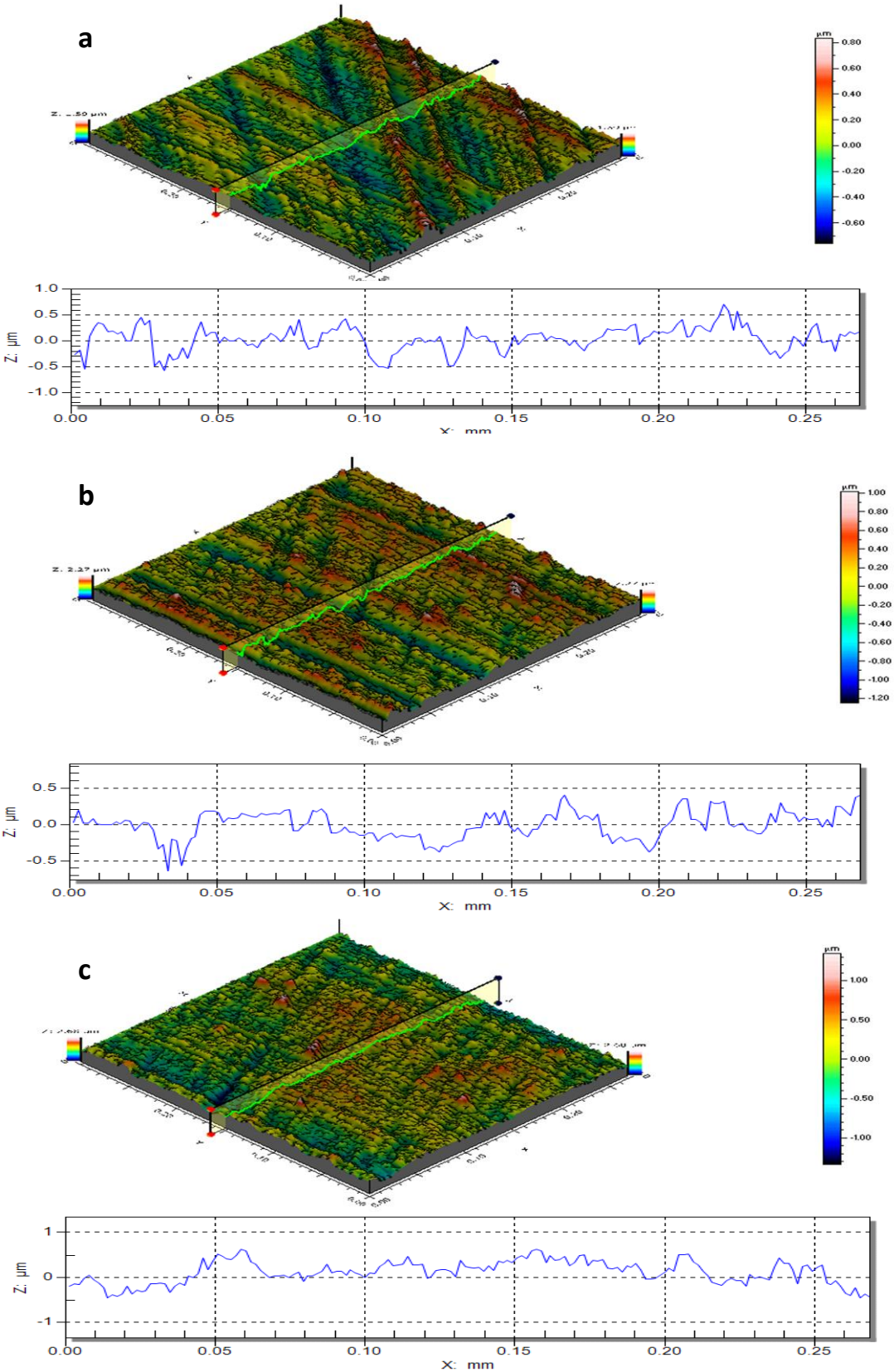
a
µm
0.80
0.60
0.40
0.20
0.00
-0.20
-0.40
-0.60
1.0
0.5
0.0
-0.5
-1.0
Z: µm
0.00
0.05
0.10
0.15
0.20
0.25
X: mm
b
µm
1.00
0.80
0.60
0.40
0.20
0.00
-0.20
-0.40
-0.60
-0.80
-1.00
-1.20
0.5
0.0
-0.5
Z: µm
0.00
0.05
0.10
0.15
0.20
0.25
X: mm
c
µm
1.00
0.50
0.00
-0.50
-1.00
1
0
-1
Z: µm
0.00
0.05
0.10
0.15
0.20
0.25
X: mm

Figure 4.3-27: 3D profiles showing 0.3 x 0.3 mm sections of the surface of samples AR (a), ST0.5 (b) and STA500_4 (c)

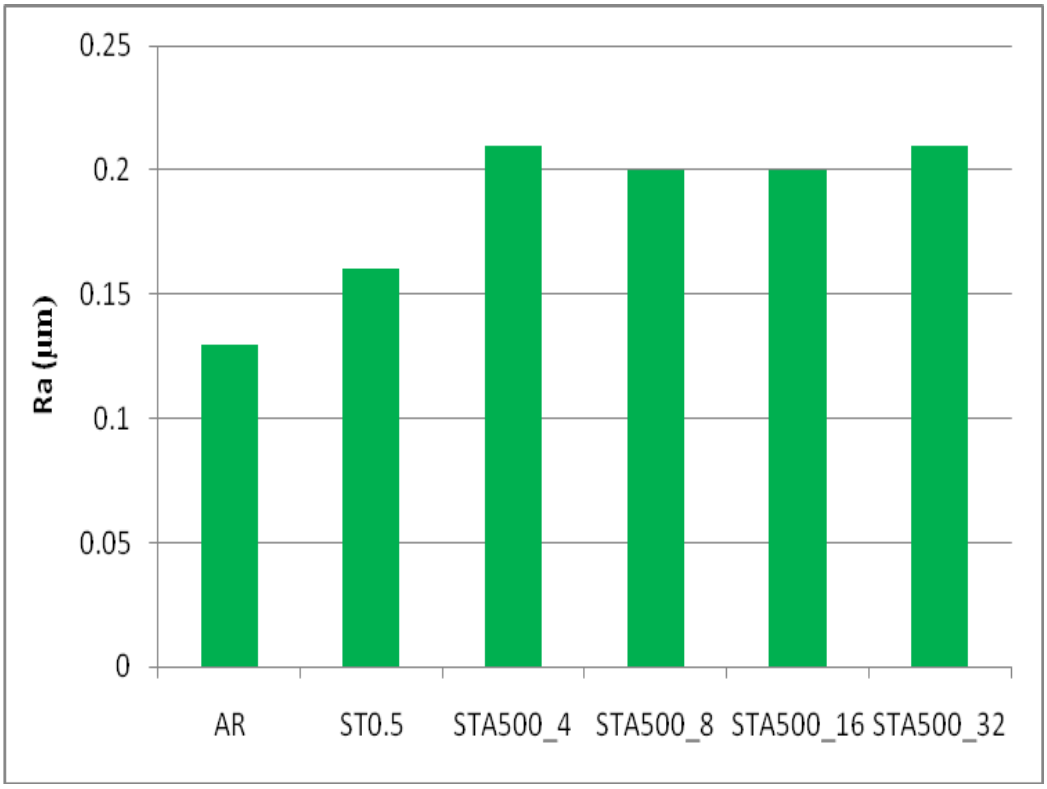

Figure 4.3-28: Average roughness (Ra) from 10 N wear tracks with a tungsten carbide ball on various samples

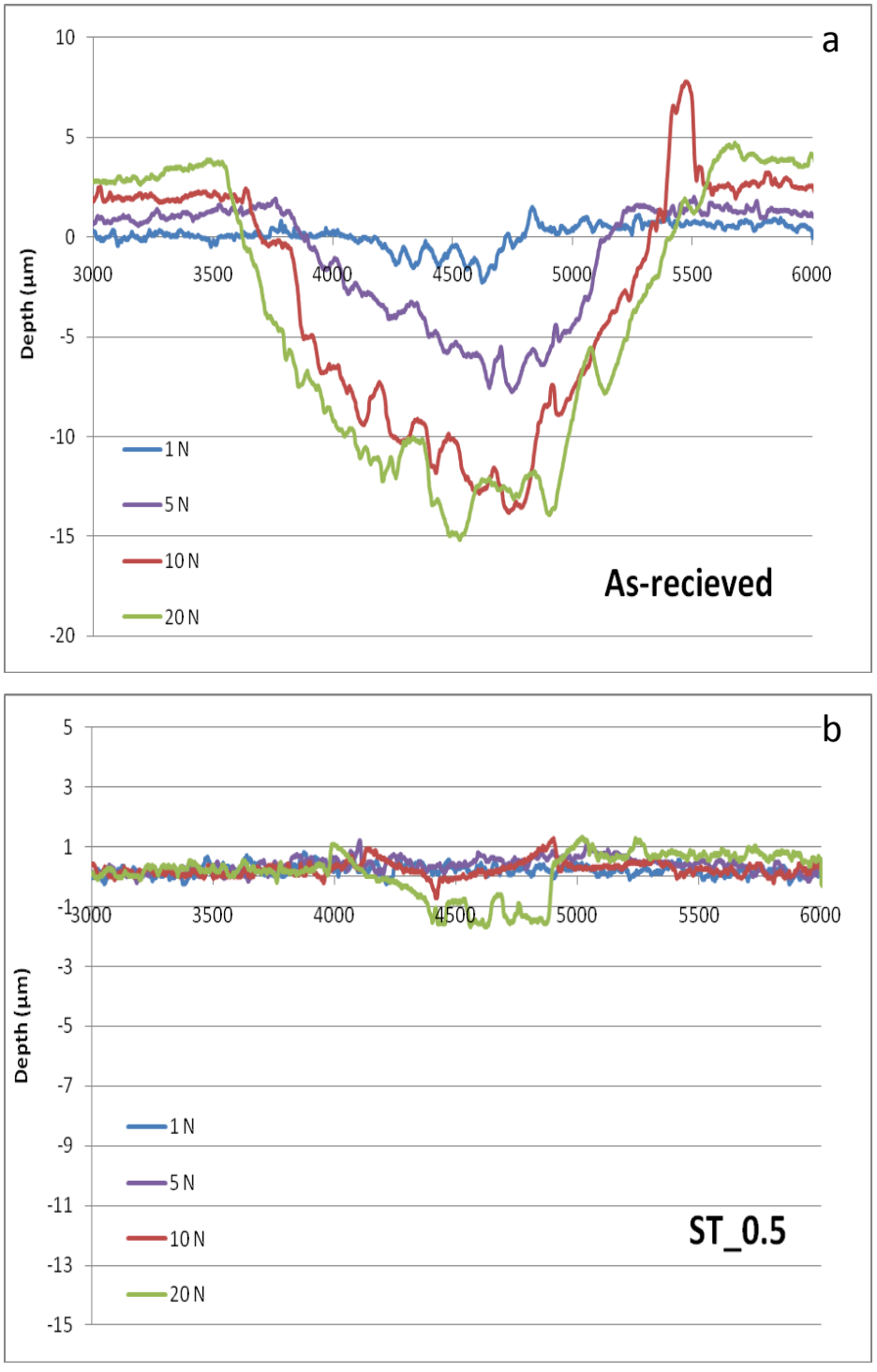

Figure 4.4-1: Wear track profiles of samples AR (a) and ST0.5 (b) under loads of 1, 5, 10 and 20 N from a tungsten carbide ball.

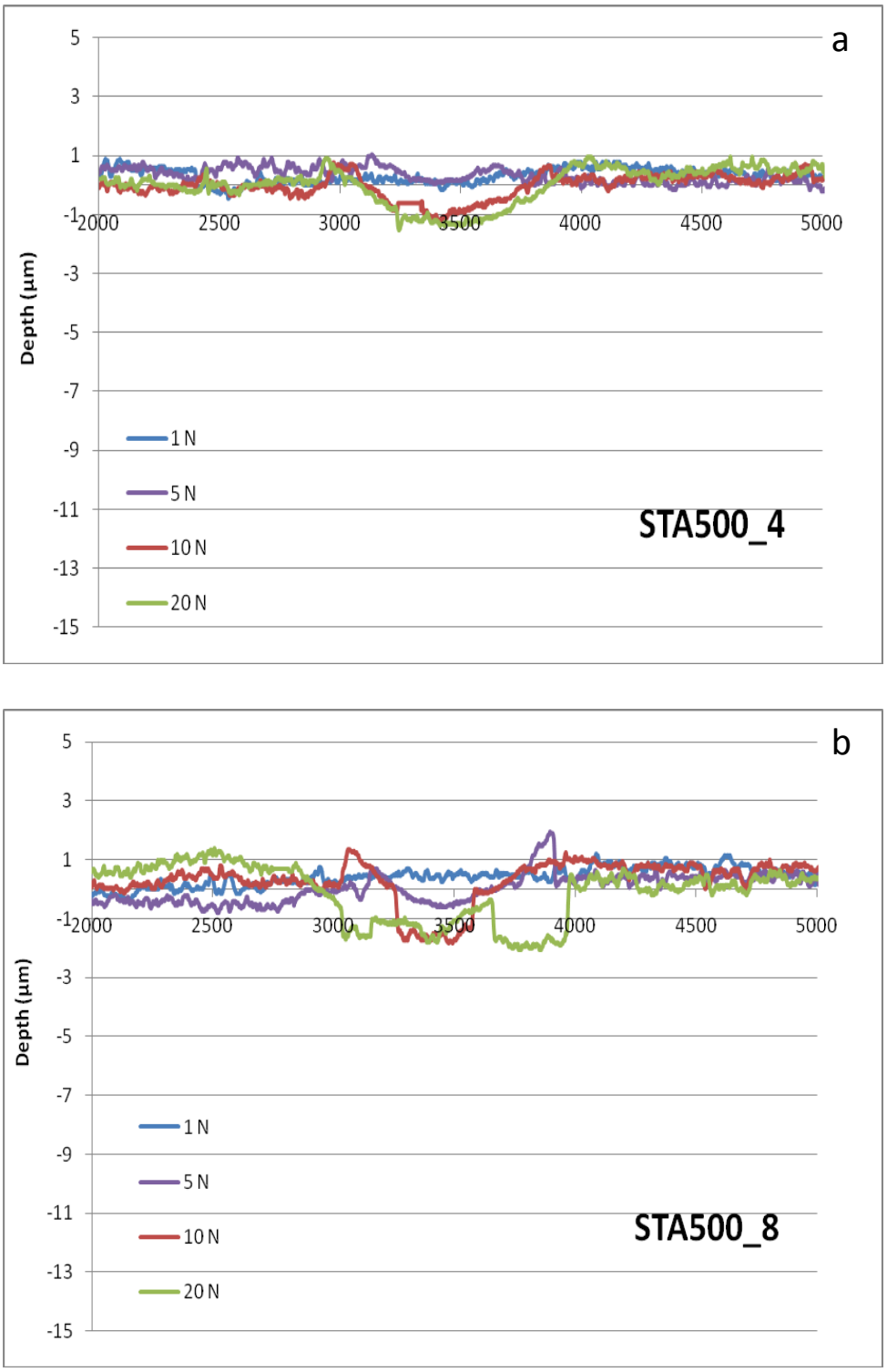

Figure 4.4-2: Wear track profiles of samples STA500_4 (a) and STA500_8 (b) under loads of 1, 5, 10 and 20 N from a tungsten carbide ball

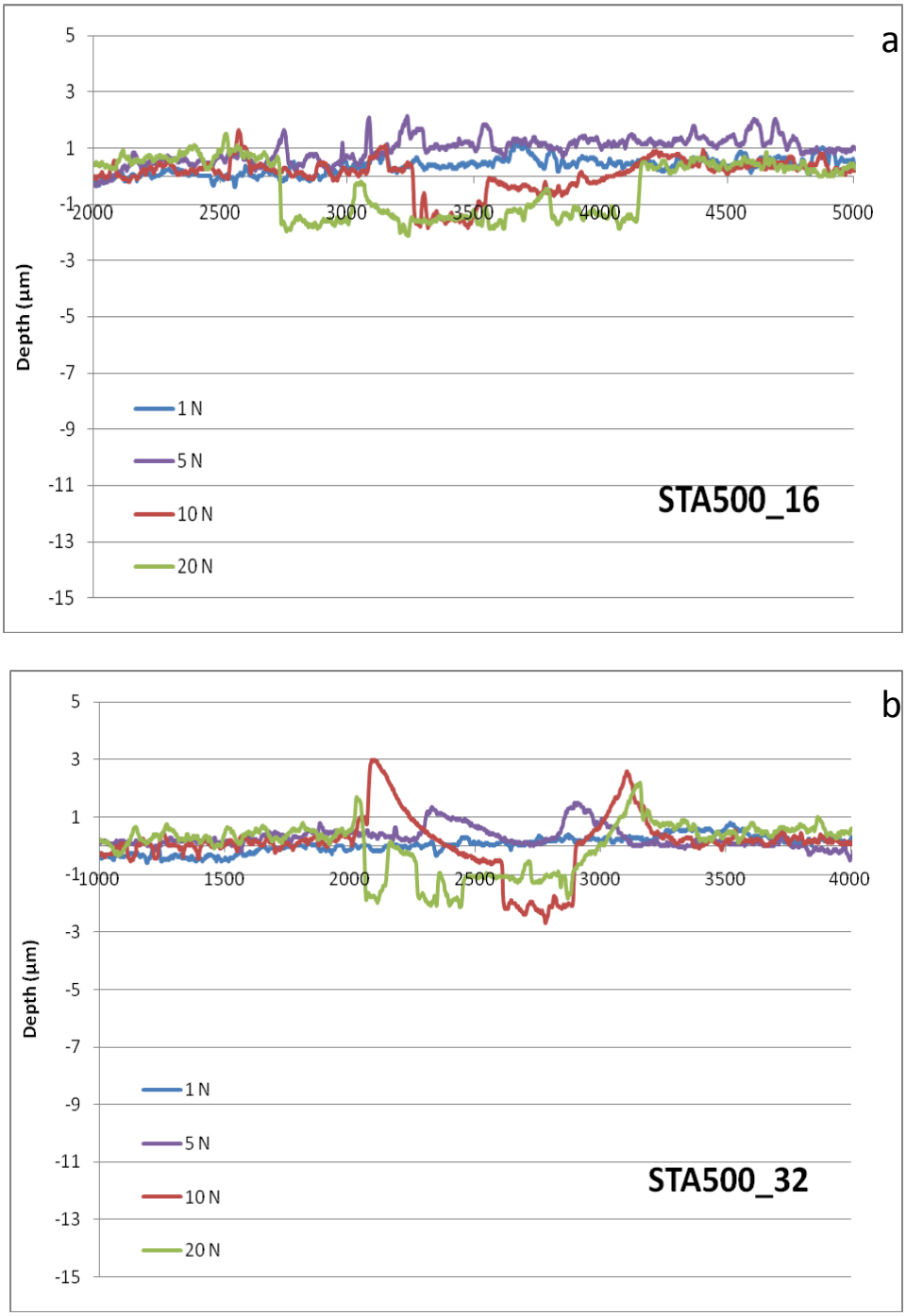

Figure 4.4-3: Wear track profiles of samples STA500_16 (a) and STA500_32 (b) under loads of 1, 5, 10 and 20 N from a tungsten carbide ball

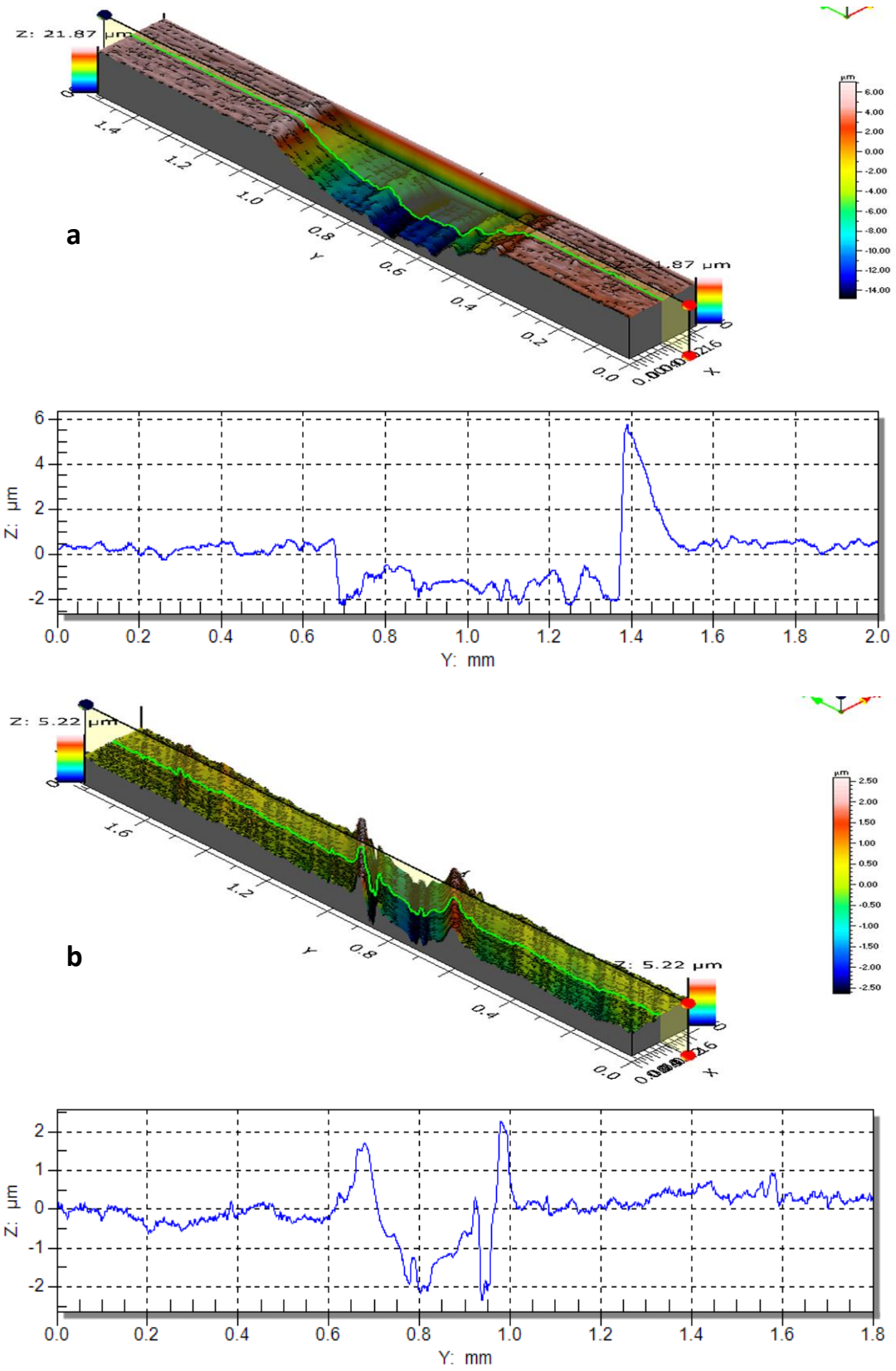

Figure 4.4-4: 3D imaging of wear tracks from a tungsten carbide ball under a 20 N load on samples AR (a) and STA500_4 (b)

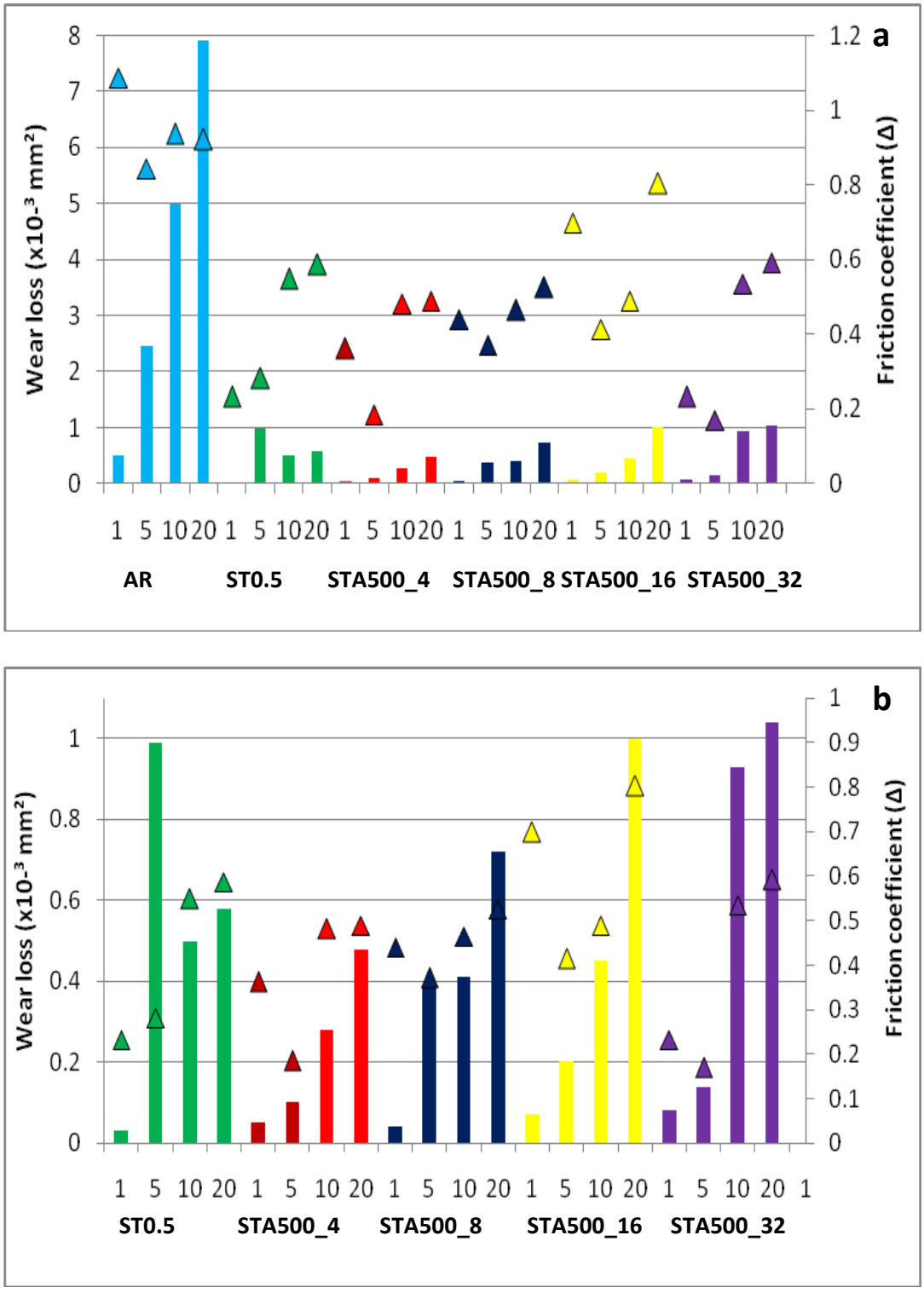

Figure 4.4-5: Wear loss (under 1,5,10,20N loads) calculated from 2D profiles and maximum friction coefficients recorded from each wear test carried out with tungsten carbide balls. Graph b gives same date but excluding as-received results.

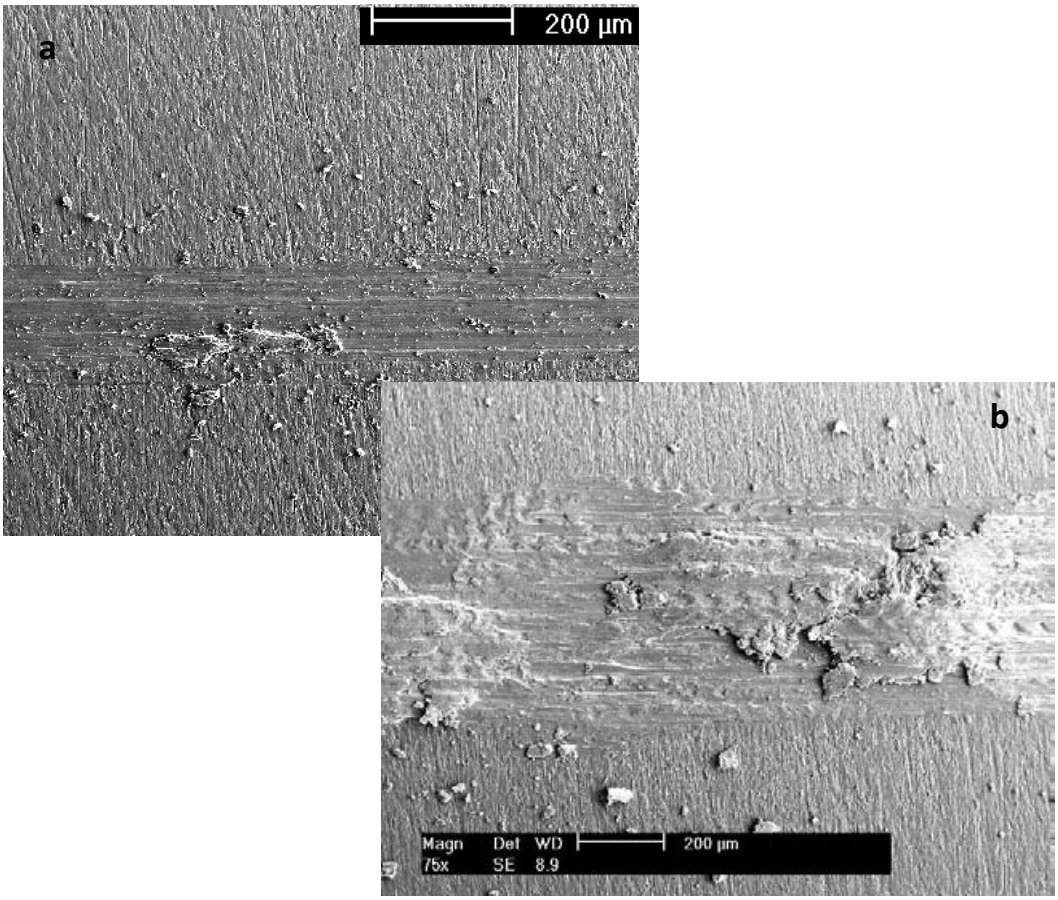

Figure 4.4-6: Wear track on AR sample from a tungsten carbide ball under 1 N (a) and a 10 N (b) load showing the material removal and adhesive wear marks

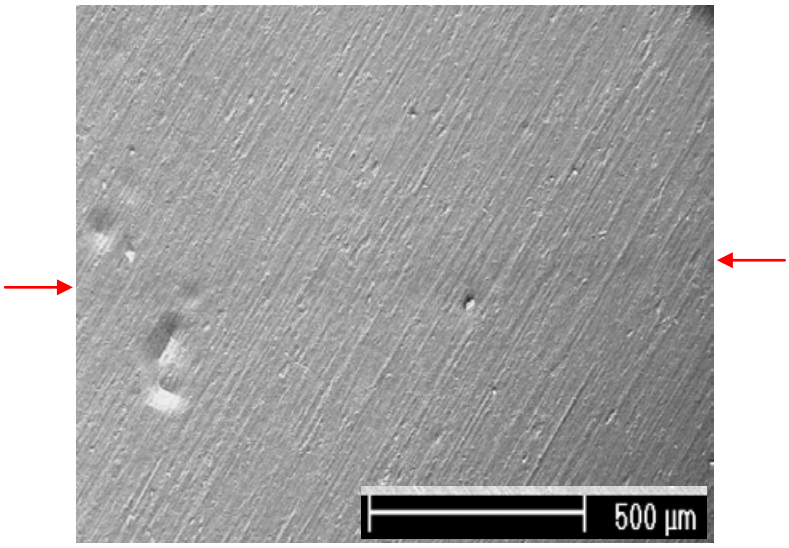

Figure 4.4-7: Wear track on STA500_8 sample from a tungsten carbide ball under 1 N load. Arrows mark the faint track caused by the test.

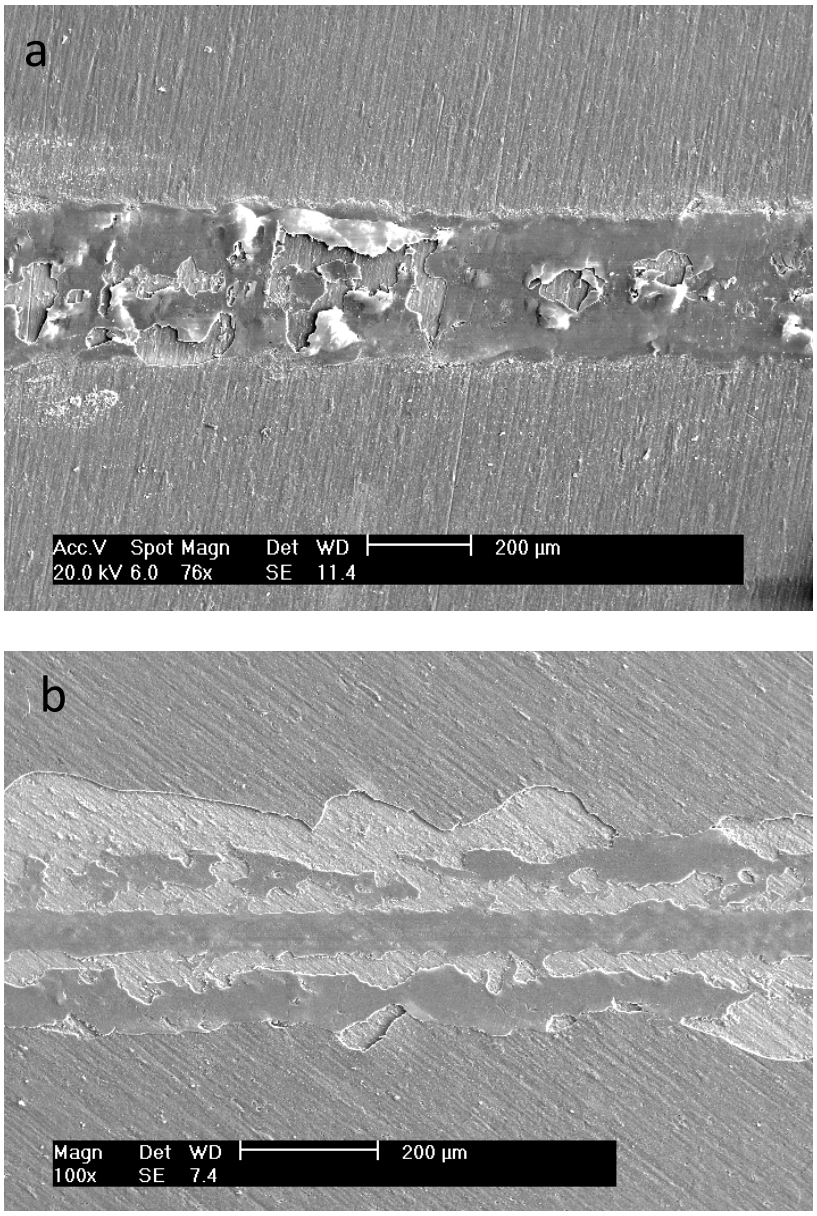

Figure 4.4-8: Wear tracks from a tungsten carbide ball under a 20 N load on STA500_4(a) and on STA500_32 (b)

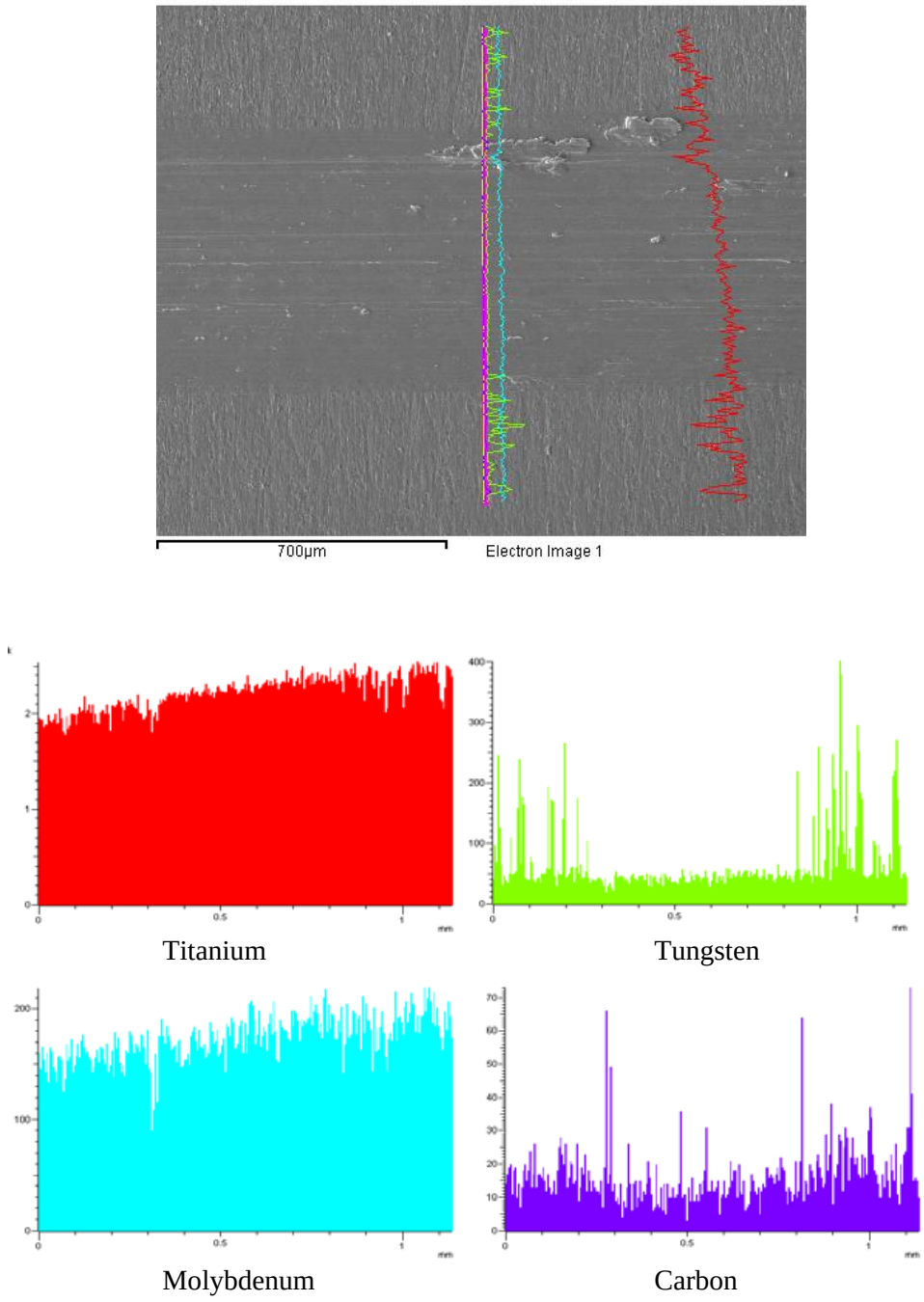

Figure 4.4-9: EDX line scans across the wear track of as-received material under 10N load with a tungsten carbide ball counterpart

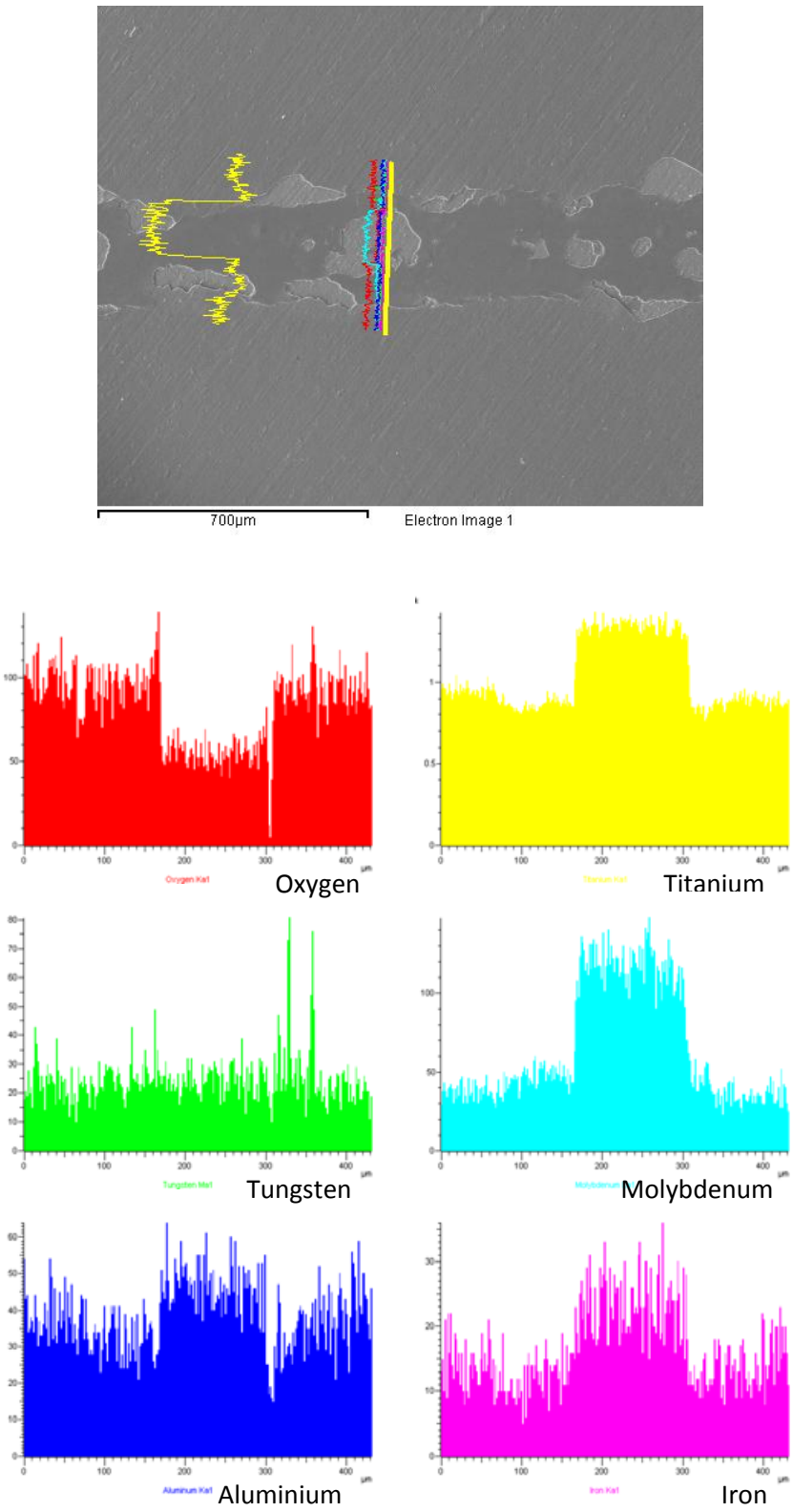

Figure 4.4-10: EDX line scans across a wear track on STA500_8 under 10N load with a tungsten carbide ball counterpart

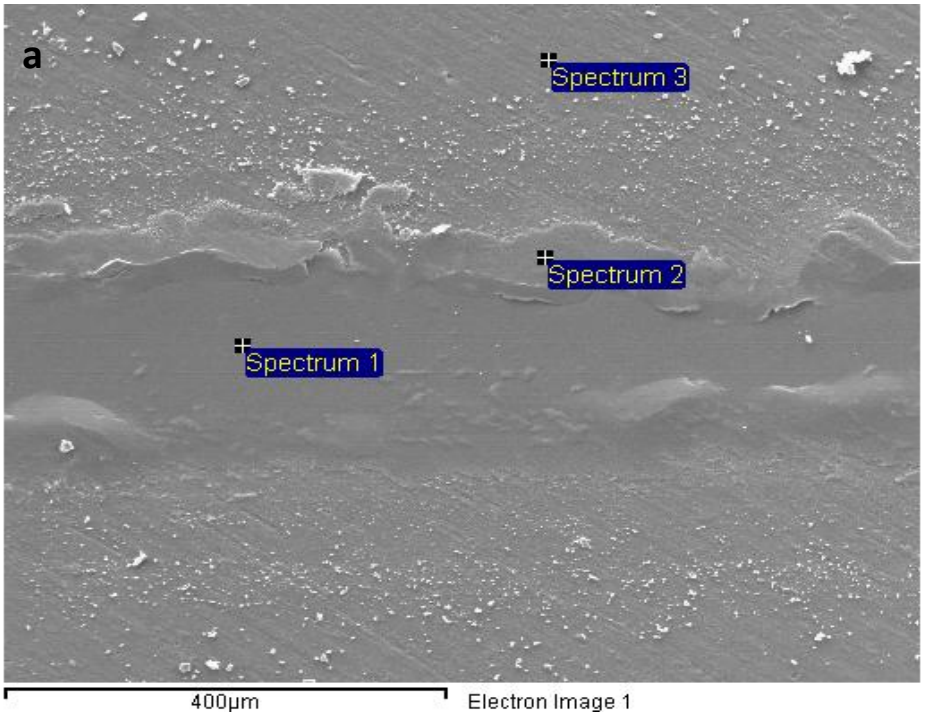

b

Spectrum	Ti	O	Mo	Fe	Al
1	54.04	41.95	2.29	0.65	1.07
2	56.87	40.29	1.37	0.49	0.98
3	57.40	39.60	1.28	0.68	1.04

Figure 4.4-11: SEM image of a wear track on sample STA500_4 (a) and EDX element composition from 3 spectrum points (b) (wear conditions: 5 N loads, a tungsten carbide ball counterpart, dry environment)

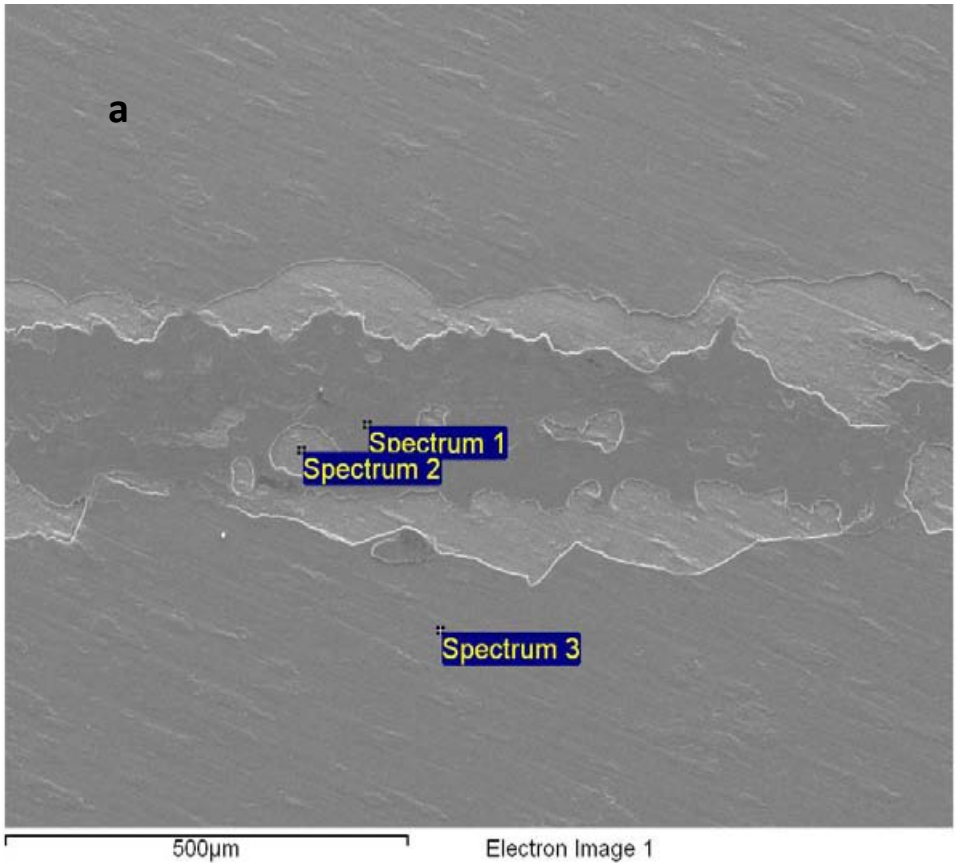

b

Spectrum	Ti	O	Mo	Fe	Al
1	53.80	42.83	2.40	0.79	0.19
2	64.63	26.85	6.12	1.56	0.84
3	53.62	43.24	1.24	1.01	0.89

Figure 4.4-12: SEM image of a wear track on sample STA500_16 (a) and EDX element composition from 3 spectrum points (b) (wear conditions: 5 N loads, a tungsten carbide ball counterpart, dry environment)

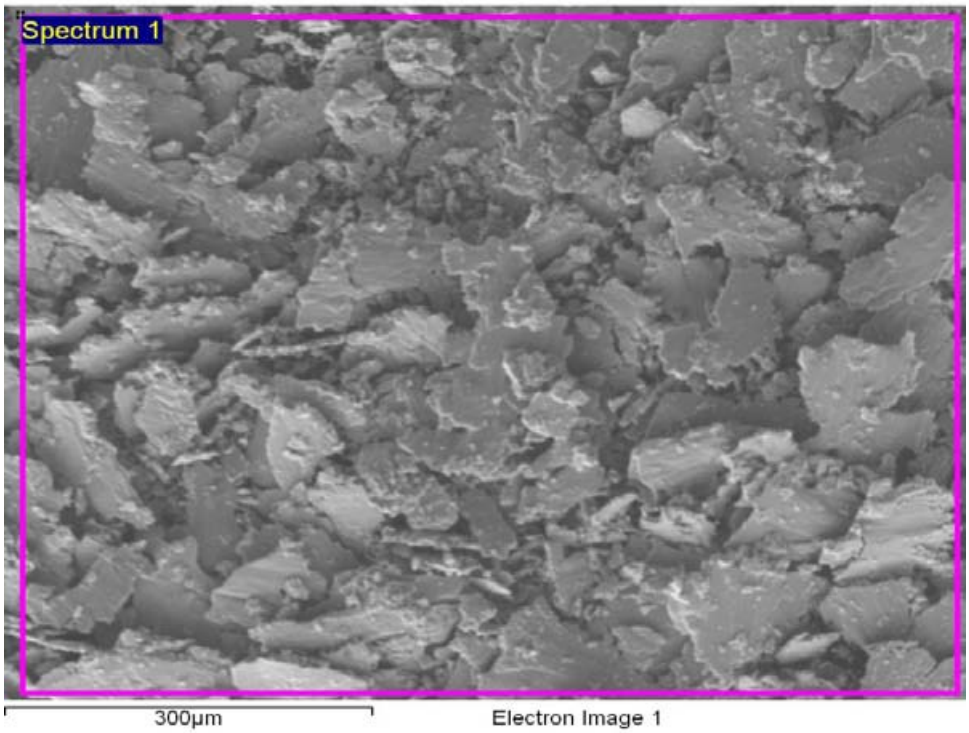

Figure 4.4-13: SEM image of oxide wear debris taken from the surface of STA500_16 after a sliding wear test of 500 cycles (10m sliding distance) under a 20 N load using a tungsten carbide ball.

a

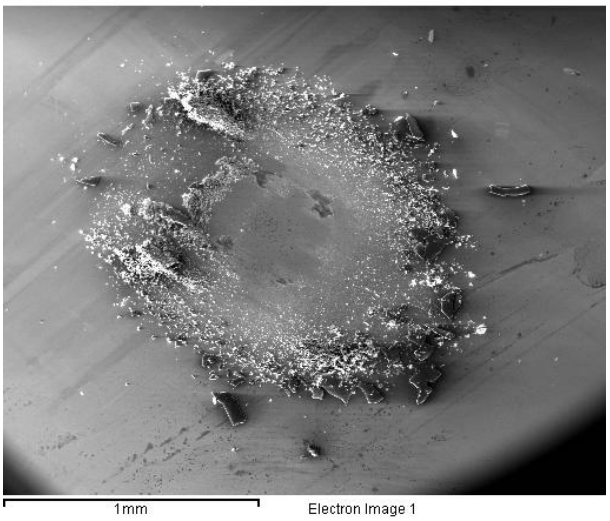

b

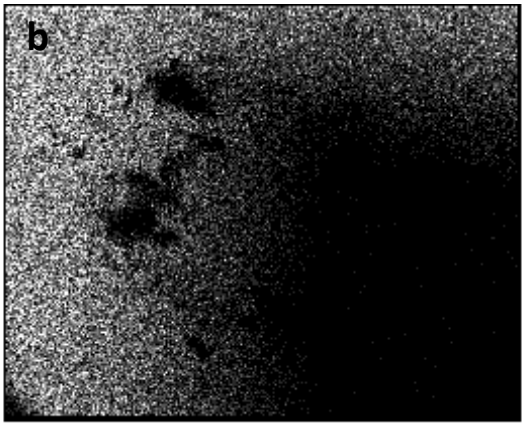
W Ma1

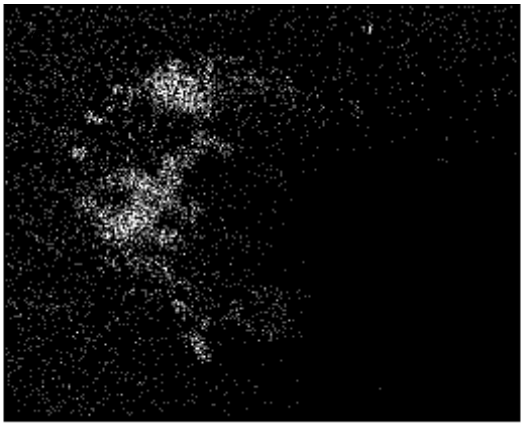
Ti Ka1

d

Element	Weight %	Atomic %
W	85.68	34.37
C	7.27	44.55
Ti	3.75	5.77
O	3.32	15.31

Figure 4.4-14: EDX examination of tungsten carbide ball after wear test on STA500_16 with a 20N load. Shown here is the SEM image (a), the element mapping showing up the location of tungsten (b) and the location of titanium (c), and the quantitative element count (d).

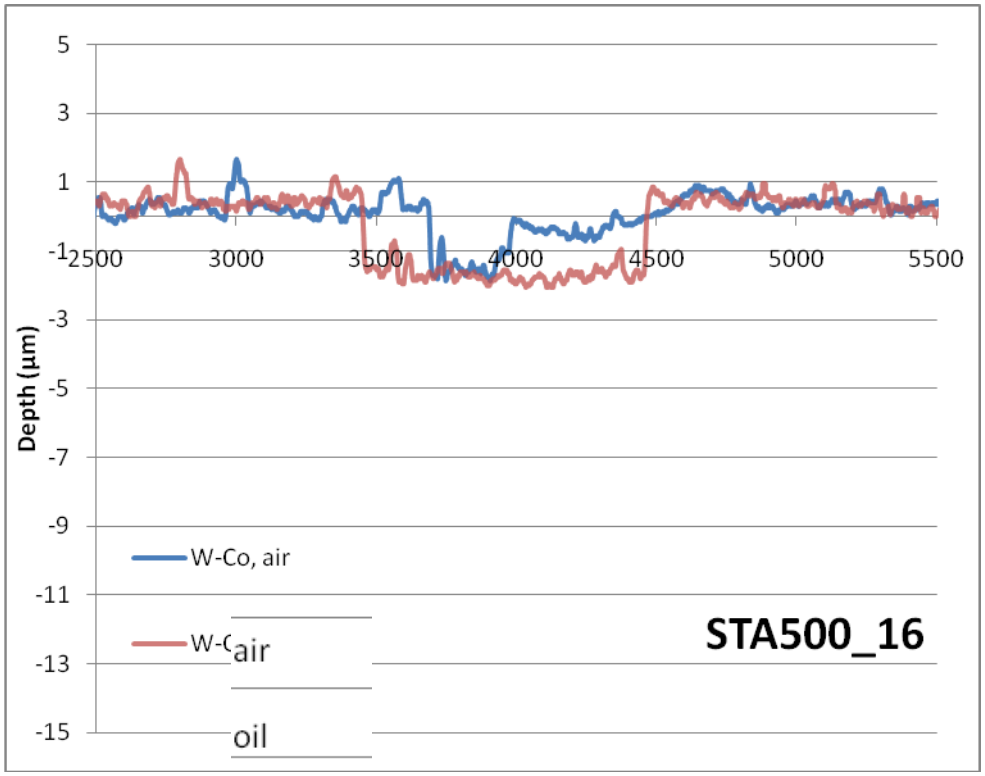

Figure 4.4-15: Wear profiles of sample STA500_16 tested under both dry and lubricated conditions with a 20 N load, WC-Co counterpart.

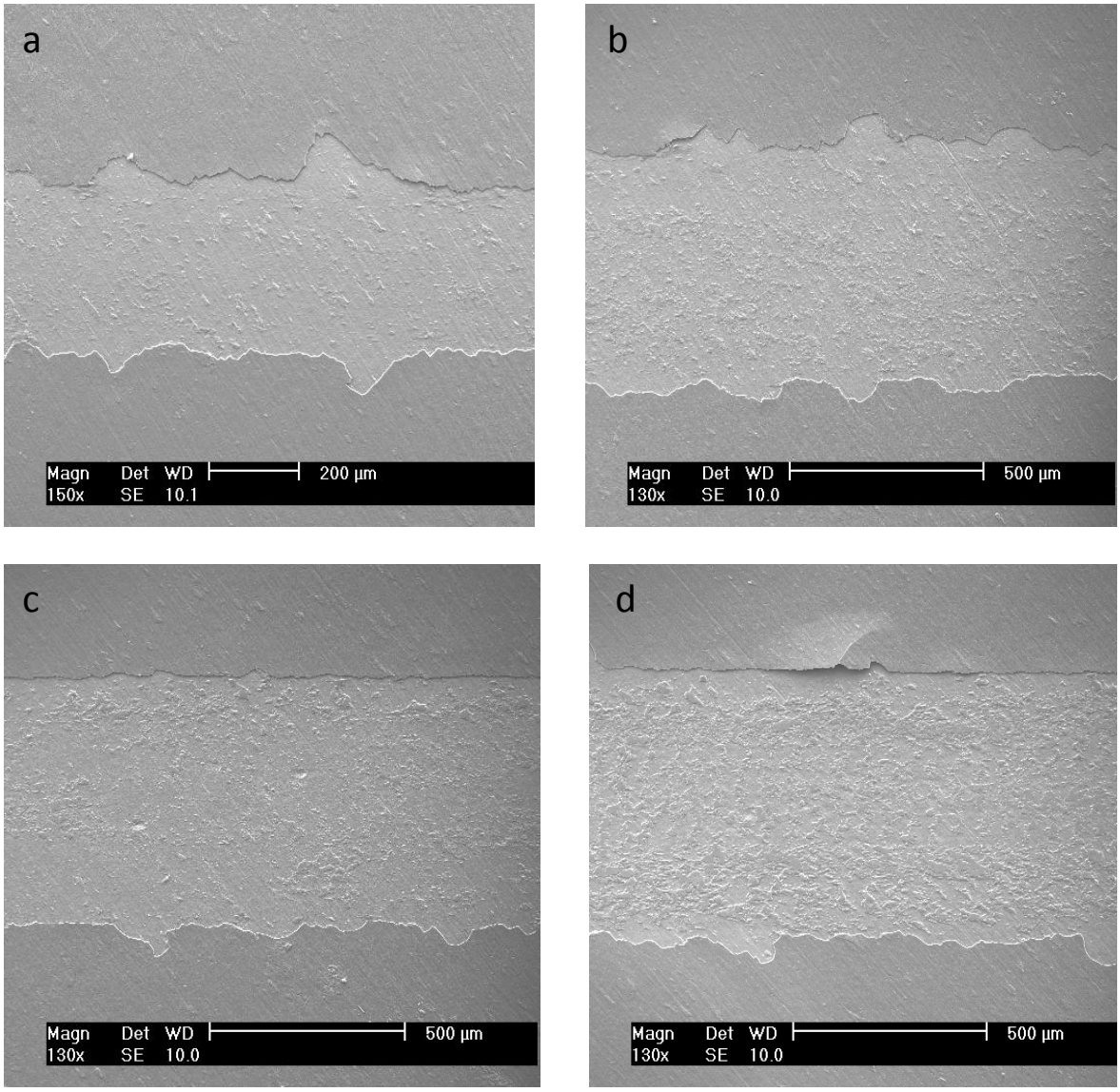

Figure 4.4-16: SEM images of wear tracks on sample STA500_16 from a hardened steel ball counterpart under loads of 1 N (a), 5 N (b), 10 N (c) and 20 N (d)

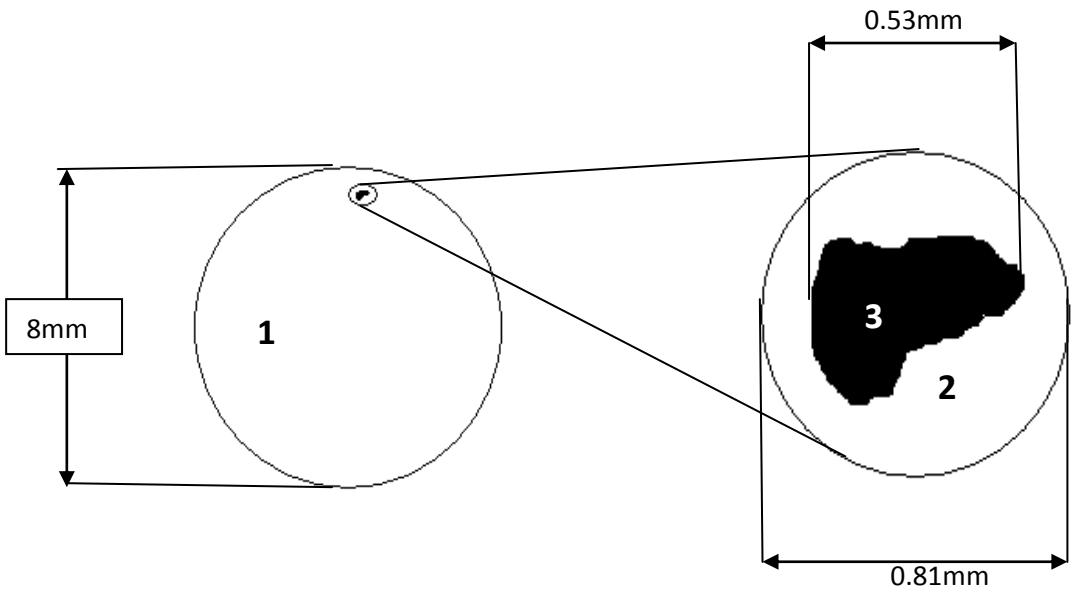

Figure 4.4-17: Schematic of a steel ball after wear testing with a 20N load. The ball (1) showed a flattened area of removed steel (2) that in itself contained wear debris (3).

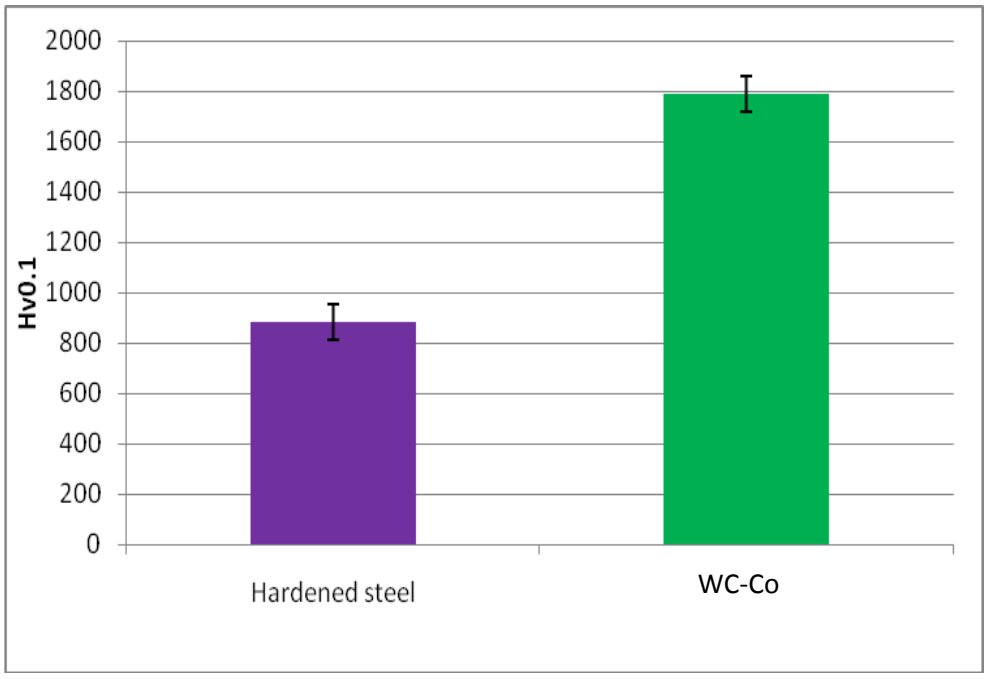

Figure 4.4-18: Vickers hardness (100g load) take from a hardened steel ball and a tungsten carbide ball which were used in the wear tests.

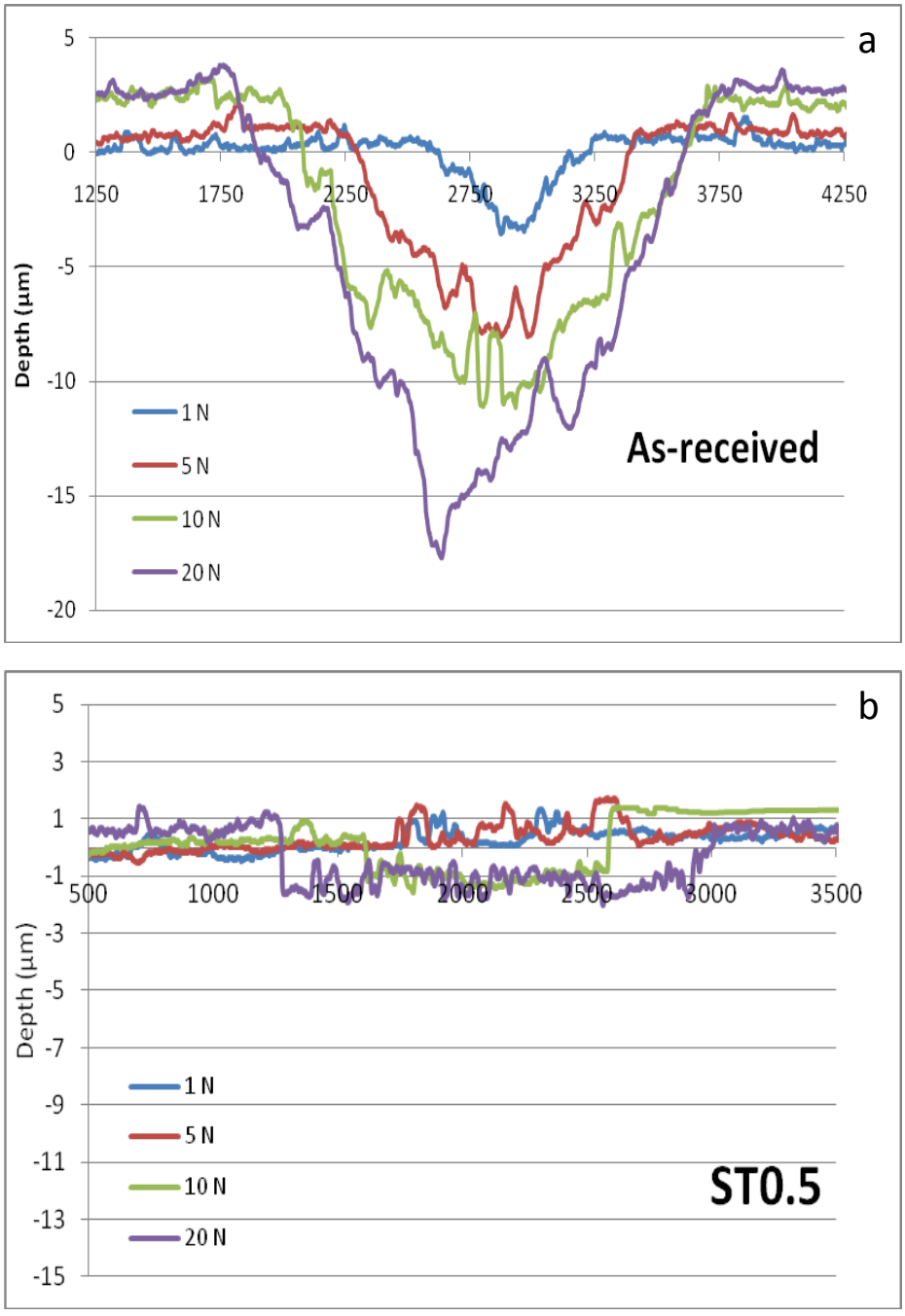

Figure 4.4-19: Wear tracks from applied loads of 1, 5, 10 and 20 N from a hardened steel ball counterpart on samples AR (a) and ST0.5 (b)

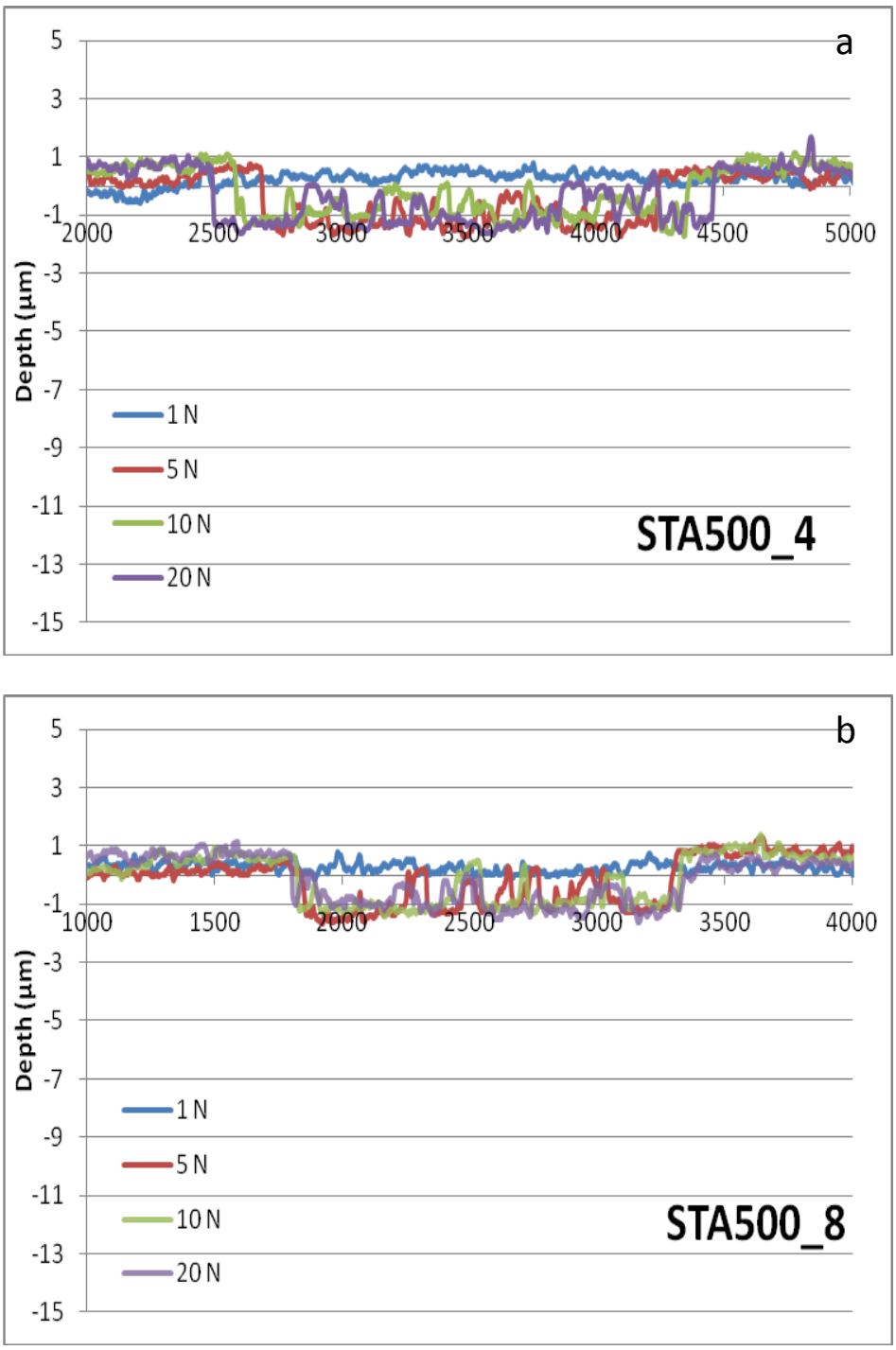

Figure 4.4-20: Wear tracks from applied loads of 1, 5, 10 and 20 N from a hardened steel ball counterpart on samples STA500_4 (a) and STA500_8 (b)

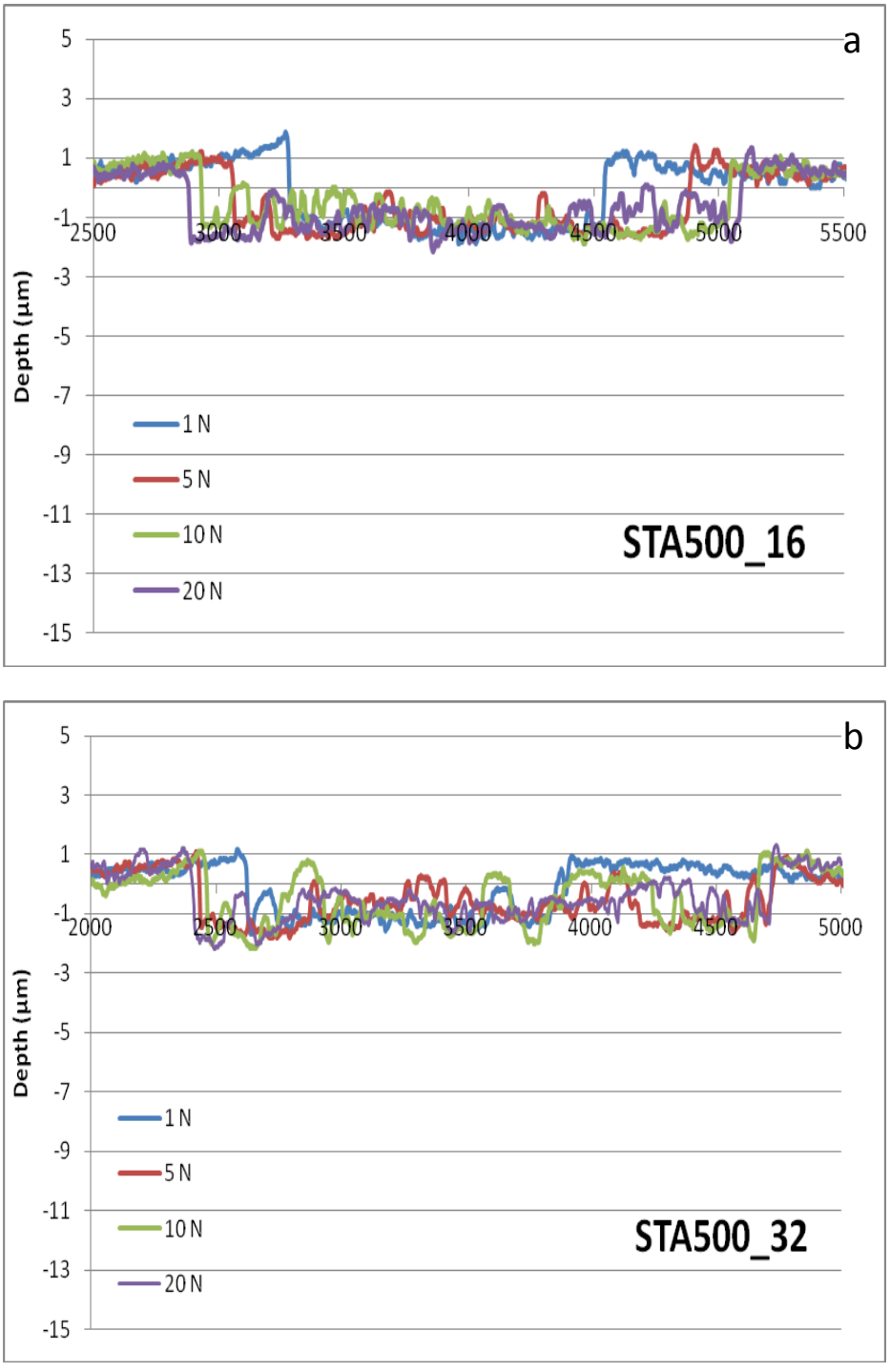

Figure 4.4-21: Wear tracks from applied loads of 1, 5, 10 and 20 N from a hardened steel ball on samples STA500_16 (a) and STA500_32 (b)

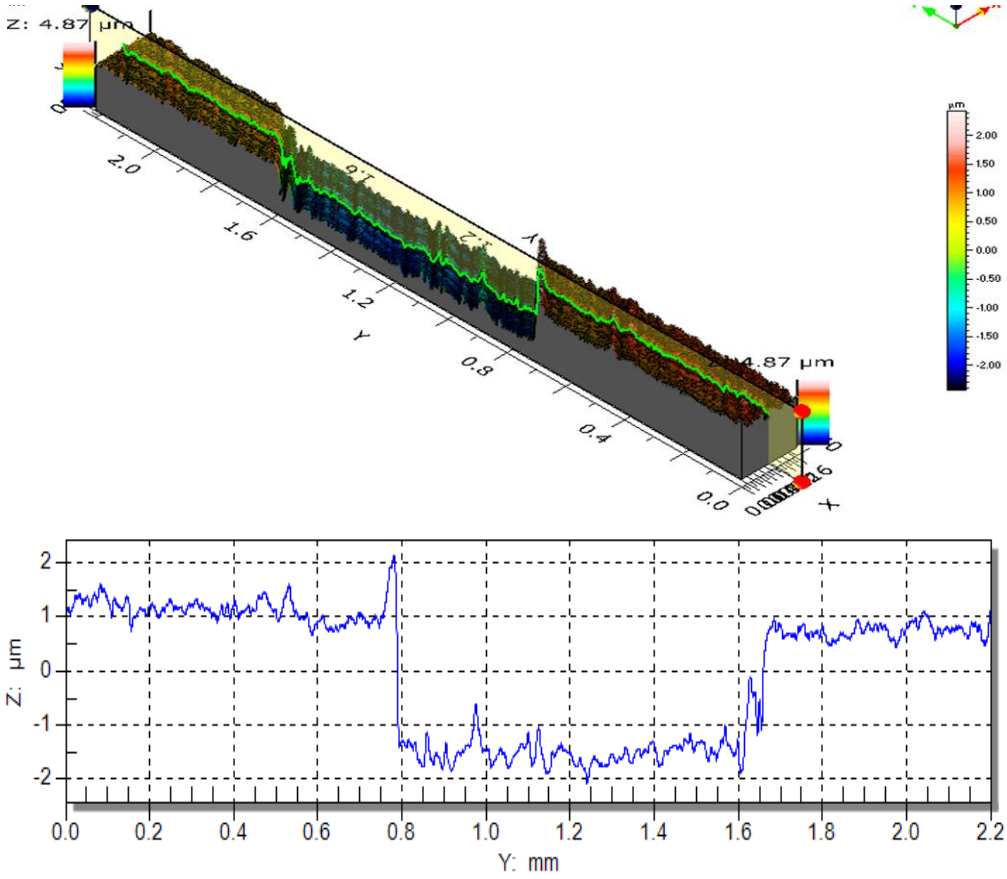

Figure 4.4-22: 3D profile, a) and 2D profile of a 20 N wear track on sample STA500_16, produced with a hardened steel ball counterpart, in air

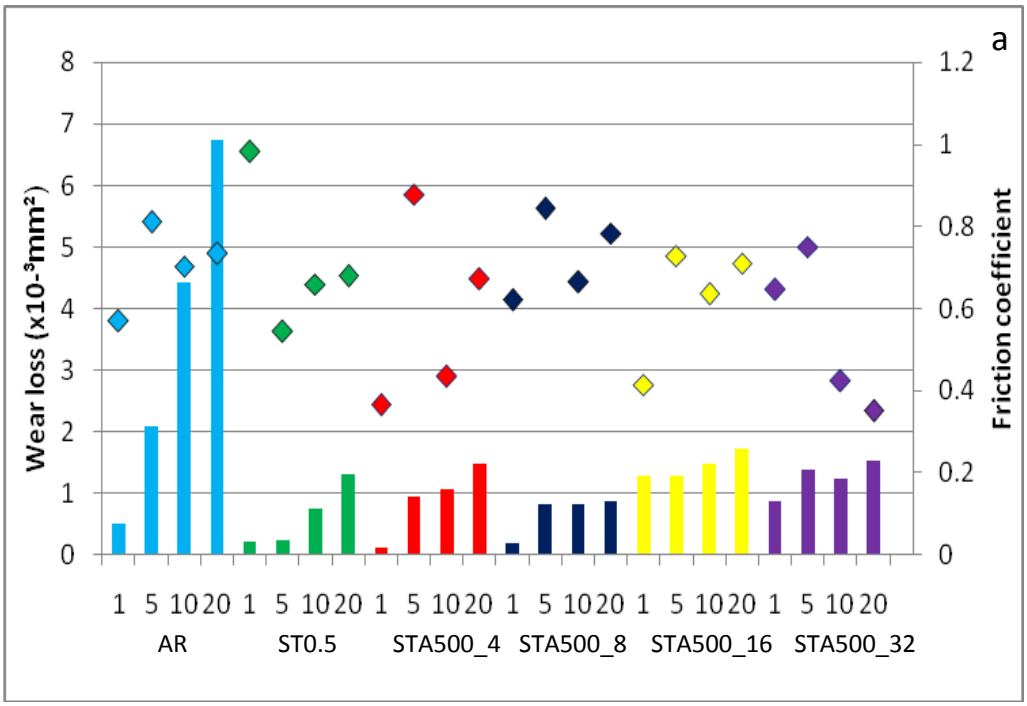

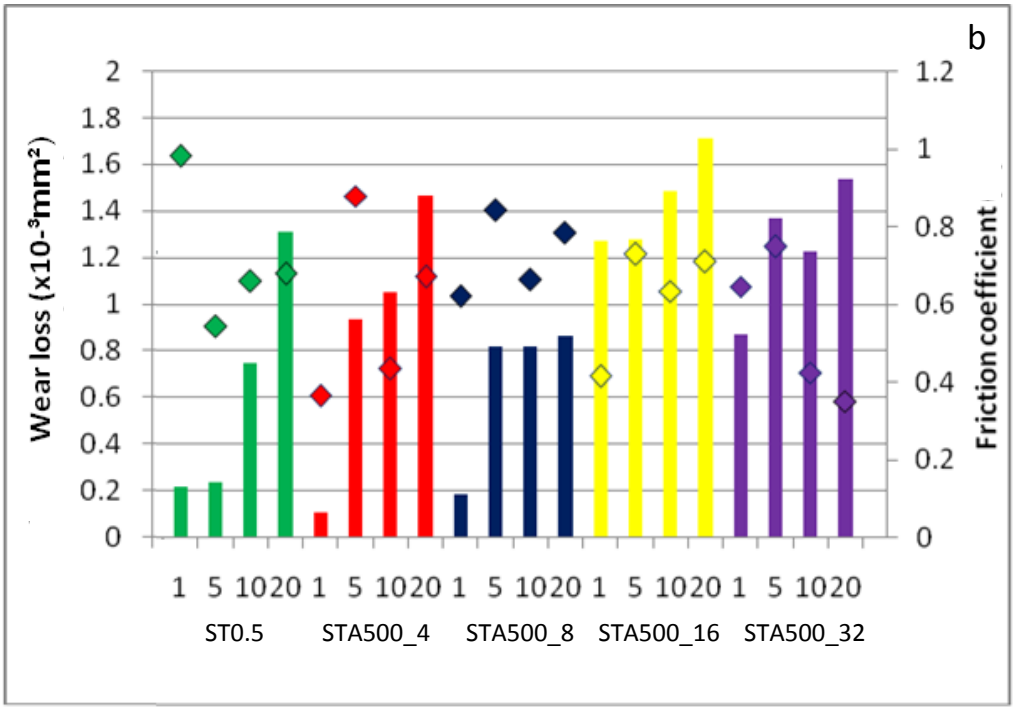

Figure 4.4-23: Wear loss and maximum friction coefficient values for samples with a hardened steel ball counterpart in air compared with AR (a) and with treated samples only (b)

a

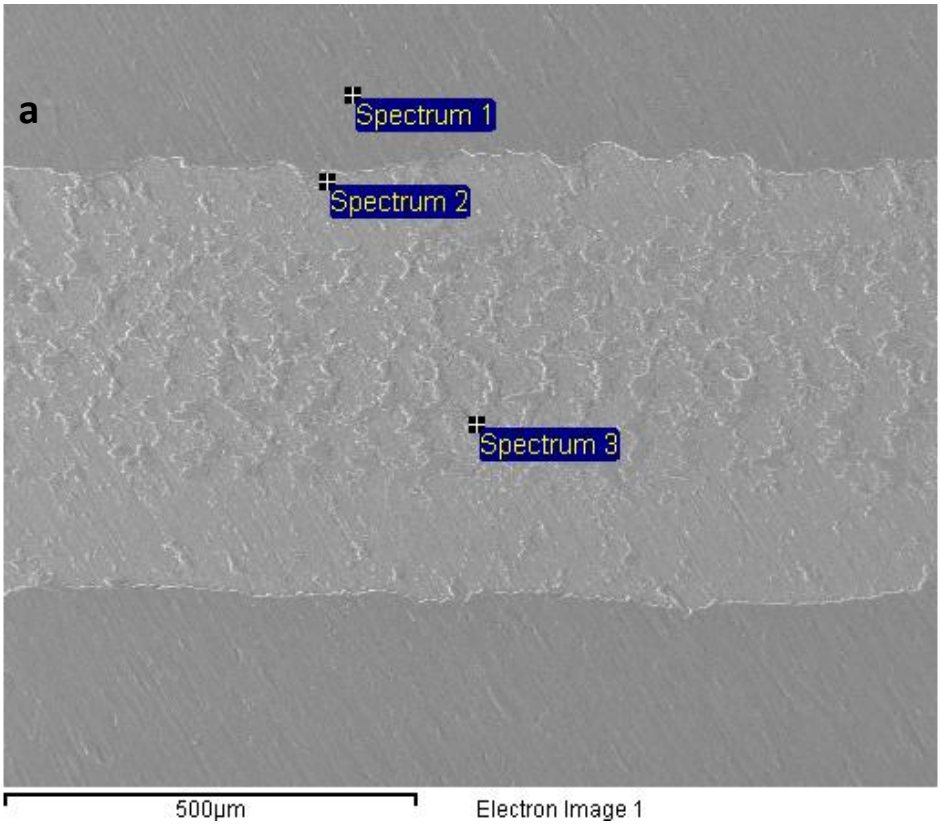

b

Spectrum	Ti	O	Mo	Fe	Al	Cr
1	55.10	41.76	1.52	0.61	0.95	0
2	63.11	28.08	6.47	1.22	1.13	0
3	13.18	41.78	0.81	43.50	0.07	0.66

Figure 4.4-24: EDX analysis (b) on an SEM image (a) of a 10 N wear track from a hardened steel ball counterpart in a dry environment on sample STA500_16.

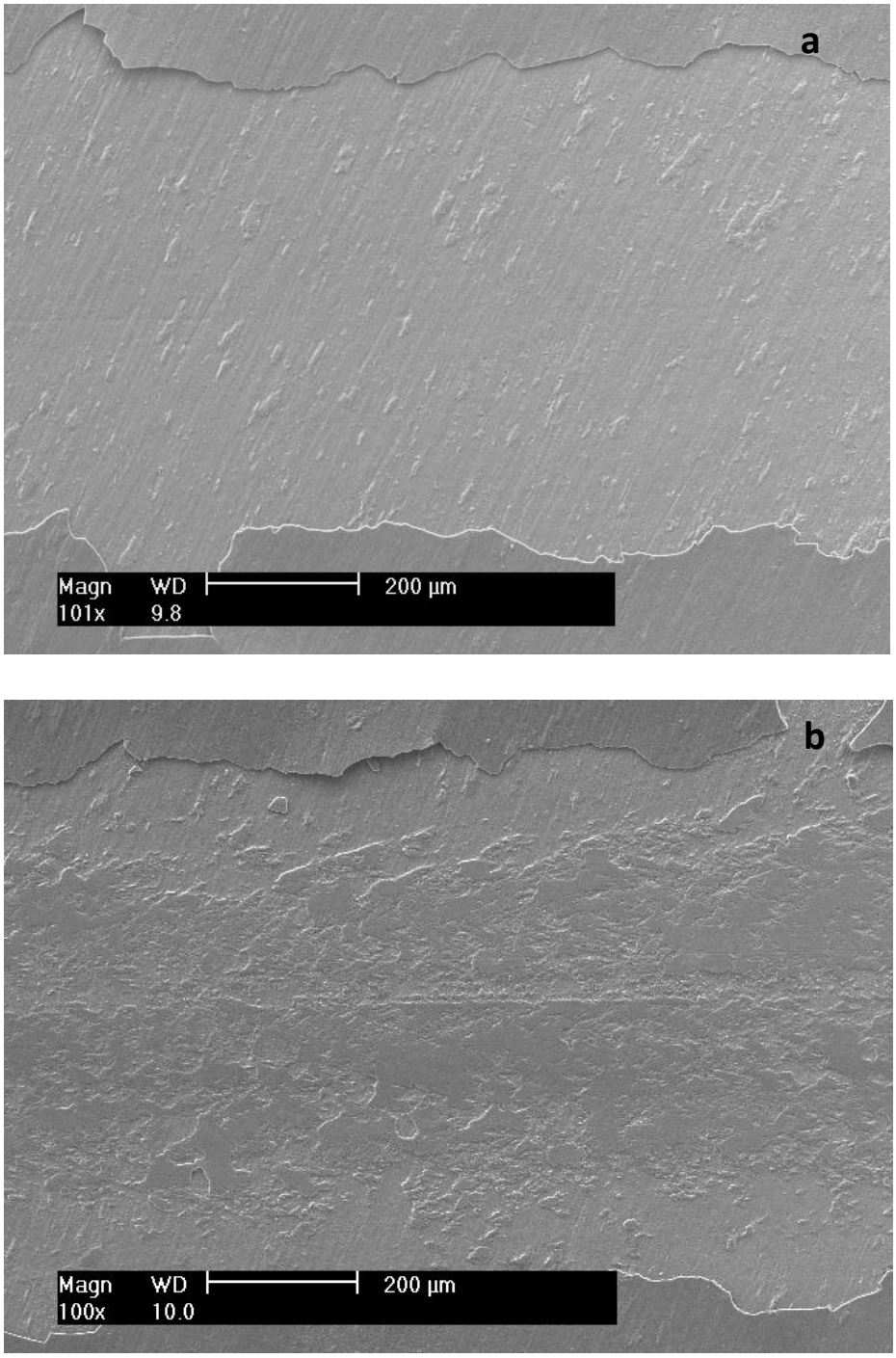

Figure 4.4-25: SEM image of a wear tracks on sample STA500_32 produced with a hardened steel ball counterpart under a 20 N load in an oil lubricated (a) and dry (b) environment

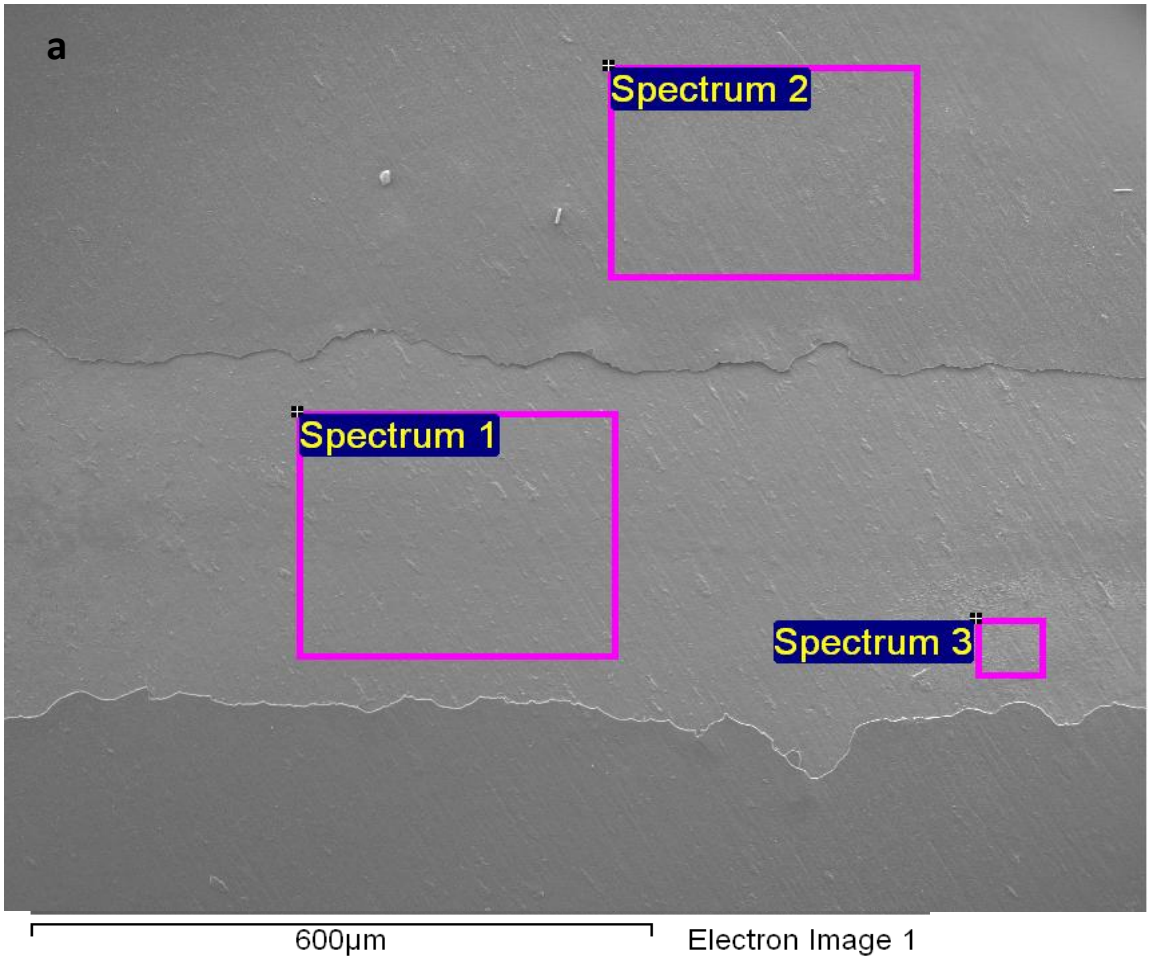

b

Spectrum	Ti	O	Mo	Fe	Al	Cr
1	62.40	30.62	5.33	0.89	0.76	0
2	54.48	42.60	1.20	0.68	1.04	0
3	61.90	29.36	6.16	0.77	0.71	0

Figure 4.4-26: 10 N wear track SEM image from an oil lubricated environment using a hardened steel ball counterpart on STA500_8 (a) and EDX composition analysis of each spectrum (b)

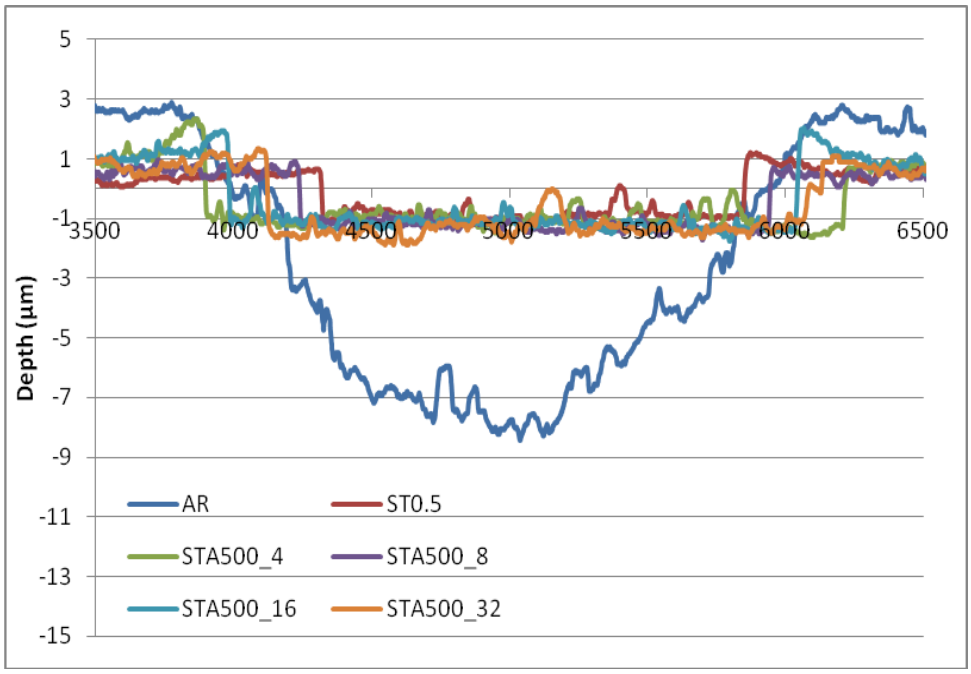

Figure 4.4-27: Wear tracks from all samples under a 20 N load from a hardened steel ball in a lubricated environment

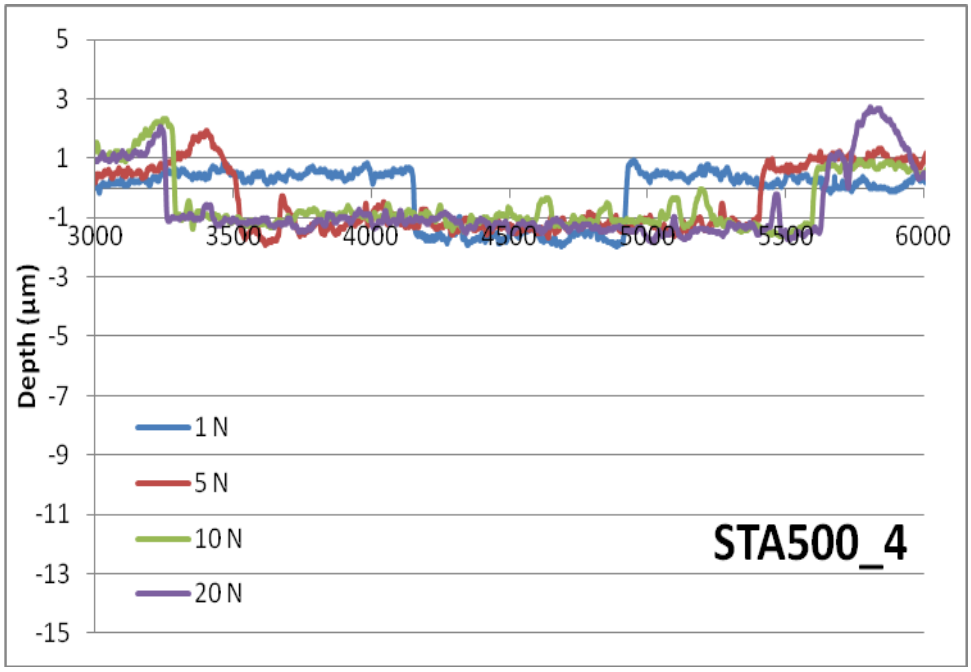

Figure 4.4-28: Wear tracks for loads of 1, 5, 10 and 20 N on STA500_4 from a hardened steel ball in lubricated environment.

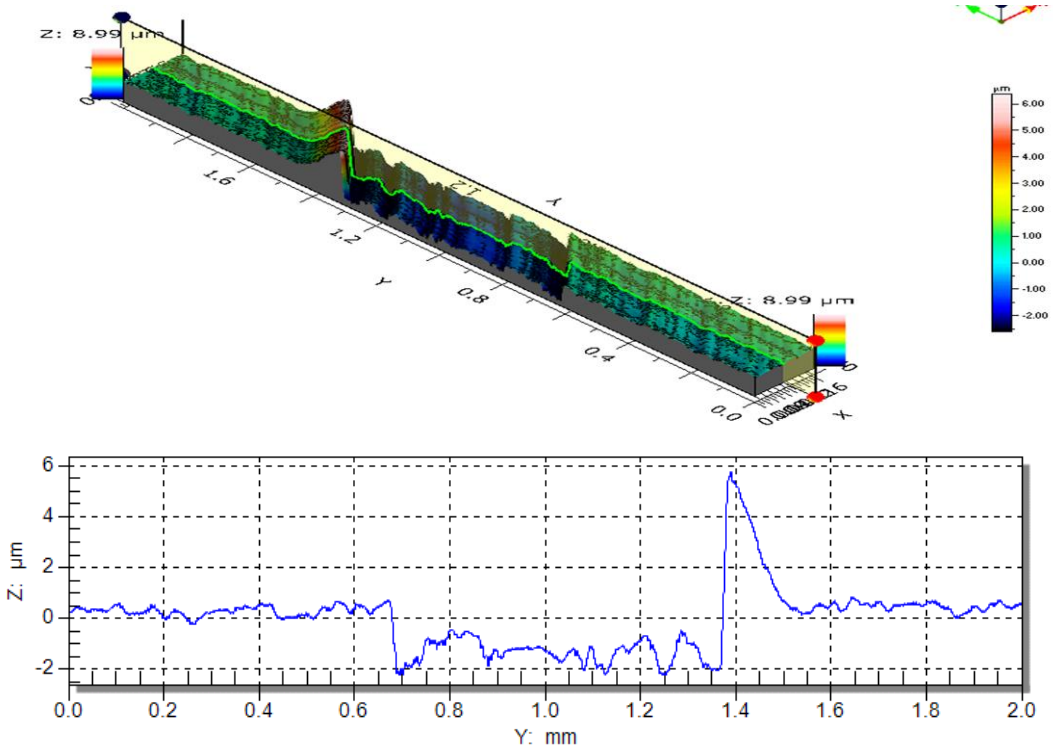

Figure 4.4.29: 3D (a) and 2D (b) profiles of wear track on sample STA500_32 produced with a 20 N load by a steel ball counterpart in an oil lubricated environment

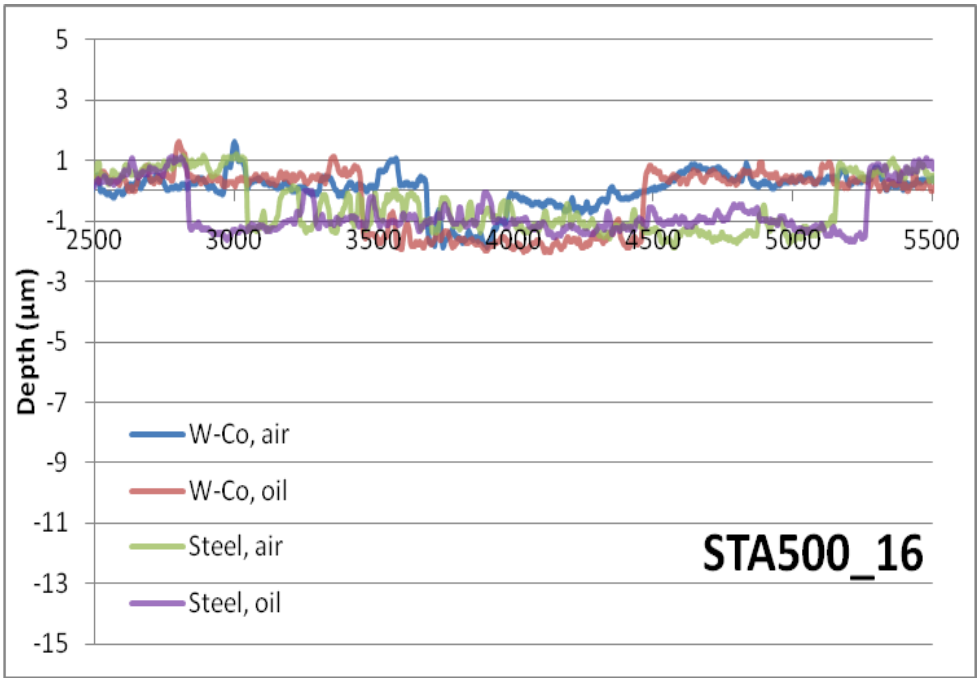

Figure 4.4-30: Wear tracks comparing STA500_16 samples under varying conditions with a 20N load

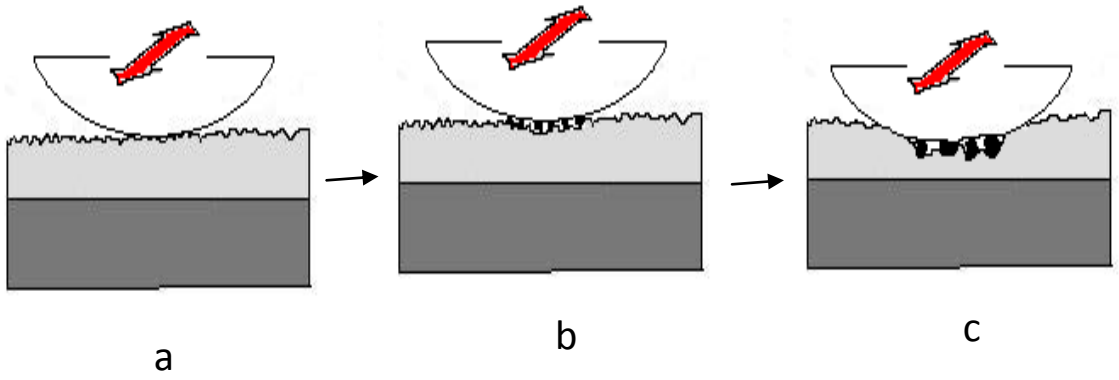

Figure 5.2-1: Cross-section schematic of a tungsten carbide ball causing abrasion wear on an oxide surface layer

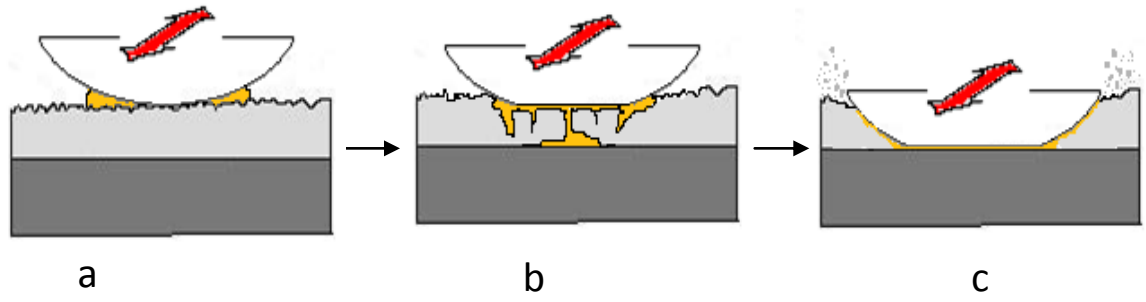

Figure 5.2-2: Cross-section schematic of a hardened steel ball causing fatigue wear under oil lubricated conditions on an oxide surface layer